

UNIVERSITÄTSKLINIKUM HAMBURG-EPPENDORF

Klinik und Poliklinik für Neurologie

Direktor: Prof. Dr. Christian Gerloff

Intra-arterial route with manipulation of the blood-brain barrier permeability for effective delivery of therapeutics to the brain

Dissertation

zur Erlangung des Grades eines Doktors der Medizin
an der Medizinischen Fakultät der Universität Hamburg.

vorgelegt von

Chengyan Chu
aus Anqing

Hamburg 2020

**Angenommen von der
Medizinischen Fakultät der Universität Hamburg am: 13. 04. 2021**

**Veröffentlicht mit Genehmigung der
Medizinischen Fakultät der Universität Hamburg.**

Prüfungsausschuss, der/die Vorsitzende: Prof. Dr. Matthias Kneussel

Prüfungsausschuss, zweite/r Gutachter/in: Prof. Dr. Tim Magnus

Table of Contents	1
1. Publications	
1.1. Real-time MRI guidance for reproducible hyperosmolar opening of the blood-brain barrier in mice	3
1.2. PET imaging of distinct brain uptake of a nanobody and similarly-sized PAMAM dendrimers after intra-arterial administration	9
1.3. Optimization of osmotic blood-brain barrier opening to enable intravital microscopy studies on drug delivery in mouse cortex.....	21
2. Introduction	
2.1. The blood-brain barrier (BBB).....	31
2.2. Hyperosmotic mannitol-induced BBB opening (BBBO)	31
2.3. Intra-arterial delivery of therapeutics to the central nervous system (CNS)	33
2.4. Intravital imaging on studying mechanisms of BBBO and drug penetration	35
2.5. Goals of the project.....	35
3. Materials and Methods	
3.1. Hyperosmotic mannitol-based BBBO	36
3.1.1. Animals and endovascular catheterization	36
3.1.2. Interventional MRI	36
3.1.3. Histological validation of BBBO	37
3.1.4. MRI and immunohistochemistry in evaluating the safety of BBBO	37
3.2. Brain uptake of nanobody and dendrimer	37
3.2.1. Gelsolin nanobody	37
3.2.2. Synthesis of NB and deferoxamine	38
3.2.3. Synthesis of Polyamidoamine (PAMAM) dendrimers and deferoxamine ...	38
3.2.4. Matrix-assisted laser desorption ionization-time-of-flight (MALDI-TOF)	38
3.2.5. Radiolabeling of NB and dendrimers	39
3.2.6. PET-CT imaging of IA and IV delivery of radiolabelled NB and dendrimer ..	39
3.2.7. Ex-vivo biodistribution of NB and dendrimer.....	40
3.3. Intravital imaging on drug delivery in mouse cortex	40
3.3.1. Cranial window implantation	40
3.3.2. Conjugation of bevacizumab and fluorescein	41
3.3.3. Intravital Epi-fluorescence and Two-photon microscopy	41
3.3.4. Histology and immunohistochemistry	42
3.4. Data processing and statistical analysis	42

4. Results

4.1. MRI guidance enabled a reproducible hyperosmolar BBBO in mice	43
4.1.1. Real-time MRI for prediction of trans-catheter perfusion territory using SPIO	43
4.1.2. Real-time MRI for precise and local BBBO using mannitol	44
4.1.3. Safety and long-term consequences of IA mannitol-induced BBBO.....	45
4.2. Intra-arterial delivery resulted in a distinct brain uptake of a nanobody and similarly-sized PAMAM dendrimers with and without BBBO	46
4.2.1. Synthesis of ⁸⁹ Zr-radiolabeled nanobody and PAMAM dendrimer	46
4.2.2. Brain uptake of ⁸⁹ Zr-radiolabeled nanobody and PAMAM dendrimer and their biodistributions.....	47
4.3. Intravital microscopy visualized the BBBO and drug targeting in mouse cortex	53
4.3.1. Hyperosmolar BBBO in cerebral cortex under MRI guidance	53
4.3.1.1. Temporary closure of contralateral CCA facilitates cortical perfusion...53	
4.3.1.2. Osmotic disruption of the BBB in cerebral cortex using real-time MRI guidance.....	54
4.3.1.3. Safety and long-term consequences of BBBO in the cortex	55
4.3.2. Vascular trans-catheter perfusion in the cortex through a cranial window...56	
4.3.3. Intravital multiphoton microscopy for visualization of cortical BBBO and drug extravasation.....	57
4.3.4. Histological confirmation of bevacizumab extravasation	58

5. Discussion

5.1. Real-time MRI enabled a safe and reproducible local BBBO	59
5.2. IA delivery resulted a distinct brain uptake regardless of BBB status for nanobodies but not for PAMAM dendrimers	59
5.3. Intravital imaging confirmed the drug penetration post BBBO	61

6. Summary

7. Reference

8. Explanation of own contribution

9. Acknowledgements

10. Curriculum vitae

11. Eidesstattliche Versicherung



Real-Time MRI Guidance for Reproducible Hyperosmolar Opening of the Blood-Brain Barrier in Mice

Chengyan Chu^{1,2,3}, Guanshu Liu^{1,4}, Miroslaw Janowski^{1,2,5,6}, Jeff W. M. Bulte^{1,2}, Shen Li^{1,2,3}, Monica Pearl⁷ and Piotr Walczak^{1,2,8*}

¹ Division of MR Research, Russell H. Morgan Department of Radiology and Radiological Science, The Johns Hopkins University School of Medicine, Baltimore, MD, United States, ² Cellular Imaging Section and Vascular Biology Program, Institute for Cell Engineering, The Johns Hopkins University School of Medicine, Baltimore, MD, United States, ³ Neurology Department, Dalian Municipal Central Hospital Affiliated with Dalian Medical University, Dalian, China, ⁴ F. M. Kirby Research Center, Kennedy Krieger Research Institute, Baltimore, MD, United States, ⁵ NeuroRepair Department, Mossakowski Medical Research Centre, Polish Academy of Sciences, Warsaw, Poland, ⁶ Department of Neurosurgery, Mossakowski Medical Research Centre, Polish Academy of Sciences, Warsaw, Poland, ⁷ Division of Interventional Neuroradiology, Russell H. Morgan Department of Radiology and Radiological Science, The Johns Hopkins University School of Medicine, Baltimore, MD, United States, ⁸ Department of Neurology and Neurosurgery, Faculty of Medical Sciences, University of Warmia and Mazury, Olsztyn, Poland

OPEN ACCESS

Edited by:

Osama O. Zaidat,
St. Vincent Mercy Medical Center,
United States

Reviewed by:

Thyagarajan Subramanian,
Independent Researcher,
Hummelstown, PA, United States
Franklin D. West,
University of Georgia, United States

*Correspondence:

Piotr Walczak
pwalczak@mr.jhu.edu

Specialty section:

This article was submitted to
Endovascular and Interventional
Neurology,
a section of the journal
Frontiers in Neurology

Received: 17 May 2018

Accepted: 10 October 2018

Published: 26 October 2018

Citation:

Chu C, Liu G, Janowski M,
Bulte JWM, Li S, Pearl M and
Walczak P (2018) Real-Time MRI
Guidance for Reproducible
Hyperosmolar Opening of the
Blood-Brain Barrier in Mice.
Front. Neurol. 9:921.
doi: 10.3389/fneur.2018.00921

The blood-brain barrier (BBB) prevents effective delivery of most therapeutic agents to the brain. Intra-arterial (IA) infusion of hyperosmotic mannitol has been widely used to open the BBB and improve parenchymal targeting, but the extent of BBB disruption has varied widely with therapeutic outcomes often being unpredictable. In this work, we show that real-time MRI can enable fine-tuning of the infusion rate to adjust and predict effective and local brain perfusion in mice, and thereby can be allowed for achieving the targeted and localized BBB opening (BBBO). Both the reproducibility and safety are validated by MRI and histology. The reliable and reproducible BBBO we developed in mice will allow cost-effective studies on the biology of the BBB and drug delivery to the brain. In addition, the IA route for BBBO also permits subsequent IA delivery of a specific drug during the same procedure and obtains high targeting efficiency of the therapeutic agent in the targeted tissue, which has great potential for future clinical translation in neuro-oncology, regenerative medicine and other neurological applications.

Keywords: blood brain barrier, intra-arterial, mannitol, MRI, mouse model

INTRODUCTION

The treatment efficacy for many central nervous system (CNS) diseases is hindered by limited access to therapeutic agents. The poor drug penetration is mainly caused by the blood-brain barrier (BBB), which sequesters the CNS from the systemic circulation. As a consequence, more than 98% of the pharmaceutical agents do not enter the brain after intravascular delivery (1–3). Thus, strategies are needed that will safely and efficiently disrupt the BBB. Intra-arterial (IA) mannitol followed by the infusion of therapeutic agents, including chemotherapeutics, gene vectors, and stem cells, has been the primary method by which therapeutics have been delivered across a disrupted BBB for several decades, both in preclinical models and in clinical studies (4–8). However, osmotic BBB opening (BBBO) proved highly variable and inconsistent (9), as it is affected by multiple factors, including the mannitol dose, injection speed, vascular anatomy, and cerebral

hemodynamics (10). This complexity and the inconsistent outcomes have resulted in highly variable published protocols (11–14).

The vast majority of previous preclinical reports on BBBO used rats or larger animals, because of the technical challenges that are encountered in mice. Our motivation to establish a reliable and safe protocol for BBBO in mice was that mice are low cost and are used for the majority of disease modeling studies. There is also an abundance of transgenic mice, indispensable for gaining insights into a variety of disorders (15, 16). Furthermore, our previous IA injection experiments in several species (10, 17–19) have shown the value and importance of monitoring local trans-catheter perfusion with MRI, allowing real-time adjustment of infusion parameters for precise and predictable BBBO and/or delivery of therapeutic agents at physiologically relevant, non-damaging infusion rates. We report here on a safe and reproducible technique to disrupt the local BBB in mice under the guidance of interventional MRI. We believe that, with our approach, the method to achieve BBBO can be reconsidered and can be re-established as a precise and effective technique that can facilitate drug delivery to the brain.

MATERIALS AND METHODS

Anesthesia and Carotid Artery Catheterization

All procedures were approved by The Johns Hopkins Animal Care and Use Committee. Male SCID mice (6–8 weeks old, 20–25 g, Jackson Laboratory) were anesthetized with 2% isoflurane. The common carotid artery (CCA) bifurcation was exposed and the occipital artery branching off from the external carotid artery (ECA) was coagulated. The ECA and the pterygopalatine artery (PPA) were temporarily ligated with 4–0 silk sutures. A temporary ligature using a 4–0 suture was placed on the carotid bifurcation and the proximal CCA was permanently ligated. A microcatheter (PE-8-100, SAI Infusion Technologies) was flushed with 2% heparin (1,000 units per ml, heparin sodium, Upjohn), inserted into the CCA via a small arteriotomy and advanced into the internal carotid artery. Before cannulation, a droplet of glue was added to the outer surface of the catheter to tightly ligate the catheter to the vessel.

Interventional MRI

The mice with a secured intra-arterial catheter were positioned in a Bruker 11.7T MRI scanner. Baseline T2 (TR/TE = 2,500/30 ms) and T1 (TR/TE 350/6.7 ms)-weighted and dynamic Gradient echo-echo planar imaging (GE-EPI, TR/TE 1250/9.7 ms, field of view (FOV) = 14, matrix = 128, acquisition time = 60 s and 24 repetitions) images of the brain were acquired. A superparamagnetic iron oxide (SPIO) nanoparticle formulation (Feridex[®], dissolved in saline at 1:30; 0.3 mg Fe/ml) was infused intra-arterially at rates between 0.05 and 0.20 ml/min under dynamic GE-EPI MRI to predict perfusion territory and optimize that territory to the desired size and location. An infusion pump (PHD 2000, Harvard Apparatus Inc.) was used to control SPIO administration. The routine was to start injections from the lowest speed, and then increase it at increments of 0.05

ml/min until an effective perfusion area was achieved. Then, 25% mannitol was delivered via an IA route over 1 min at a speed determined by previous contrast agent injection. Five minutes after mannitol injection, mice received 0.07 ml of gadolinium (Gadoteridol, 279.3 mg/mL) intraperitoneally. T1-weighted images were obtained post-gadolinium to visualize BBB integrity (20).

Histological Validation of BBBO

For histological evaluation of BBBO, 0.1 ml of IA 2% w/v Evans blue (EB) or rhodamine red (1 mmol/l) were subsequently administered intra-arterially at the same rate as mannitol. The brains were harvested right after injection and without perfusion to avoid the clearance of the both imaging agents. For EB verification, frozen coronal brain slabs (1-mm) were sliced on a cryostat. For the detection of rhodamine, the brain was cryosectioned at 30 μ m and fluorescent images of rhodamine biodistribution were acquired.

Immunohistochemistry to Evaluate the Safety of BBBO

Seven days after BBBO, animals were transcardially perfused with Five percent sucrose and then with Four percent paraformaldehyde. The brains were cryopreserved in 30% sucrose and cryosectioned at 30- μ m. Primary antibodies and dilutions were used as follows: anti-GFAP (1:250, Dako); anti-Iba1 (1:250, Wako); and anti-NeuN (1:100, Cell Signaling Technology). The secondary antibody was goat anti-rabbit (Alexa Fluor-488, 1:200, Molecular Probes).

Image Processing and Statistical Analysis

Quantitation of immunohistochemistry results was based on relative fluorescence using Image J and analyzed with Mann-Whitney *U*-test. While stereology is more accurate and appropriate when absolute cell numbers are essential, in case of microglial or astrocytic activation both cell number and signal intensity are relevant, thus we measured relative fluorescence. The MRI analysis of the change in area of the SPIO perfusion territory and Gd-enhancement for each mouse was calculated by a custom-written script in MATLAB and also analyzed with Mann-Whitney *U*-test. A Pearson correlation coefficient comparing the above-mentioned areas was calculated using GraphPad software.

RESULTS

Real-Time MRI for Prediction of Trans-catheter Perfusion Territory Using SPIO

The infusion of SPIO results in a drop of T2* hypointensity on MRI, which immediately clears once the infusion is stopped. This T2* hypointensity in the brain can be sampled by GE-EPI at a temporal resolution of 2 images each second, which allows precise temporo-spatial visualization of the parenchymal perfusion territory. Initially, our transcatheter SPIO contrast delivery was set at 0.05 ml/min, and in those animals in which no drop of T2* intensity was observed, we increased

the speed at increments 0.05 ml/min, until the contrast agent appeared on real-time MRI. There was no need to increase the speed over 0.15 ml/min, which resulted in satisfactory and reproducible brain perfusion, as visualized by a characteristic reduction in signal intensity for the duration of the injection bolus (Figures 1a,b). Notably, increasing the infusion speed to 0.2 ml/min resulted in delayed brain injury, as shown by an abnormal signal on T2-weighted images and pathological changes on histology (Supplemental Figure 1). In addition, the injection rate for a satisfactory perfusion territory varied among

mice, necessitating the titration of the injection speed for each animal.

Real-Time MRI for Precise and Local BBBO Using Mannitol

Immediately after the optimal infusion rate was determined for a particular mouse using SPIO, IA mannitol was infused at that rate for 1 min. To clearly present the MRI images, the signal change maps of SPIO-perfusion and Gd-contrast enhancement

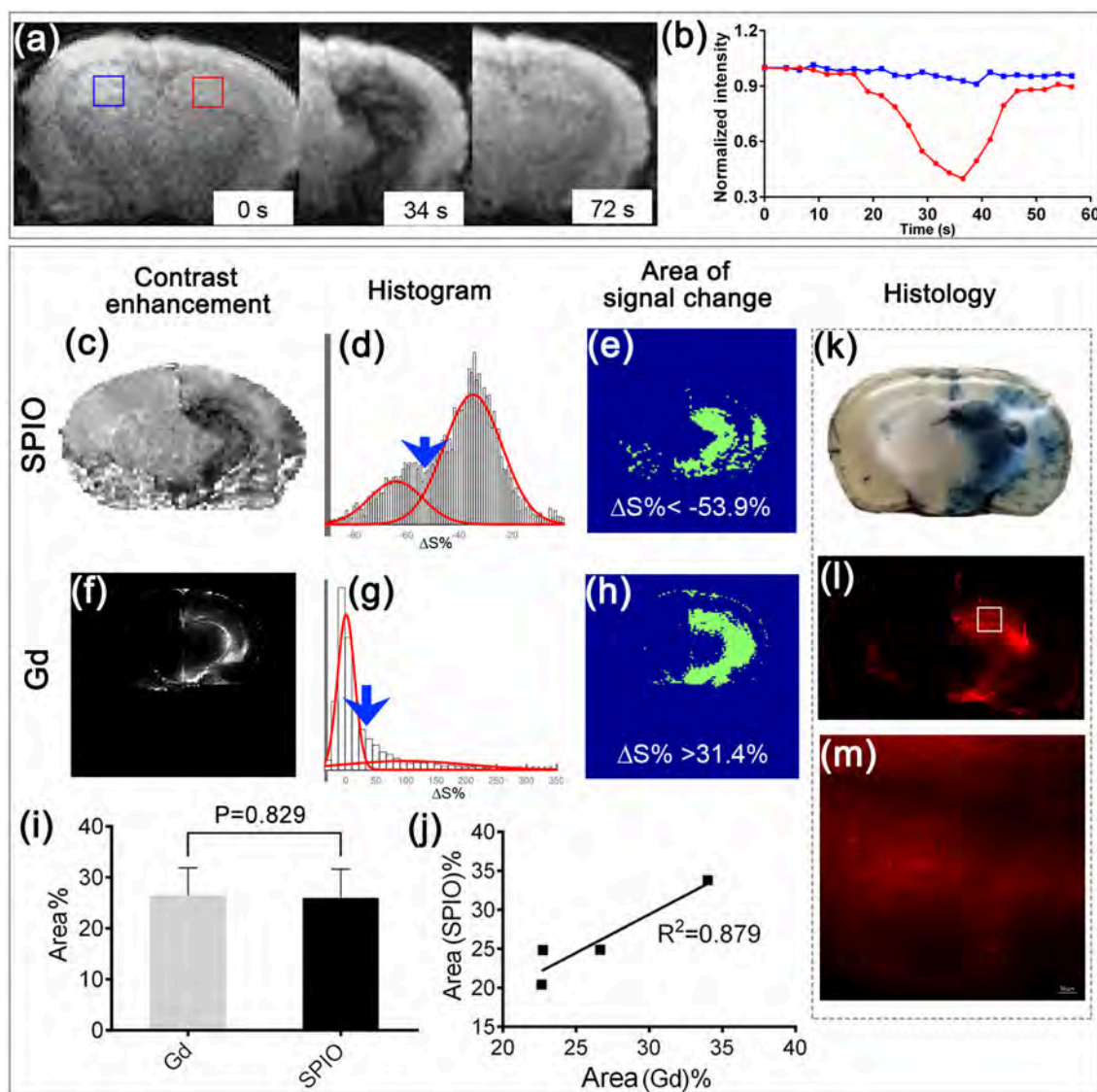


FIGURE 1 | Real-time MRI to predict BBBO territory and histological validation. **(a)** Representative T2* images before, 34, and 72 s after infusion of SPIO at a rate of 0.15 ml/min. **(b)** Dynamic signal changes of the two ROIs marked in **(a)**. **(c)** Contrast enhancement map at 34 s after SPIO infusion. **(d)** Histogram analysis of pixel intensities in **(c)**, showing two Gaussian distributions (red lines). Blue arrow points to where a cut-off of -53.9% was applied to separate the two distributions. **(e)** Segmented map shows the area where the relative signal change was smaller than -53.9%. **(f)** Contrast enhancement map, **(g)** histogram analysis, and **(h)** segmented map ($\Delta S\% > 31.4\%$) at 5 min after i.p. injection of Gd. **(i)** Bar graph and **(j)** correlation analysis of the BBBO territory predicted by SPIO and that assessed using Gd ($n = 4$, mean \pm SD). The histological analyses show the region with extravasation of Evans blue **(k)** and rhodamine **(l, m)**; **(m)** shows the zoomed-in area indicated by the white square in **(l)** following mannitol injection.

(Gd-CE) were calculated first (**Figures 1c,f**). As a consequence, such an approach resulted in an effective BBBO as reflected by gadolinium enhancement on the T1-weighted scan, which showed hyperintensity in the region previously highlighted by the contrast infusion (**Figures 1c,f**). The correlation between the SPIO-perfusion (**Figure 1c**) and Gd-CE (**Figure 1f**) MRI was determined. The histograms were drawn and fitted into two Gaussian distributions (**Figures 1d,g**). The values that corresponded to the minimal overlap between the two Gaussian functions were chosen to be the threshold that separated the pixels with a significant signal change. Using these determined thresholds, the areas with a significant signal change were determined (**Figures 1e,h**). For the four mice studied, the SPIO perfusion MRI showed an average signal change area of $26.00 \pm 5.60\%$, while Gd-CE showed an average signal change area of $26.52 \pm 5.33\%$, which was not significantly different ($P = 0.829$, **Figure 1i**). A good correlation was shown between these two methods ($r = 0.937$, $R^2 = 0.879$, **Figure 1j**). This indicated a successful BBBO by IA mannitol, as predicted by the perfusion pre-scan. Furthermore, the histopathological validation using Evans Blue, which is a gold standard for BBB assessment and rhodamine, which was used as a surrogate marker of therapeutic agents, demonstrated a pattern of extravasation that was consistent with MRI (**Figures 1k-m**).

Safety and Long-Term Consequences of IA Mannitol-Induced BBBO

To assess the safety of our BBBO protocol, mice were assessed for neurological and MRI sequelae. Three days after BBBO,

MRI showed neither T2 abnormalities nor T1 Gd-enhancement (**Figure 2a**), indicating that the procedure was safe and that the BBB breach was transient, and did not cause permanent brain damage. Histology confirmed these observations with GFAP and IBA-1 staining 7 days post BBBO, in which there was no elevated astrocytic or microglia activation in the BBBO region, as measured by fluorescence intensity. There was no statistically significant difference in fluorescence intensity between the targeted region and the contralateral hemisphere ($P = 0.571$, $P = 0.093$; **Figures 2b,c**). Similarly, there was no evidence of neuronal damage based on NeuN staining ($P = 0.331$, **Figure 2d**).

DISCUSSION

The overall goal of BBBO is to maximize CNS targeting of the therapeutic agent while minimizing systemic toxicity. Various methods and drugs have been developed to induce transient permeabilization of the BBB, with IA mannitol-mediated osmotic disruption being the most frequently used procedure in both preclinical and clinical studies (7, 8, 21). Although osmotic BBBO has been an established method for decades, the parameters for inducing BBBO are highly variable and inconsistent. The infusion speed, in particular, is one of the most critical parameters in small animals and many published reports recommend an infusion that highly exceeds the physiological perfusion rate in the carotid artery, leading to brain damage (17, 22, 23). For example, in different preclinical studies, the infusion velocity of mannitol into the carotid artery for some rat studies was as low as 3.0 ml/min (14) or as high as 7.2 ml/min (13).

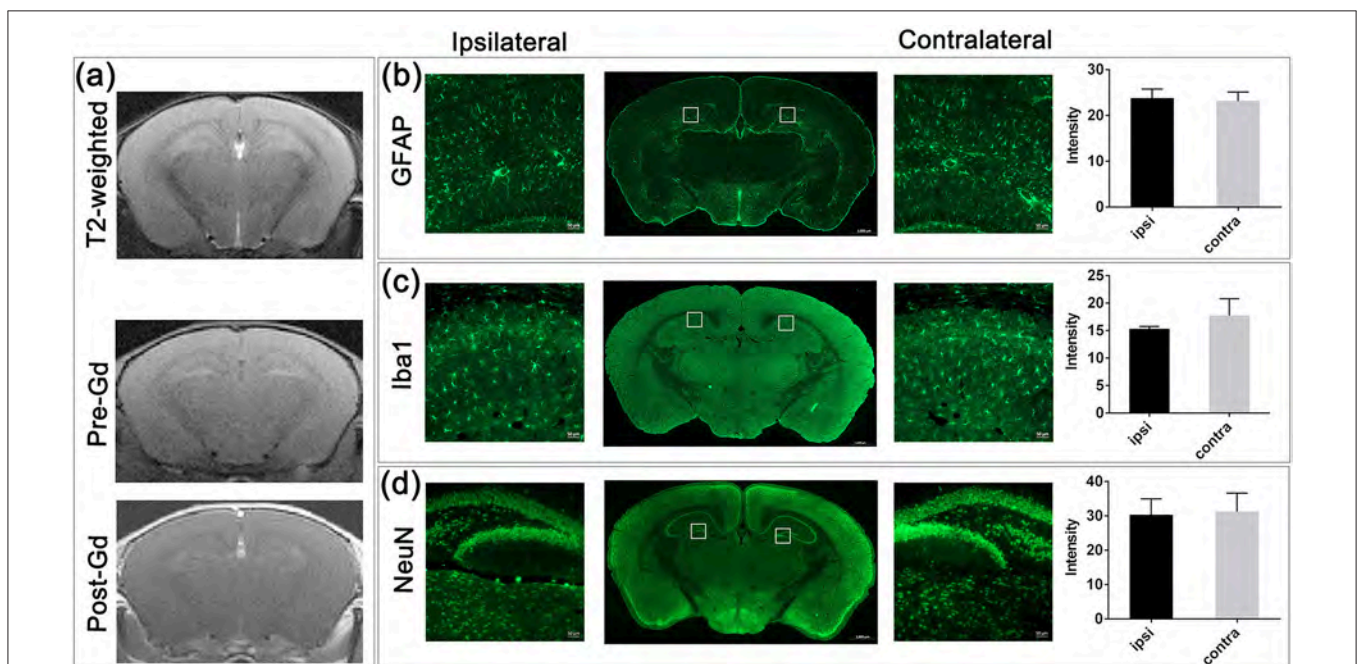


FIGURE 2 | MRI and histological assessment post-BBBO. **(a)** T2-weighted, pre-Gd, and post-Gd images 3 days after BBBO showed no sign of brain damage. No Gd-CE could be observed in the brain, suggesting that the BBB was resealed. Fluorescent staining of the BBBO region with GFAP **(b)**, Iba1 **(c)**, and NeuN **(d)** revealed comparable intensity between the ipsilateral and the contralateral hemisphere (2 ROIs/hemisphere as represented in lower magnification, $n = 4$, mean \pm SD) indicating no inflammation and no neuronal loss after BBBO.

Similarly, one mouse BBBO study reported that the procedure was performed with an IA infusion at a very high rate of 1.0 ml/min (6), which, in addition to the effect of mannitol, would likely have a direct damaging effect on the BBB. In that study, the PPA was not ligated, which might have added variability to the procedure, as the majority of the flow might be through the PPA and not the ICA (24). Indeed, we have shown that IA infusion into the rat internal carotid artery at rates exceeding 0.9 ml/min is damaging and results in scattered white matter hyperintensities (17). Here, we also found severe damage when the speed reached 0.2 ml/min indicating fine balance effective BBBO and damage. We also believe that PPA obstruction is necessary to route the entire contrast agent and mannitol volume to the cerebral arteries. Thus, we exploited dynamic susceptibility contrast MRI for perfusion prediction prior to BBBO. We escalated the rate from a low speed, increasing in 0.05 ml/min increments until the desired perfusion territory was reached. The extravasation of rhodamine and Evans blue corroborated the efficacy of BBBO, therefore suggesting that IA mannitol-mediated local BBBO is predictable and can be targeted to a specific region. The IA route for BBBO also allows immediate IA delivery of a specific drug during the same procedure, thus providing a “one-stop-shop” and improving the probability to achieve an adequate therapeutic concentration. Finally, SPIO in our study has been used at about 0.6 mg/kg which is similar to the dose previously used in patients (25).

Hence, our procedure may have potential for future clinical translation.

AUTHOR CONTRIBUTIONS

CC, GL, MJ, JB, SL, MP and PW conception and design. CC, GL and PW acquisition of data. CC, GL, MJ, JB, SL, MP and PW analysis and interpretation of data. CC draft of the manuscript. CC, GL, MJ, JB, SL, MP and PW revision, and final approval.

FUNDING

This study was supported by Maryland Stem Cell Research Foundation grant 2017-MSCRFD-3942, NIH R01 NS091110, NIH R21NS091599, and Strategmed 1/233209/12/NCBIR/2015.

ACKNOWLEDGMENTS

We thank Mary McAllister for editorial assistance.

SUPPLEMENTARY MATERIAL

The Supplementary Material for this article can be found online at: <https://www.frontiersin.org/articles/10.3389/fneur.2018.00921/full#supplementary-material>

REFERENCES

- Goldstein GW, Betz AL. The blood-brain-barrier. *Sci Am.* (1986) 255:74–83. doi: 10.1038/scientificamerican0986-74
- Pardridge WM. The blood-brain barrier: bottleneck in brain drug development. *NeuroRx* (2005) 2:3–14. doi: 10.1602/neurorx.2.1.3
- Budde MD, Janes L, Gold E, Turtzo LC, Frank JA. The contribution of gliosis to diffusion tensor anisotropy and tractography following traumatic brain injury: validation in the rat using Fourier analysis of stained tissue sections. *Brain* (2011) 134(Pt 8):2248–60. doi: 10.1093/brain/awr161
- Rapoport SI. Osmotic opening of the blood-brain barrier: principles, mechanism, and therapeutic applications. *Cell Mol Neurobiol.* (2000) 20:217–30. doi: 10.1023/A:1007049806660
- Burkhardt JK, Riina H, Shin BJ, Christos P, Kesavabhotla K, Hofstetter CP, et al. Intra-arterial delivery of bevacizumab after blood-brain barrier disruption for the treatment of recurrent glioblastoma: progression-free survival and overall survival. *World Neurosurg.* (2012) 77:130–4. doi: 10.1016/j.wneu.2011.05.056
- Foley CP, Rubin DG, Santillan A, Sondhi D, Dyke JP, Crystal RG, et al. Intra-arterial delivery of AAV vectors to the mouse brain after mannitol mediated blood brain barrier disruption. *J Control Release* (2014) 196:71–8. doi: 10.1016/j.jconrel.2014.09.018
- Gonzales-Portillo GS, Sanberg PR, Franzblau M, Gonzales-Portillo C, Diamandis T, Staples M, et al. Mannitol-enhanced delivery of stem cells and their growth factors across the blood-brain barrier. *Cell Transplant.* (2014) 23:531–9. doi: 10.3727/096368914X678337
- Chakraborty S, Filippi CG, Wong T, Ray A, Fralin S, Tsiouris AJ, et al. Superselective intraarterial cerebral infusion of cetuximab after osmotic blood/brain barrier disruption for recurrent malignant glioma: phase I study. *J Neurooncol.* (2016) 128:405–15. doi: 10.1007/s11060-016-2099-8
- Joshi S, Ergin A, Wang M, Reif R, Zhang J, Bruce JN, et al. Inconsistent blood brain barrier disruption by intraarterial mannitol in rabbits: implications for chemotherapy. *J Neurooncol.* (2011) 104:11–9. doi: 10.1007/s11060-010-0466-4
- Janowski M, Walczak P, Pearl MS. Predicting and optimizing the territory of blood-brain barrier opening by superselective intra-arterial cerebral infusion under dynamic susceptibility contrast MRI guidance. *J Cereb Blood Flow Metab.* (2016) 36:569–75. doi: 10.1177/0271678X15615875
- Bhattacharjee AK, Nagashima T, Kondoh T, Tamaki N. Quantification of early blood-brain barrier disruption by *in situ* brain perfusion technique. *Brain Res Brain Res Protoc.* (2001) 8:126–31. doi: 10.1016/S1385-299X(01)00094-0
- Chi OZ, Liu X, Weiss HR. Effects of mild hypothermia on blood-brain barrier disruption during isoflurane or pentobarbital anesthesia. *Anesthesiology* (2001) 95:933–8. doi: 10.1097/0000542-200110000-00023
- Yang WL, Barth RF, Leveille R, Adams DM, Ciesielski M, Fenstermaker RA, et al. Evaluation of systemically administered radiolabeled epidermal growth factor as a brain tumor targeting agent. *J Neuro Oncol.* (2001) 55:19–28. doi: 10.1023/A:1013017821166
- Kaya M, Gulturk S, Elmas I, Kalayci R, Arican N, Kocyildiz ZC, et al. The effects of magnesium sulfate on blood-brain barrier disruption caused by intracarotid injection of hyperosmolar mannitol in rats. *Life Sci.* (2004) 76:201–12. doi: 10.1016/j.lfs.2004.07.012
- Rivera J, Sobey CG, Walduck AK, Drummond GR. Nox isoforms in vascular pathophysiology: insights from transgenic and knockout mouse models. *Redox Rep.* (2010) 15:50–63. doi: 10.1179/174329210X12650506623401
- Doyle A, McGarry MP, Lee NA, Lee JJ. The construction of transgenic and gene knockout/knockin mouse models of human disease. *Transgenic Res.* (2012) 21:327–49. doi: 10.1007/s11248-011-9537-3
- Janowski M, Lyczek A, Engels C, Xu J, Lukomska B, Bulte JW, et al. Cell size and velocity of injection are major determinants of the safety of intracarotid stem cell transplantation. *J Cereb Blood Flow Metab.* (2013) 33:921–7. doi: 10.1038/jcbfm.2013.32
- Song X, Walczak P, He X, Yang X, Pearl M, Bulte JW, et al. Salicylic acid analogues as chemical exchange saturation transfer MRI contrast agents for the assessment of brain perfusion territory and blood-brain barrier opening

- after intra-arterial infusion. *J Cereb Blood Flow Metab.* (2016) 36:1186–94. doi: 10.1177/0271678X16637882
19. Walczak P, Wojtkiewicz J, Nowakowski A, Habich A, Holak P, Xu J, et al. Real-time MRI for precise and predictable intra-arterial stem cell delivery to the central nervous system. *J Cereb Blood Flow Metab.* (2017) 37:2346–58. doi: 10.1177/0271678X16665853
 20. Qin H, Janowski M, Pearl MS, Malysz-Cymborska I, Li S, Eberhart CG, et al. Rabbit model of human gliomas: implications for intra-arterial drug delivery. *PLoS ONE* (2017) 12:e0169656. doi: 10.1371/journal.pone.0169656
 21. Cloughesy TF, Gobin YP, Black KL, Vinuela F, Taft F, Kadkhoda B, et al. Intra-arterial carboplatin chemotherapy for brain tumors: a dose escalation study based on cerebral blood flow. *J Neurooncol.* (1997) 35:121–31. doi: 10.1023/A:1005856002264
 22. Cui LL, Kerkela E, Bakreen A, Nitzsche F, Andrzejewska A, Nowakowski A, et al. The cerebral embolism evoked by intra-arterial delivery of allogeneic bone marrow mesenchymal stem cells in rats is related to cell dose and infusion velocity. *Stem Cell Res Ther.* (2015) 6:11. doi: 10.1186/scrt544
 23. Guzman R, Janowski M, Walczak P. Intra-arterial delivery of cell therapies for stroke. *Stroke* (2018) 49:1075–82. doi: 10.1161/STROKEAHA.117.018288
 24. Gorelik M, Orukari I, Wang J, Galpoththawela S, Kim H, Levy M, et al. Use of MR cell tracking to evaluate targeting of glial precursor cells to inflammatory tissue by exploiting the very late antigen-4 docking receptor. *Radiology* (2012) 265:175–85. doi: 10.1148/radiol.12112212
 25. Zheng WW, Zhou KR, Chen ZW, Shen JZ, Chen CZ, Zhang SJ. Characterization of focal hepatic lesions with SPIO-enhanced MRI. *World J Gastroenterol.* (2002) 8:82–6. doi: 10.3748/wjg.v8.i1.82

Conflict of Interest Statement: The authors declare that the research was conducted in the absence of any commercial or financial relationships that could be construed as a potential conflict of interest.

Copyright © 2018 Chu, Liu, Janowski, Bulte, Li, Pearl and Walczak. This is an open-access article distributed under the terms of the Creative Commons Attribution License (CC BY). The use, distribution or reproduction in other forums is permitted, provided the original author(s) and the copyright owner(s) are credited and that the original publication in this journal is cited, in accordance with accepted academic practice. No use, distribution or reproduction is permitted which does not comply with these terms.



PET imaging of distinct brain uptake of a nanobody and similarly-sized PAMAM dendrimers after intra-arterial administration

Wojciech G. Lesniak¹ · Chengyan Chu^{1,2} · Anna Jablonska^{1,2} · Babak Behnam Azad¹ · Olivier Zwaenepoel³ · Michal Zawadzki⁴ · Ala Lisok¹ · Martin G. Pomper¹ · Piotr Walczak^{1,2} · Jan Gettemans³ · Miroslaw Janowski^{1,2}

Received: 2 December 2018 / Accepted: 29 April 2019 / Published online: 3 June 2019
© Springer-Verlag GmbH Germany, part of Springer Nature 2019

Abstract

Introduction We have recently shown that intracerebral delivery of an anti-VEGF monoclonal antibody bevacizumab using an intra-arterial (IA) infusion is more effective than intravenous administration. While antibodies are quickly emerging as therapeutics, their disadvantages such as large size, production logistics and immunogenicity motivate search for alternatives. Thus we have studied brain uptake of nanobodies and polyamidoamine (PAMAM) dendrimers.

Methods Nanobodies were conjugated with deferoxamine (DFO) to generate NB(DFO)₂. Generation-4 PAMAM dendrimers were conjugated with DFO, and subsequently primary amines were capped with butane-1,2-diol functionalities to generate G4(DFO)₃(Bdiol)₁₁₀. Resulting conjugates were radiolabeled with zirconium-89. Brain uptake of ⁸⁹ZrNB(DFO)₂ and ⁸⁹ZrG4(DFO)₃(Bdiol)₁₁₀ upon carotid artery vs tail vein infusions with intact BBB or osmotic blood–brain barrier opening (OBBBO) with mannitol in mice was monitored by dynamic positron emission tomography (PET) over 30 min to assess brain uptake and clearance, followed by whole-body PET-CT (computed tomography) imaging at 1 h and 24 h post-infusion (pi). Imaging results were subsequently validated by ex-vivo biodistribution.

Results Intravenous administration of ⁸⁹ZrNB(DFO)₂ and ⁸⁹ZrG4(DFO)₃(Bdiol)₁₁₀ resulted in their negligible brain accumulation regardless of BBB status and timing of OBBBO. Intra-arterial (IA) administration of ⁸⁹ZrNB(DFO)₂ dramatically increased its brain uptake, which was further potentiated with prior OBBBO. Half of the initial brain uptake was retained after 24 h. In contrast, IA infusion of ⁸⁹ZrG4(DFO)₃(Bdiol)₁₁₀ resulted in poor initial accumulation in the brain, with complete clearance within 1 h of administration. Ex-vivo biodistribution results reflected those on PET-CT.

Conclusions IA delivery of nanobodies might be an attractive therapeutic platform for CNS disorders where prolonged intracranial retention is necessary.

Keywords PET · Nanobody · Dendrimer · Intra-arterial · Zirconium · Brain

This article is part of the Topical Collection on Neurology

Wojciech G. Lesniak and Chengyan Chu contributed equally to this work.

Electronic supplementary material The online version of this article (<https://doi.org/10.1007/s00259-019-04347-y>) contains supplementary material, which is available to authorized users.

✉ Wojciech G. Lesniak
wlesniak1@jhmi.edu

✉ Miroslaw Janowski
mjanows1@jhmi.edu

¹ The Russell H. Morgan Department of Radiology and Radiological Science, Johns Hopkins University School of Medicine, Baltimore, MD, USA

² Institute for Cell Engineering, Johns Hopkins University School of Medicine, Baltimore, MD, USA

³ Department of Biomolecular Medicine, Faculty of Medicine and Health Sciences, Ghent University, Ghent, Belgium

⁴ Department of Radiology, Centre of Postgraduate Medical Education, Warsaw, Poland

Introduction

Neurological disorders and cerebral malignancies continue to be a significant burden to the society, in part due to the blood–brain barrier (BBB), which limits access for most drugs circulating in the blood, precluding them from reaching therapeutic concentrations in the central nervous system (CNS) [1]. Importantly, another relevant function of BBB is active efflux of molecules from the CNS [2]. Therefore, parenchymal accumulation of neurotherapeutic agents is contingent upon both penetration to the CNS and circumvention of clearance by the BBB. There are several methods to increase permeability and drug transport across the BBB; however, strategies to overcome drug clearance by BBB are less explored [3]. Low molecular weight and lipophilic molecules have been considered as most suitable for therapy of CNS disorders [4]; however, they have fallen short, necessitating alternative approaches.

Advances in biotechnology enable efficient and cost-effective design of macromolecules including antibodies, nanobodies, fusion proteins, and synthetic nanoparticles. Such scaffolds can be designed with high affinity and specificity for safe engagement of certain molecular targets [5]. These advances can also be applied to CNS therapeutics. We have recently shown that systemically infused anti-VEGF monoclonal antibody (bevacizumab) failed to accumulate in the brain, even upon osmotic blood–brain barrier opening (OBBBO) [6]. Transporter-based delivery of intravenously (IV)-administered antibodies to the brain increased their uptake by an order of magnitude [7]. Intra-arterial (IA) delivery of bevacizumab, however, resulted in significant accumulation in the brain as measured by positron emission tomography (PET) (~10% of injected dose per cubic centimeter of tissue, %ID/cc), which was further increased by OBBBO to ~25 %ID/cc, several orders of magnitude higher than for systemic (IV) delivery [6]. Importantly, retention of bevacizumab in the brain after 24 h was high, which makes IA delivery of antibodies an attractive strategy, especially as the precision of endovascular infusions has been significantly improved by real-time guidance through magnetic resonance imaging (MRI) [8, 9]. We have recently applied this approach clinically in a patient with aggressive recurrent glioblastoma multiforme, and IA injection of bevacizumab, which resulted in a rapid therapeutic response [10].

While antibodies are quickly emerging as therapeutic agents, and demonstrated efficacy of their IA delivery to the CNS is an important step towards treatment of neurological disorders and CNS malignancies, they are plagued with several disadvantages including relatively complex production, high cost, and immunogenicity. Accordingly,

there is growing interest in nanobodies as therapeutic agents and dendrimers as drug nanocarriers. Nanobodies are derived from naturally occurring heavy chain antibodies in camelids. They are one-tenth (~15 kDa) of the size of monoclonal antibodies. The small size of nanobodies has several advantages such as easy in-vitro production, lack of immune recognition, high affinity to molecular targets, and improved permeability across biological barriers [11, 12]. Furthermore, nanobody cDNAs are routinely produced, which opens opportunities for derivatization with fluorophores or anti-cancer therapeutics. Polyamidoamine (PAMAM) dendrimers are quickly emerging as a versatile nanopatform for selective drug delivery due to their unique physicochemical properties, including small size, large number of reactive terminal groups that can be readily modified with different functionalities, bulky interior void volume, and biocompatibility [13, 14]. There have been reports of PAMAM dendrimers that cross the BBB upon IV administration, and their selective uptake by activated microglia in an experimental model of cerebral palsy [15, 16]. Another report involves accumulation of dendrimers within intracranial tumor-associated macrophages in a rodent model of gliosarcoma [17]. A generation-4 PAMAM dendrimer has a similar size to a nanobody and has the further advantage of capacity for conjugation with various functionalities, including ligands for molecular targets, imaging-radio-, chemo-, and immunotherapeutic agents [18]. Potential benefits of IA delivery of nanobodies and dendrimers over IV administration have not been assessed until now. Here, we measure the ability for nanobodies and generation-4 PAMAM hydroxy terminated dendrimers to penetrate and clear from the CNS using PET. In our study, neither nanobody nor dendrimer have specific targets in the brain, to provide basal kinetics for future studies with brain-targeted molecules and molecular targets in specific neurological diseases.

Materials

All chemicals were purchased from Sigma–Aldrich (Milwaukee, WI, USA) or Fisher Scientific (Tewksbury, MA, USA) unless otherwise specified. Ethylenediamine core amine-terminated generation-4 poly(amidoamine dendrimer) [G4(NH₂)₆₄] was acquired from Dendritech (Midland, MI, USA). ⁸⁹Zr(C₂O₄)₂ (t_{1/2} = 78.4 h) and 1-(4-isothiocyanatophenyl)-3-[6,17-dihydroxy-7,10,18,21-tetraoxo-27-(N-acetylhydroxylamino)-6,11,17,22-tetraazaheptaicosine] thiourea (p-SCN-Bn-DFO, Cat. # B-705) were obtained from Washington University (St. Louis, MO, USA) and Macrocyclics (Plano, TX, USA),

respectively. All reagents and solvents were used as received without further purification.

Nanobody

Gelsolin nanobody 11 (NB11), cloned in the pHEN6c vector, was purified from WK6 cells as described previously [19]. Briefly, competent WK6 cells were transformed with the plasmid and grown at 37 °C in TB medium with 100 µg/ml ampicillin until the OD₆₀₀ reached 0.60–0.80. Then temperature was set to 20 °C and nanobody expression was induced by the addition of 0.5 mM IPTG. After overnight induction, bacterial cultures were pelleted by centrifugation at 11,000×g for 20 min at 4 °C. Cells were resuspended in a small volume of phosphate-buffered saline (PBS), and 0.2 mg/ml lysozyme was added. Lysis proceeded during 30 min rotation at room temperature. This suspension was then sonicated (Vibracell, Sonics and Materials, Newtown, CT, USA) and centrifuged again (~29,000×g) for 30 min at 4 °C to obtain the bacterial protein lysate. The His₆-tagged nanobody was purified by Immobilized metal ion affinity chromatography (IMAC) on a Ni²⁺ column and eluted with 500 mM imidazole. Finally, nanobody 11 was purified to homogeneity by gel filtration chromatography on a Superdex 200 HR 10/30 column (GE Healthcare, Diegem, Belgium), equilibrated in 20 mM Tris.HCl pH 7.5, 150 mM NaCl, 1 mM DTT. *Composition of NB11*: Ala (11, 8.6%), Arg (9, 7.0%), Asn (4, 3.1%), Asp (9, 7.0%), Cys (2, 1.6%), Gln (9, 7.0%), Glu (3, 2.3%), Gly (14, 10.9%), His (1, 0.8%), Ile (2, 1.6%), Leu (7, 5.5%), Lys (4, 3.1%), Met (3, 2.3%), Phe (5, 3.9%), Pro (4, 3.1%), Ser (16, 12.5%), Thr (9, 7.0%), Trp (2, 1.6%), Tyr (5, 3.9%), Val (9, 7.0%). *Physicochemical properties*: total number of negatively charged residues (Asp + Glu) 12, total number of positively charged residues (Arg + Lys) 13, grand average of hydropathicity (GRAVY) 0.534, aliphatic index 56.41. *Biological properties*: the estimated half-life 30 h (mammalian reticulocytes, in vitro), > 20 h (yeast, in vivo), > 10 h (*Escherichia coli*, in vivo).

Synthesis of NB(DFO)₂

For conjugation of DFO with nanobody, storage buffer was replaced with saline using ultrafiltration with Millipore Amicon Ultra Centrifugal Filters 3000 Da molecular weight cut-off (MWCO, Millipore Sigma, cat #: UFC80030) and pH was adjusted to 9 with a small amount of 2 M Na₂CO₃ solution. Then five-fold molar equivalent of SCN-Bn-DFO dissolved in DMSO was added and conjugation was carried out for 30 min at 37 °C in a thermomixer at 550 r.p.m. Resulting NB-DFO conjugate was purified as described above, reconstituted in saline at 10 mg/ml and 0.1 ml aliquots were kept at −20 °C until further use.

Synthesis of G4(DFO)₃(Bdiol)₁₁₀ dendrimer

Preparation of G4(DFO)₃(Bdiol)₁₁₀ involved a one-pot, two-step synthesis as presented in Fig. 4. G4(NH₂)₆₄ dendrimer (0.030 g, 2.11 × 10^{−6} mol) was dissolved in 3 ml deionized water resulting in pH = 9.2 and 5 mol equivalent of SCN-Bn-DFO (0.008 g, 1.05 × 10^{−5} mol) reconstituted in 0.2 ml of DMSO was added. The reaction proceeded for 30 min at 37 °C in a thermomixer at 550 r.p.m., and a small amount of reaction mixture was subjected to MALDI-TOF mass spectrometry to confirm conjugation of DFO with dendrimer. Next, 0.2 ml (2.99 × 10^{−3} mol) of glycidol was added and reaction was carried for additional overnight to cap remaining primary amines with butane-1,2-diol (Bdiol). Resulting G4(DFO)₃(Bdiol)₁₁₀ dendrimer was purified using deionized water and ultrafiltration with Millipore Amicon Ultra Centrifugal Filters 10,000 Da MWCO, lyophilized, yielding 0.035 g of the conjugate, which was stored at −20 °C until further use.

Matrix-assisted laser desorption ionization-time-of-flight (MALDI-TOF)

To determine average number of DFO molecules conjugated with nanobody and dendrimer and assess its capping efficiency with butane-1,2-diol, MALDI-TOF spectra were recorded on a Voyager DE-STR spectrophotometer, using 2,5-dihydroxybenzoic acid (DHB) as a matrix, which was dissolved in 50% MeOH and 0.1% TFA aqueous solution at concentration of 20 mg/ml. NB and NB(DFO)₂ samples were desalted using Zeba™ spin columns 7 K MWCO (cat. # 89882, Thermo Fisher Scientific). Samples of G4(NH₂)₆₄, G4(NH₂)₆₁,(DFO)₃, and G4(DFO)₃(Bdiol)₁₁₀ dendrimers were prepared in deionized water. 10 µl of samples were mixed with 10 µl of matrix, and 1 µl of resulting mixture was placed on the target plate (in triplicate) and evaporated. Number of shots and laser power was adjusted according to spectrum quality.

Dynamic light scattering and zeta potential analysis

Dynamic light scattering and zeta potential analyses were performed using a Malvern Zetasizer Nano ZEN3600. G4(DFO)₃(Bdiol)₁₁₀ dendrimer was prepared at a concentration of 4 mg/ml in PBS (c = 0.1 M, pH 7.4). DLS measurements were performed at a 90° scattering angle at 25 °C. Zeta potential analysis was carried out using the same solution.

Radiolabeling of NB(DFO)₂ and G4(DFO)₃(Bdiol)₁₁₀

Radiolabeling of NB(DFO)₂ and G4(DFO)₃(Bdiol)₁₁₀ with ⁸⁹Zr was performed using reported procedure [20]. ⁸⁹ZrNB(DFO)₂ was fabricated with ~99% radiochemical

purity and 129.5 ± 10 MBq/mg specific activity. $^{89}\text{ZrG4(DFO)}_3(\text{Bdiol})_{110}$ was prepared with $\sim 99\%$ radiochemical purity and 120 ± 8 MBq/mg specific activity. For further studies, $^{89}\text{ZrNB(DFO)}_2$ and $^{89}\text{ZrG4(DFO)}_3(\text{Bdiol})_{110}$ were diluted with sterile saline.

Partition coefficient of $^{89}\text{ZrNB(DFO)}_2$ and $^{89}\text{ZrG4(DFO)}_3(\text{Bdiol})_{110}$

To vials containing 0.5 ml PBS (pH 7.4), 0.5 ml of octanol, 0.74 MBq of $^{89}\text{ZrNB(DFO)}_2$ or $^{89}\text{ZrG4(DFO)}_3(\text{Bdiol})_{110}$ was added ($n = 3$). Resulting solutions were vortexed vigorously for 3 min. Then to achieve efficient phase separation, vials were centrifuged for 5 min at $4000\times g$. Aliquots (100 μl) of the aqueous and the octanol phase were collected and the radioactivity in the respective samples were measured using a PerkinElmer - 2480 Automatic Gamma Counter (Waltham, MA). The LogP values were calculated from the means of $n = 3$ separate measurements.

PET-CT imaging of IA and IV delivery of $^{89}\text{ZrNB(DFO)}_2$ and $^{89}\text{ZrG4(DFO)}_3(\text{Bdiol})_{110}$ with or without OBBBO

PET-CT studies were performed as we have recently described [6] using 6–8-week-old male C3HeB/FeJ mice (stock number 000658; Jackson, $n = 4$ per group, total $n = 28$). Under general anesthesia, a catheter was placed in the internal carotid artery (ICA), as we have reported previously [21] and mice were transferred to the PET-CT scanner. BBB opening was performed with 25% mannitol infused for 1 min at a speed of 0.15 ml/min. Speed of mannitol infusion to achieve reproducible BBB opening in mice was optimized in our previous study [21]; ~ 8.5 MBq (~ 230 μCi) of $^{89}\text{ZrNB(DFO)}_2$ or $^{89}\text{ZrG4(DFO)}_3(\text{Bdiol})_{110}$ reconstituted in 1 ml of saline was infused IA or IV over 5 min at 0.15 ml/min flow rate. There were four experimental groups: 1) IA infusion with BBB intact (IA/BBBI), 2) OBBBO followed by IA infusion (OBBBO/IA), 3) OBBBO followed by intravenous infusion (OBBBO/IV) and 4) intravenous infusion followed by OBBBO (IV/OBBBO) for $^{89}\text{ZrNB(DFO)}_2$. Three groups — 1) IA infusion with BBB intact (IA/BBBI), 2) OBBBO followed by IA infusion (OBBBO/IA), and 3) intravenous infusion followed by OBBBO (IV/OBBBO) — were evaluated for $^{89}\text{ZrG4(DFO)}_3(\text{Bdiol})_{110}$. Accumulation of $^{89}\text{ZrNB(DFO)}_2$ or $^{89}\text{ZrG4(DFO)}_3(\text{Bdiol})_{110}$ in the brain was initially evaluated with dynamic 30-min-long PET scans divided into 30 s frames, followed by whole body PET/CT imaging acquired around 1 h and 24 h post-infusion (pi), in two bed positions and 7 min per bed on an ARGUS small-animal PET/CT scanner (Sedecal, Madrid, Spain). A CT scan (512 projections) was performed before whole-body PET imaging at 1 h (mice remained in the scanner after dynamic scan was completed) and 24 h pi, to enable co-registration. PET

data were reconstructed using the two-dimensional ordered subsets-expectation maximization algorithm (2D-OSEM), and corrected for dead time and radioactive decay. Presented whole-body images were generated using Amira® (FEI, Hillsboro, OR, USA) and dynamic scans (brain and heart radioactivity accumulation) and radioactivity distribution in different brain regions were analyzed with PMOD 4.3 (PMOD Technologies LLC, Zürich, Switzerland). The peak concentration of radioactivity over 5 min around the end of IA infusion of $^{89}\text{ZrNB(DFO)}_2$ and $^{89}\text{ZrG4(DFO)}_3(\text{Bdiol})_{110}$ was extracted, and compared with the last 5 min of the dynamic scans to calculate the rate of early clearance of administrated radiotracers from the brain. Then the radioactivity detected in the CNS at 1 h and 24 h after infusion was used to assess their later brain clearance. The effect of OBBBO on nanobody or dendrimer brain accumulation following their IV infusion was evaluated by comparing level of radioactivity 5 min before and 5 min after mannitol administration.

Ex-vivo biodistribution of $^{89}\text{ZrNB(DFO)}_2$ and $^{89}\text{ZrG4(DFO)}_3(\text{Bdiol})_{110}$

Upon completion of PET-CT at 24 h pi of $^{89}\text{ZrNB(DFO)}_2$ or $^{89}\text{ZrG4(DFO)}_3(\text{Bdiol})_{110}$, mice were sacrificed; blood, brain (divided into right and left hemispheres), and selected organs were harvested and weighed. The radioactivity in collected samples was measured on a PerkinElmer 2480 Automatic Gamma Counter (Waltham, MA, USA) 4 days after sample collection to avoid detector saturation due to high radioactivity accumulation in brain and kidneys. To calculate the percent of injected dose per gram of tissue (%ID/g), triplicate radioactive standards (0.01% of the injected dose) were counted along with tissue samples. Biodistribution data shown is mean \pm the standard deviation (SD).

Statistical analysis

PROC MIXED (SAS 9.4) was used for statistical analysis, with the lowest means square (LMS) test for comparison between groups [22]. The statements “repeated” and “random” were used for repeated measures and to express random effects, respectively.

Results

Synthesis of $^{89}\text{ZrNB(DFO)}_2$

Preparation of $^{89}\text{ZrNB(DFO)}_2$ involved conjugation of on average two DFO molecules as measured by MALDI-TOF spectrometry (Fig. S1) and subsequent radiolabeling with Zirconium-89 (Fig. 1). Partition coefficient analysis provided a LogP value of -2.35 for $^{89}\text{ZrNB(DFO)}_2$, indicating that the

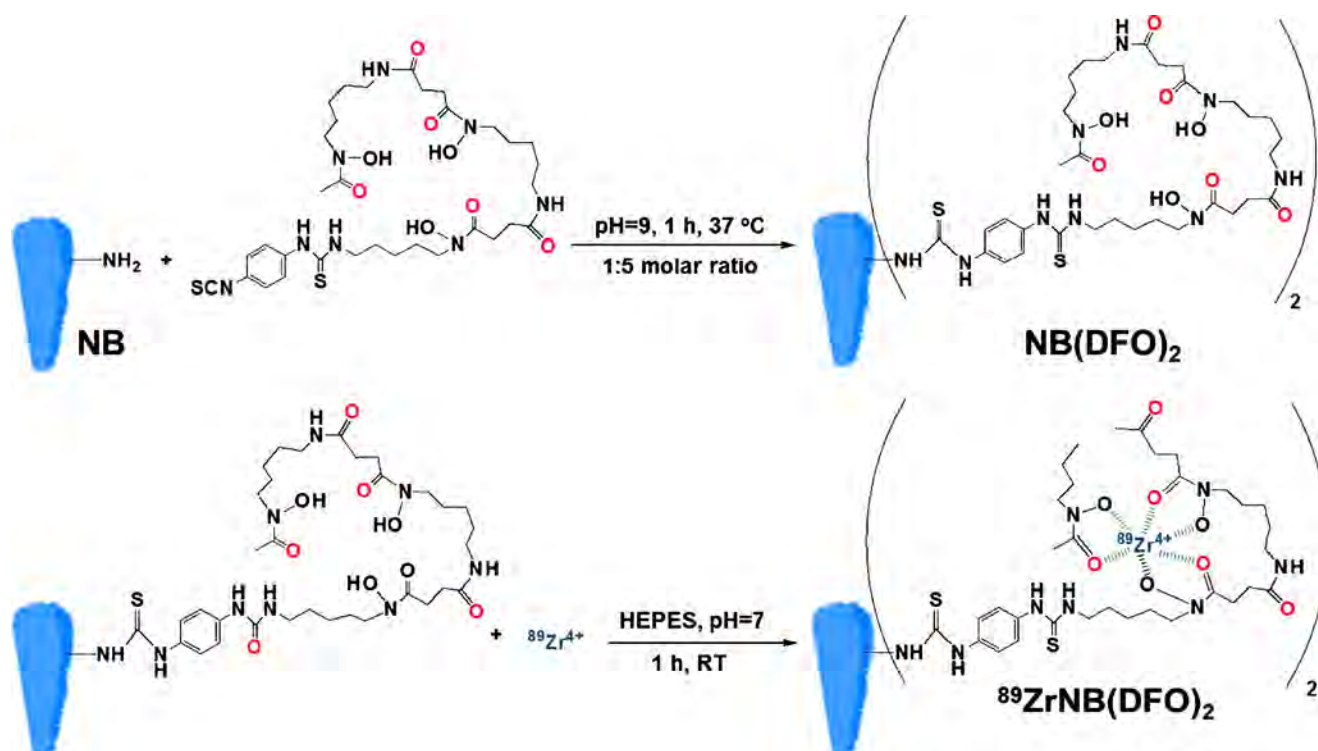


Fig. 1 Conjugation of nanobody with DFO and radiolabeling with ⁸⁹Zr

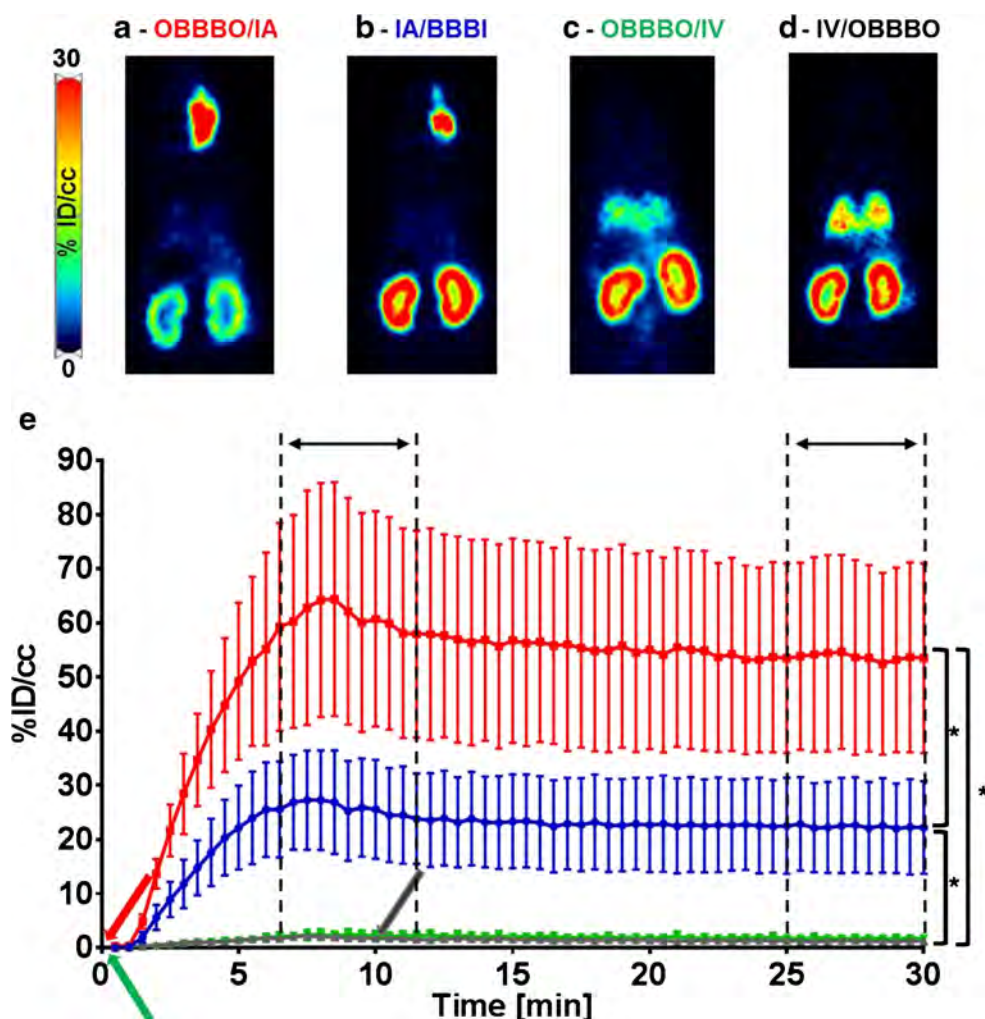
nanobody is hydrophilic, in agreement with the theoretically estimated GRAVY of -0.534 and graph of theoretical hydrophilicity, showing that most of the NB11 molecule is hydrophilic (Fig. S2).

CNS uptake of ⁸⁹ZrNB(DFO)₂ and its biodistribution

Nearly linear uptake of radioactivity in the ipsilateral hemisphere was observed during IA infusions of ⁸⁹ZrNB(DFO)₂ regardless of the BBB status, with no accumulation in the contralateral hemisphere (Fig. 2). The IA/BBBI infusion resulted in ⁸⁹ZrNB(DFO)₂ accumulation in the ipsilateral hemisphere with a peak concentration of 25.79 ± 15.79 %ID/cc, and OBBBO further enhanced its uptake to 60.66 ± 35.41 %ID/cc ($P < 0.05$). Radioactivity in the CNS after IV infusion of ⁸⁹ZrNB(DFO)₂ was at background level regardless of the timing of OBBBO. The background radioactivity after OBBBO/IV and IV/OBBBO remained at a similar level during dynamic scans and in subsequent whole-body PET-CT imaging. For clarity we are not presenting those separately. There was very slow early clearance of radioactivity from the ipsilateral hemisphere over a period of 30 min, which was not significant for IA/BBBI (22.46 ± 15.05 , $P = \text{NS}$), but it was statistically different for OBBBO/IA infusion (53.66 ± 30.73 , $P < 0.05$). The whole-body PET-CT imaging performed 1 h after infusion revealed a similar pattern of radioactivity uptake in the

brain as at the end of the dynamic PET scan, which then decreased nearly by 50%, 24 h after infusion ($P < 0.05$, Fig. 3, Table 1). In all evaluated cohorts, high uptake of radioactivity was also observed in kidneys, indicating renal clearance (Fig. 3 and Table 1). High accumulation of ⁸⁹ZrNB(DFO)₂ in the ipsilateral hemisphere upon OBBBO/IA infusion resulted in its statistically relevant lower concentration in kidneys at 1 h after infusion (26.72 ± 4.19) in comparison to IA/BBBI (43.36 ± 3.83) and IV/OBBBO (39.61 ± 7.51 %ID/cc). The clearance of ⁸⁹ZrNB(DFO)₂ from brain over 24 h resulted in increase of radioactivity in kidneys to 35.38 ± 5.11 %ID/cc in OBBBO/IA group ($P < 0.05$), while no difference was observed for the remaining experimental groups (41.84 ± 5.47 and 40.34 ± 7.91 %ID/cc for IA/BBBI and IV/OBBBO respectively). For IV/OBBBO, 12.48 ± 2.32 %ID/cc of ⁸⁹ZrNB(DFO)₂ could also be detected in the lungs 1 h after infusion. In agreement with PET-CT imaging, post-mortem biodistribution analysis (Fig. 3) revealed significantly higher accumulation of ⁸⁹ZrNB(DFO)₂ in the ipsilateral hemisphere in OBBBO/IA (17.8 ± 5.99 %ID/g) compared to IA/BBBI (6.15 ± 3.53 %ID/g), and IV/OBBBO (0.09 ± 0.03 %ID/g) infusions with negligible radioactivity uptake in the contralateral hemispheres in all mice 24 h after infusion. Among peripheral organs, the highest accumulation of ⁸⁹ZrNB(DFO)₂ was detected in kidneys followed by the spleen, liver, and lungs in all evaluated groups.

Fig. 2 PET imaging and dynamics of [^{89}Zr]NB(DFO) $_2$ uptake in ipsilateral hemisphere. Representative coronal PET images recorded 1 h after infusion, illustrating brain uptake of ^{89}Zr NB(DFO) $_2$ upon: **a** OBBBO followed by immediate IA infusion of 8.5 MBq of ^{89}Zr NB(DFO) $_2$ reconstituted in 1 ml of saline at 0.15 ml/min; **b** IA infusion with BBBI; **c** OBBBO followed by immediate IV infusion; and **d** IV infusion followed by OBBBO at 5 min after radiotracer administration was completed, showing the highest accumulation of radioactivity in ipsilateral hemisphere upon OBBBO/IA; **e** curves demonstrating dynamics of ^{89}Zr NB(DFO) $_2$ uptake in the ipsilateral hemisphere upon OBBBO/IA (red line), IA/BBBI (blue line), OBBBO/IV (green line) and IV/OBBBO (gray line; arrows show time of OBBBO) indicating highest brain uptake of ^{89}Zr NB(DFO) $_2$ in animals treated with OBBBO and IA infusion and lack of its brain accumulation upon IV administration regardless timing of OBBBO. Each time point is presented as mean and SEM, $n = 4$



Synthesis of $^{89}\text{ZrG4}(\text{DFO})_3(\text{Bdiol})_{110}$

$\text{G4}(\text{NH}_2)_{64}$ was conjugated with an average of three molecules of DFO (Fig. 4), and remaining primary amines were substituted with 110 butane-1,2-diol moieties, as assessed by increase of the molecular weight observed in MALDI-TOF spectrometry (Fig. S3A). A one-pot synthesis yielded nanoparticles with narrow size distribution around 5 nm (Fig. S3B) and neutral net-surface charge, indicated by zeta potential of -1.8 mV. Resulting $\text{G4}(\text{DFO})_3(\text{Bdiol})_{110}$ dendrimer was subsequently radiolabeled with ^{89}Zr , and the LogP of -2.84 was measured for resulting $^{89}\text{ZrG4}(\text{DFO})_3(\text{Bdiol})_{110}$, confirming it is hydrophilic.

CNS uptake of $^{89}\text{ZrG4}(\text{DFO})_3(\text{Bdiol})_{110}$ and its biodistribution

There was no difference in the peak concentration of $^{89}\text{ZrG4}(\text{DFO})_3(\text{Bdiol})_{110}$ in the ipsilateral hemisphere for IA/BBBI ($3.29 \pm 1.31\%$ ID/cc) and OBBBO/IA ($3.20 \pm 1.47\%$ ID/cc) infusions ($P = \text{NS}$) as indicated by the

time-activity curves and PET images obtained by summing frames collected between 5 and 10 min of dynamic scans (Fig. 5). This low accumulation of dendrimer in the brain was despite BBB opening at the time of maximum $^{89}\text{ZrG4}(\text{DFO})_3(\text{Bdiol})_{110}$ concentration in the blood pool (Fig. 5a). We did not evaluate the effect of OBBBO prior to IV infusion of dendrimers as for nanobodies. IV/OBBBO infusion resulted in a background radioactivity uptake of $1.22 \pm 0.29\%$ ID/cc in the CNS, with decrease of radioactivity after OBBBO to 1.1 ± 0.25 ($P < 0.05$). The fast and statistically significant clearance of $^{89}\text{ZrG4}(\text{DFO})_3(\text{Bdiol})_{110}$ from the brain was observed regardless of BBB status, reaching 1.68 ± 0.8 , 1.05 ± 0.22 , 0 and $83 \pm 0.18\%$ ID/cc for OBBBO/IA, IA/BBBI, and BBBO/IV respectively, at the end of the dynamic PET scan. However, the clearance after OBBBO/IA was somewhat slower compared to IA/BBBI ($P < 0.05$). IA/BBBI actually dropped to the same low level as IV/OBBBO ($P = \text{NS}$) at the end of the dynamic scans. However, whole-body PET-CT imaging performed 1 h after infusion showed only background radioactivity in the brain

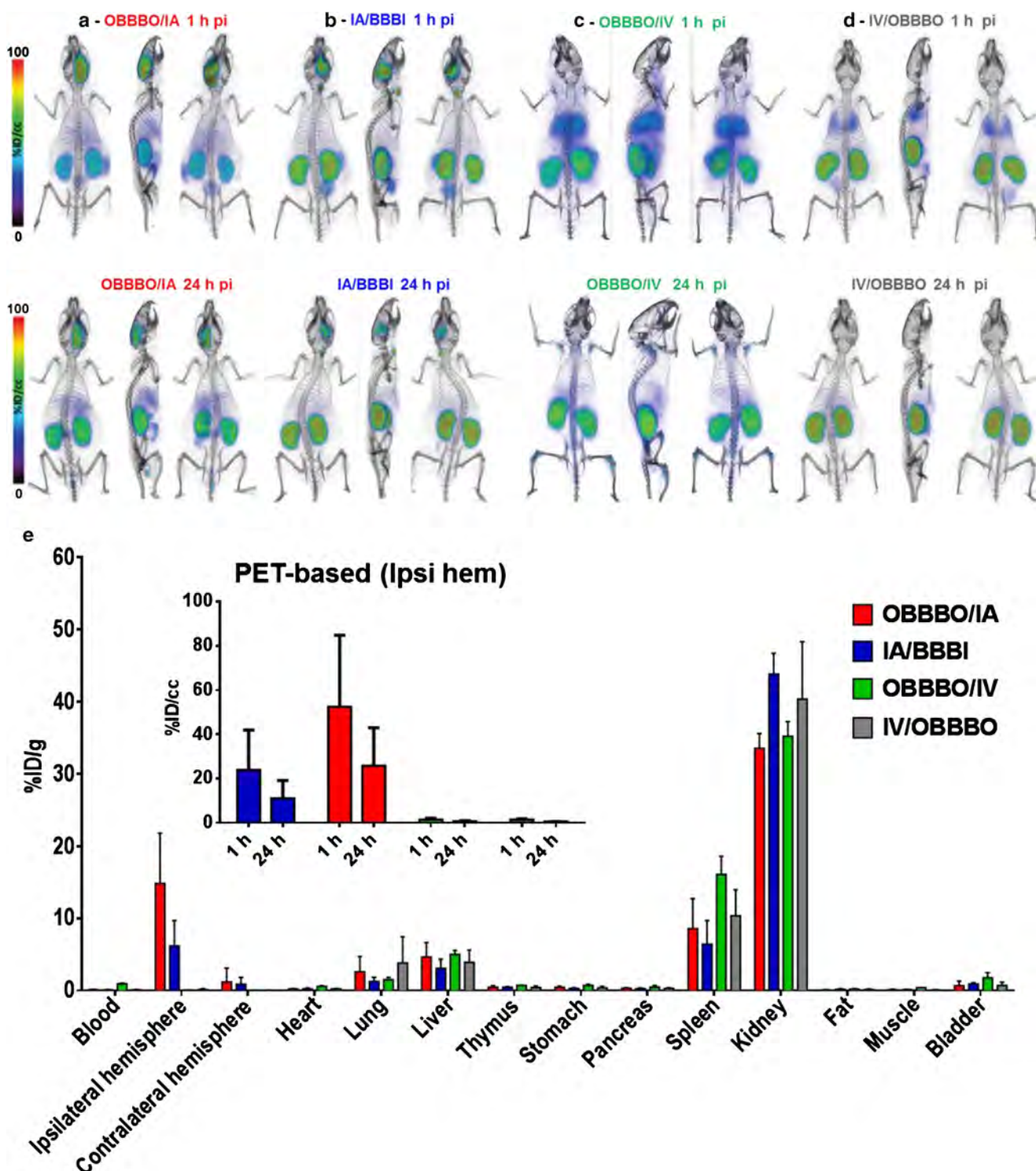


Fig. 3 PET-CT imaging and ex-vivo biodistribution of $^{89}\text{ZrNB}(\text{DFO})_2$ at 24 h after infusion. Whole body volume rendered PET-CT images recorded 1 h and 24 h post infusion of $\sim 8.5 \text{ MBq}$ ($\sim 230 \mu\text{Ci}$) of $^{89}\text{ZrNB}(\text{DFO})_2$, demonstrating its biodistribution upon: **a** OBBBO followed by immediate IA infusion; **b** IA infusion with BBBI; **c** OBBBO followed by immediate IV infusion; and **d** IV infusion followed by OBBBO 5 min after infusion was completed. **e** Ex-vivo biodistribution of $^{89}\text{ZrNB}(\text{DFO})_2$ at

24 h after infusion in the same groups (*insert* - PET-based quantification of $^{89}\text{ZrNB}(\text{DFO})_2$ uptake in ipsilateral hemisphere), showing in agreement with PET imaging higher uptake of $^{89}\text{ZrNB}(\text{DFO})_2$ in ipsilateral hemisphere compared to contralateral hemisphere in OBBBO/IA group and its higher brain accumulation in comparison with IA/BBBI, OBBBO/IV, and IV/OBBBO cohorts

regardless of the route of $^{89}\text{ZrG4}(\text{DFO})_3(\text{Bdiol})_{110}$ delivery, with no statistically significant differences among

groups (Fig. 5c and 6). Significant amounts of radioactivity could be detected in kidneys and bladder, followed by

Table 1 PET-based assessment of $^{89}\text{ZrG4}(\text{DFO})_3(\text{Bdiol})_{110}$ biodistribution

	AI/OBBBO (%ID/cc)	IA/BBBI (%ID/cc)	IV/BBBO (%ID/cc)
1 h after infusion			
Ipsilateral hemisphere	1.9 ± 0.74	1.23 ± 0.33	1.31 ± 0.21
Kidneys	31.09 ± 1.33	66.48 ± 3.51	47.74 ± 2.62
Bladder	35.24 ± 1.85	26.46 ± 15.09	39.38 ± 5.95
Liver	15.82 ± 1.22	26.47 ± 7.48	15.33 ± 0.87
24 h after infusion			
Kidneys	18.61 ± 1.22	21.67 ± 1.59	19.68 ± 1.57
Liver	13.01 ± 2.01	13.91 ± 1.69	12.35 ± 1.56

liver at 1 h after infusion, indicating renal clearance with hepatic involvement. At 24 h after infusion, no radioactivity in the brain of evaluated mice was observed. In agreement with PET-CT imaging, post-mortem biodistribution demonstrated negligible accumulation of $^{89}\text{ZrG4}(\text{DFO})_3(\text{Bdiol})_{110}$ in both hemispheres ($P = \text{NS}$) and presence of radioactivity in kidneys and liver for all assessed delivery routes (Fig. 6). Twenty-four hours after infusion, tracer retention in the ipsilateral hemisphere and bladder was below PET quantification limit.

Discussion

We have shown that the IA route was more effective in delivering nanobodies to the brain than systemic administration, regardless of the BBB status. Preceding OBBBO potentiated brain accumulation of the nanobodies by ~2.5-fold. Brain uptake of $^{89}\text{ZrNB}(\text{DFO})_2$ reached 60.66 ± 35.41 %ID/cc, which is higher compared to brain accumulation of 23.58 ± 4.58 %ID/cc for ^{89}Zr radiolabeled-bevacizumab ($^{89}\text{ZrBVDFO}$) observed in our previous study [6]. While half of the $^{89}\text{ZrNB}(\text{DFO})_2$ was cleared from the brain over 24 h, clearance of $^{89}\text{ZrBVDFO}$ was slower. In both studies, bevacizumab and the nanobody did not have specific targets in mouse brains. Brain retention of generation-4 hydroxy

terminated PAMAM dendrimer was marginal. The peak concentration of $^{89}\text{ZrG4}(\text{DFO})_3(\text{Bdiol})_{110}$ in the brain was only 3 %ID/cc after IA delivery regardless of BBB status, decreasing to background levels within 1 h. Intravenous infusion of $^{89}\text{ZrNB}(\text{DFO})_2$ and $^{89}\text{ZrG4}(\text{DFO})_3(\text{Bdiol})_{110}$ resulted in only background tracer retention regardless of BBB status. Our results are in agreement with previous reports showing negligible penetration of PAMAM dendrimers through intact BBB upon IV administration, regardless of their size and terminal functionalities, including hydroxy, carboxyl, and polyethylene glycol groups [23–25]. Kannan et al. demonstrated uniform accumulation of Cy5 fluorescently labeled generation-4 hydroxy terminated PAMAM dendrimer in a rodent model of gliosarcoma, as well as its specific uptake by tumor-associated macrophages after systemic delivery [17]. Although microscopic imaging was convincing, the peak concentration of dendrimer in tumor reached only ~0.023 %ID/g at 8 h after injection and decreased to ~0.0067 %ID/g 40 h later, as measured by fluorescence spectroscopy of extracted tissue [17]. Similarly, very low brain uptake of ~0.07 %ID/g in neonatal rabbits with cerebral palsy and 0.003 %ID/g healthy control pups for the same dendrimer at 24 h after injection was also reported [26]. Both studies, in agreement with our results, demonstrated marginal BBB permeability and brain retention of generation-4 hydroxy terminated PAMAM dendrimers even with a compromised BBB, brain tumor, or activated

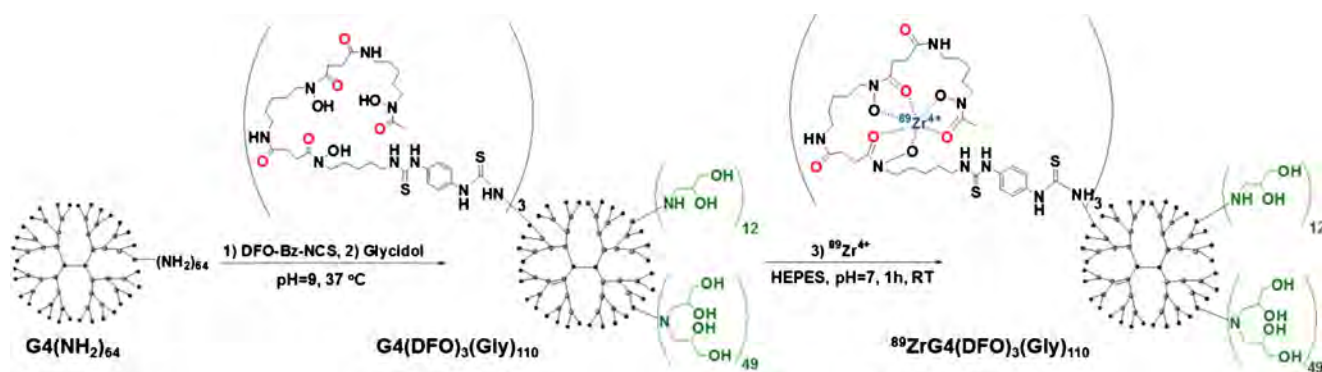
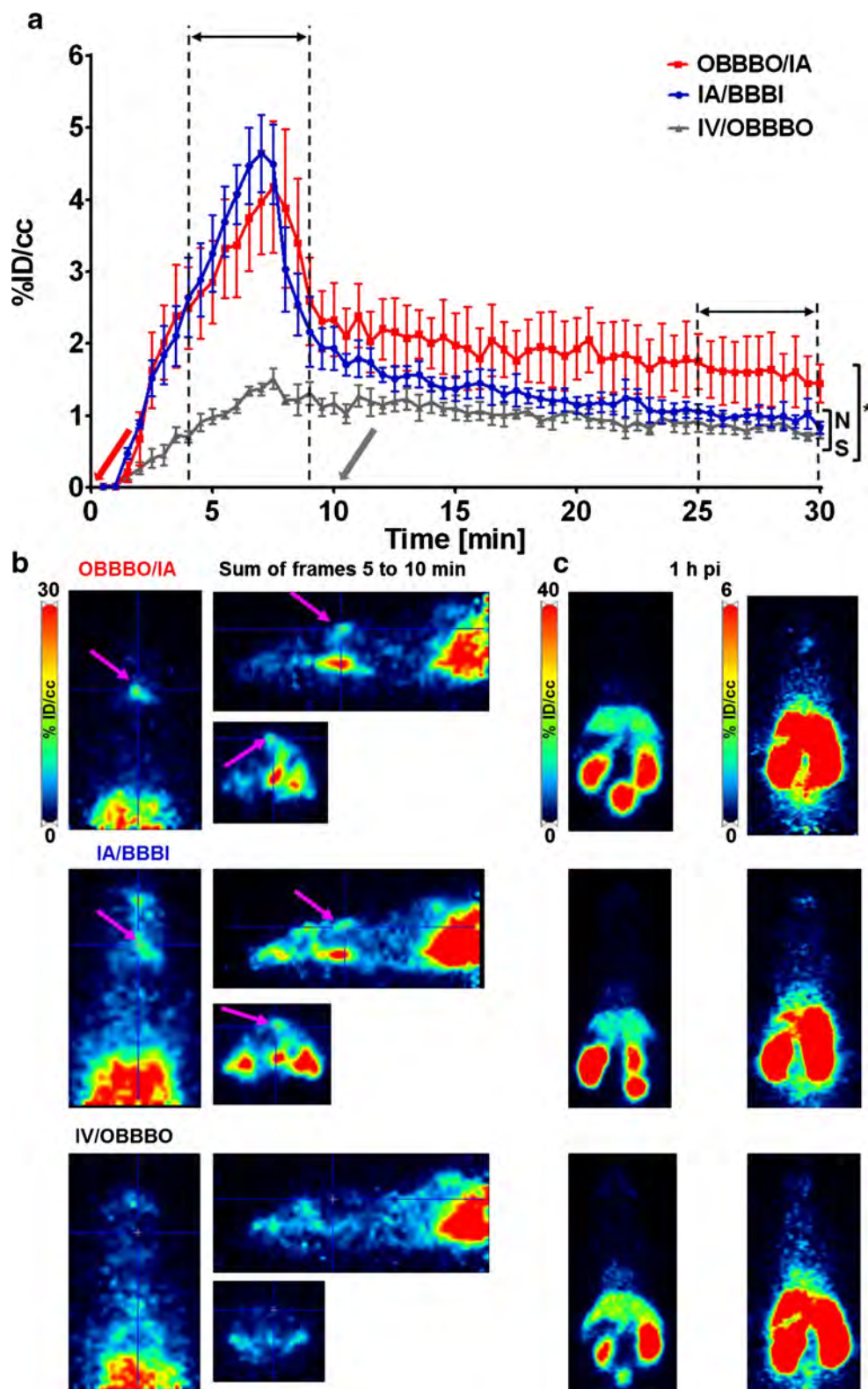


Fig. 4 Conjugation of $\text{G4}(\text{NH}_2)_{64}$ dendrimer with DFO, followed by capping of primary amines with butane-1,2-diol moieties and radiolabeling with ^{89}Zr

Fig. 5 Time–activity curves of $^{89}\text{ZrG4}(\text{DFO})_3(\text{Bdiol})_{110}$ uptake in ipsilateral hemisphere and corresponding PET imaging. **a** Curves demonstrating dynamics of $^{89}\text{ZrG4}(\text{DFO})_3(\text{Bdiol})_{110}$ accumulation in the ipsilateral hemisphere upon OBBBO/IA (red line), IA/BBBI (blue line), and IV/OBBBO (gray line; arrows show when BBB was opened) indicating significantly lower uptake compared to $^{89}\text{ZrNB}(\text{DFO})_2$ and no benefits of OBBBO application. Each time point is presented as mean and SEM, $n = 4$. **b** Representative orthogonal PET images obtained by summing frames between 5 and 10 min acquired during 30 min long dynamic scans. **c** Representative axial PET images with scales adjusted to demonstrate whole body distribution of radioactivity (left panel) and absence of $^{89}\text{ZrG4}(\text{DFO})_3(\text{Bdiol})_{110}$ in the brain (right panel) 1 h after infusion. Results demonstrate negligible retention of $^{89}\text{ZrG4}(\text{DFO})_3(\text{Bdiol})_{110}$ in the brain regardless of BBB status and route of administration



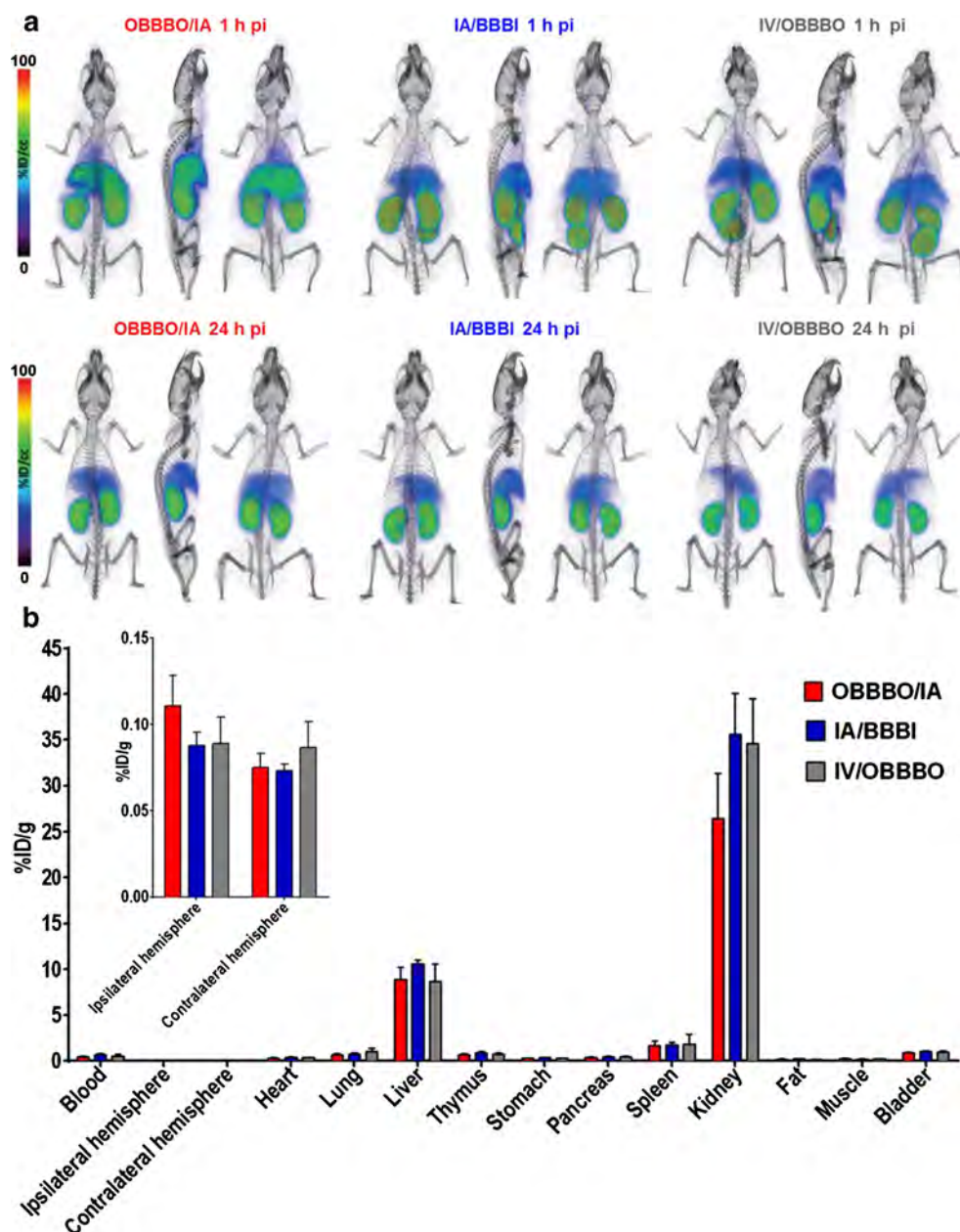
microglia present in cerebral palsy model. Interestingly, PET imaging of generation-4 hydroxy terminated dendrimer-radiolabeled with copper-64 in newborn rabbits with cerebral palsy indicated brain accumulation of radioactivity around 2.5

%ID/cc 24 h after injection [15]. However, copper-64 undergoes trans-chelation in vivo, in particular in the absence of a strong Cu(II) chelator forming thermodynamically stable complexes [27].

Our $^{89}\text{ZrNB}(\text{DFO})_2$ and $^{89}\text{ZrG4}(\text{DFO})_3(\text{Bdiol})_{110}$ were not targeted to specific molecular species within the BBB or the brain. Also, no disease model was induced, enabling testing as a baseline therapeutic delivery platform for CNS drug delivery. In this context, the nanobodies seem attractive for IA infusion, while a lot of caution should be taken regarding utility of PAMAM dendrimers as drug delivery vehicles for brain diseases, especially when they are administered systemically. Therefore, in the case of PAMAM dendrimers the challenge for appropriate surface modification to achieve appreciate brain uptake and retention remains open. While here we tested generation-4 hydroxy terminated PAMAM dendrimers constructed by capping the primary amines with butane-1,2-diol, the same dendrimers with different surface modifications

can potentially exhibit higher brain retention, and our study may serve as a benchmark for quantitative performance of dendrimer-based diagnostics and therapeutics in the CNS diseases. In contrast, the IA route is very effective in delivery of nanobodies, and their relatively fast clearance comparing to antibody could potentially be mitigated by applying nanobodies aimed for a specific brain target. While IV administration is highly ineffective for delivery of nanobodies to the brain, it was recently reported that the intranasal route might be an alternative [28]. However, no quantitative assessment of intranasal brain delivery of nanobodies has been reported yet. There is progress in design of nanobodies against brain disorders [29], and our IA infusion might be a right approach to use them effectively in the clinic. Especially after the anti-tumoral

Fig. 6 PET-CT imaging and ex-vivo biodistribution of $^{89}\text{ZrG4}(\text{DFO})_3(\text{Bdiol})_{110}$. **a** Representative whole body volume rendered PET-CT images recorded 1 h and 24 h post infusion of $^{89}\text{ZrG4}(\text{DFO})_3(\text{Bdiol})_{110}$ for OBBBO/IA, IA/BBBI, and IV/OBBBO infusions. **b** Ex-vivo biodistribution of $^{89}\text{ZrG4}(\text{DFO})_3(\text{Bdiol})_{110}$ at 24 h after infusion in the same mice (*insert* - scale was adjusted to show brain accumulation of $^{89}\text{ZrG4}(\text{DFO})_3(\text{Bdiol})_{110}$, indicating lack of $^{89}\text{ZrG4}(\text{DFO})_3(\text{Bdiol})_{110}$ retention on the brain regardless of method of administration and its renal clearance with minor hepatic uptake



activity of neutralizing antibodies was shown in a mouse model of melanoma, the potentially neutralizing nanobodies could also be created against brain targets [30].

Limitations We have observed relatively high variability in brain uptake of nanobodies after IA delivery. We performed four rounds of experiments, in four groups of animals (IA/BBBI, OBBBO/IA, IV/OBBBO, and OBBBO/IV); and while we observed high reproducibility within rounds with relatively constant ratio of brain uptake OBBBO/IA versus IA/BBBI (ca. 2.5 x), relatively high variability between rounds was observed. No brain uptake and no variability was observed after IV delivery regardless of the timing of BBB opening. Interestingly, in one animal we observed the brain uptake at nearly 100 %ID/cc, which actually shows a high promise for the IA route and the possibility for further improvement of nanobody delivery to the brain. There might be various sources of variability including kinetics of cerebral blood flow or volume of the brain perfused from the IA catheter. It has been recently shown that real-time MRI can increase reproducibility of OBBBO [21]; thus, studies like ours would benefit from PET/MR systems, in which infusion parameters could be adjusted based on feedback from real-time MRI and quantitative assessment of brain uptake of infused molecules based on PET imaging. In a clinical setting, the real-time monitoring of IA delivery of nanobodies to the brain using PET, until the required quantity is achieved, might be an ultimate solution for precise dosing. In our study, we have not measured the affinity of radiolabeled nanobody, as we have not used it to bind a specific target, but it has previously been shown that nanobodies can be radiolabeled without losing their efficacy, providing a proof-of-concept for the viability of our approach [31, 32]. Also, we have not studied mechanisms behind such different penetration of BBB and brain retention of nanobodies vs dendrimers, which have similar basic physicochemical properties such as size, average charge, and hydrophilicity (Table S1). The drastically different in-vivo behavior of NB11 and G4(DFO)₃(Bdiol)₁₁₀ is most likely buried in their different structural composition. The studied nanobody was composed of a large number of amino acids with different side chains enforcing its folding and rigid 3D structure, forming fragments capable of, for example, electrostatic or hydrophobic interactions with biological species, as presented in Fig. S2, showing variable hydrophobicity along sequence of NB11. This may also be the case for antibodies that similarly to nanobodies result in high brain uptake after IA injection. On the contrary, polymeric G4(DFO)₃(Bdiol)₁₁₀ dendrimers, composed of ethane-1,2-diamine, butyraldehyde, and butane-1,2-diol are flexible and only have hydrophilic hydroxy groups in their surface, yielding molecules of highly uniform hydrophilicity. We also did not study compartmentalization or aggregation of nanobodies in the blood following IA administration, which could explain improved accumulation after IA delivery. Since the IV and IA infusion processes are identical in terms of

the infusion speed and duration or catheter size, we did not expect aggregation before or after IA delivery, which could increase the retention in the brain at a cost of reducing biological activity. However, should aggregation have occurred, we would have observed substantial accumulation of the nanobody in the lungs after IV injection. We observed quite the opposite, as a large proportion of the nanobody was routed for renal clearance, as expected for monodispersed nanobodies. Nevertheless, follow-up experiments are warranted, and should be performed in the future to better understand the rules governing the advantages of IA delivery of macromolecules.

Conclusions

We have shown that brain delivery of nanobodies and generation-4 hydroxy terminated PAMAM dendrimers upon IV administration is negligible, regardless of BBB status. The IA route substantially increases brain uptake of nanobodies, which is further potentiated by OBBBO. However, half of the nanobodies are cleared from the brain within 24 h. Designing nanobodies against specific brain targets could ameliorate this deficiency. In contrast, the IA route marginally improved brain delivery of dendrimers, which quickly cleared from CNS. Appropriate surface modification of PAMAM dendrimers may improve their brain uptake and retention.

Funding This work was funded by National Institutes of Health (NIH) R01NS091110, R21NS106436, P41 EB024495.

Compliance with ethical standards

Disclosure of potential conflict of interest JAG has a financial and/or business interests in Gulliver Biomed BVBA, a company that licensed the tested nanobody; however, since the nanobody does not have a brain target there are no direct benefits to Gulliver Biomed. The remaining authors declared no conflict of interest related to the current work.

Ethical approval All animal procedures were carried out under protocols approved by the Johns Hopkins Animal Care and Use Committee. All applicable international, national, and/or institutional guidelines for the care and use of animals were followed. This article does not contain any studies with human participants performed by any of the authors.

References

1. Woodworth GF, Dunn GP, Nance EA, Hanes J, Brem H. Emerging insights into barriers to effective brain tumor therapeutics. *Front Oncol.* 2014;4:126. <https://doi.org/10.3389/fonc.2014.00126>.
2. Mayhan WG, Heistad DD. Permeability of blood–brain barrier to various sized molecules. *Am J Phys.* 1985;248:H712–8. <https://doi.org/10.1152/ajpheart.1985.248.5.H712>.
3. On NH, Miller DW. Transporter-based delivery of anticancer drugs to the brain: improving brain penetration by minimizing drug efflux at the blood–brain barrier. *Curr Pharm Des.* 2014;20:1499–509.
4. Oldendorf WH. Lipid solubility and drug penetration of the blood brain barrier. *Proc Soc Exp Biol Med.* 1974;147:813–5.

5. Boockvar JA, Tsiouris AJ, Hofstetter CP, Kovanlikaya I, Fralin S, Kesavabhotla K, et al. Safety and maximum tolerated dose of superselective intraarterial cerebral infusion of bevacizumab after osmotic blood–brain barrier disruption for recurrent malignant glioma. *Clinical article. J Neurosurg.* 2011;114:624–32. <https://doi.org/10.3171/2010.9.JNS101223>.
6. Lesniak WG, Chu C, Jablonska A, Du Y, Pomper MG, Walczak P, et al. A distinct advantage to intraarterial delivery of 89zr-bevacizumab in pet imaging of mice with and without osmotic opening of the blood–brain barrier. *J Nucl Med.* 2019;60(5):617–22. <https://doi.org/10.2967/jnumed.118.218792>.
7. Banks WA. Characteristics of compounds that cross the blood–brain barrier. *BMC Neurol.* 2009;9(Suppl 1):S3. <https://doi.org/10.1186/1471-2377-9-S1-S3>.
8. Janowski M, Walczak P, Pearl MS. Predicting and optimizing the territory of blood–brain barrier opening by superselective intra-arterial cerebral infusion under dynamic susceptibility contrast MRI guidance. *J Cereb Blood Flow Metab.* 2016;36:569–75. <https://doi.org/10.1177/0271678X15615875>.
9. Lyczek A, Arnold A, Zhang J, Campanelli JT, Janowski M, Bulte JW, et al. Transplanted human glial-restricted progenitors can rescue the survival of dysmyelinated mice independent of the production of mature, compact myelin. *Exp Neurol.* 2017;291:74–86. <https://doi.org/10.1016/j.expneurol.2017.02.005>.
10. Zawadzki M, Walecki J, Kostkiewicz B, Kostyra K, Pearl MS, Solaiyappan M, et al. Real-time MRI guidance for intra-arterial drug delivery in a patient with a brain tumor: technical note. *BMJ Case Rep.* 2019;12:pii: e014469. <https://doi.org/10.1136/bcr-2018-014469>.
11. Ingram JR, Schmidt FI, Ploegh HL. Exploiting Nanobodies' singular traits. *Annu Rev Immunol.* 2018;36:695–715. <https://doi.org/10.1146/annurev-immunol-042617-053327>.
12. Bannas P, Lenz A, Kunick V, Well L, Fumey W, Rissiek B, et al. Molecular imaging of tumors with nanobodies and antibodies: timing and dosage are crucial factors for improved in vivo detection. *Contrast Media Mol Imaging.* 2015;10:367–78. <https://doi.org/10.1002/cmmi.1637>.
13. Kannan RM, Nance E, Kannan S, Tomalia DA. Emerging concepts in dendrimer-based nanomedicine: from design principles to clinical applications. *J Intern Med.* 2014;276:579–617. <https://doi.org/10.1111/joim.12280>.
14. Chauhan AS. Dendrimers for Drug Delivery. *Molecules.* 2018;23:938. <https://doi.org/10.3390/molecules23040938>.
15. Kannan S, Dai H, Navath RS, Balakrishnan B, Jyoti A, Janisse J, et al. Dendrimer-based postnatal therapy for neuroinflammation and cerebral palsy in a rabbit model. *Sci Transl Med.* 2012;4:130ra46. <https://doi.org/10.1126/scitranslmed.3003162>.
16. Balakrishnan B, Nance E, Johnston MV, Kannan R, Kannan S. Nanomedicine in cerebral palsy. *Int J Nanomedicine.* 2013;8:4183–95. <https://doi.org/10.2147/IJN.S35979>.
17. Zhang F, Mastorakos P, Mishra MK, Mangraviti A, Hwang L, Zhou J, et al. Uniform brain tumor distribution and tumor associated macrophage targeting of systemically administered dendrimers. *Biomaterials.* 2015;52:507–16. <https://doi.org/10.1016/j.biomaterials.2015.02.053>.
18. Qiu J, Kong L, Cao X, Li A, Wei P, Wang L, et al. Enhanced delivery of therapeutic siRNA into glioblastoma cells using dendrimer-entrapped gold nanoparticles conjugated with beta-cyclodextrin. *Nanomaterials.* 2018;8:131. <https://doi.org/10.3390/nano8030131>.
19. Van den Abbeele A, De Clercq S, De Ganck A, De Corte V, Van Loo B, Soror SH, et al. A llama-derived gelsolin single-domain antibody gelsolin-G-actin interaction. *Cell Mol Life Sci.* 2010;67:1519–35. <https://doi.org/10.1007/s00018-010-0266-1>.
20. Vosjan MJ, Perk LR, Visser GW, Budde M, Jurek P, Kiefer GE, et al. Conjugation and radiolabeling of monoclonal antibodies with zirconium-89 for PET imaging using the bifunctional chelate p-isothiocyanatobenzyl-desferrioxamine. *Nat Protoc.* 2010;5:739–43. <https://doi.org/10.1038/nprot.2010.13>.
21. Chu C, Liu G, Janowski M, Bulte JWM, Li S, Pearl M, et al. Real-time MRI guidance for reproducible hyperosmolar opening of the blood–brain barrier in mice. *Front Neurol.* 2018;9:921. <https://doi.org/10.3389/fneur.2018.00921>.
22. Tellinghuisen J. Least squares with non-normal data: estimating experimental variance functions. *Analyst.* 2008;133:161–6. <https://doi.org/10.1039/b708709h>.
23. Laznickova A, Biricova V, Laznicek M, Hermann P. Mono(pyridine-N-oxide) DOTA analog and its G1/G4-PAMAM dendrimer conjugates labeled with 177Lu: radiolabeling and biodistribution studies. *Appl Radiat Isot.* 2014;84:70–7. <https://doi.org/10.1016/j.apradiso.2013.10.021>.
24. Sadekar S, Ray A, Janat-Amsbury M, Peterson CM, Ghandehari H. Comparative biodistribution of PAMAM dendrimers and HPMA copolymers in ovarian-tumor-bearing mice. *Biomacromolecules.* 2011;12:88–96. <https://doi.org/10.1021/bm101046d>.
25. Zhang Y, Sun Y, Xu X, Zhang X, Zhu H, Huang L, et al. Synthesis, biodistribution, and microsingle photon emission computed tomography (SPECT) imaging study of technetium-99m labeled PEGylated dendrimer poly(amidoamine) (PAMAM)-folic acid conjugates. *J Med Chem.* 2010;53:3262–72. <https://doi.org/10.1021/jm901910j>.
26. Lesniak WG, Mishra MK, Jyoti A, Balakrishnan B, Zhang F, Nance E, et al. Biodistribution of fluorescently labeled PAMAM dendrimers in neonatal rabbits: effect of neuroinflammation. *Mol Pharm.* 2013;10:4560–71. <https://doi.org/10.1021/mp400371r>.
27. Boswell CA, Sun X, Niu W, Weisman GR, Wong EH, Rheingold AL, et al. Comparative in vivo stability of copper-64-labeled cross-bridged and conventional tetraazamacrocyclic complexes. *J Med Chem.* 2004;47:1465–74. <https://doi.org/10.1021/jm030383m>.
28. Gomes JR, Cabrito I, Soares HR, Costelha S, Teixeira A, Wittelsberger A, et al. Delivery of an anti-transferrin Nanobody to the brain through intranasal administration reveals transferrin expression and secretion by motor neurons. *J Neurochem.* 2018;145:393–408. <https://doi.org/10.1111/jnc.14332>.
29. Samec N, Jovcevska I, Stojan J, Zottel A, Liovic M, Myers MP, et al. Glioblastoma-specific anti-TUFM nanobody for in-vitro immunotargeting and cancer stem cell targeting. *Oncotarget.* 2018;9:17282–99. <https://doi.org/10.18632/oncotarget.24629>.
30. McMurphy T, Xiao R, Magee D, Slater A, Zabeau L, Tavernier J, et al. The anti-tumor activity of a neutralizing nanobody targeting leptin receptor in a mouse model of melanoma. *PLoS One.* 2014;9:e89895. <https://doi.org/10.1371/journal.pone.0089895>.
31. Vaidyanathan G, McDougald D, Choi J, Koumariou E, Weitzel D, Osada T, et al. Preclinical evaluation of 18F-labeled anti-HER2 Nanobody conjugates for imaging HER2 receptor expression by Immuno-PET. *J Nucl Med.* 2016;57:967–73. <https://doi.org/10.2967/jnumed.115.171306>.
32. Bala G, Blykers A, Xavier C, Descamps B, Broisat A, Ghezzi C, et al. Targeting of vascular cell adhesion molecule-1 by 18F-labelled nanobodies for PET/CT imaging of inflamed atherosclerotic plaques. *Eur Heart J Cardiovasc Imaging.* 2016;17:1001–8. <https://doi.org/10.1093/ehjci/jev346>.

Publisher's note Springer Nature remains neutral with regard to jurisdictional claims in published maps and institutional affiliations.



Optimization of osmotic blood-brain barrier opening to enable intravital microscopy studies on drug delivery in mouse cortex

Chengyan Chu^a, Anna Jablonska^{a,b}, Wojciech G. Lesniak^a, Aline M. Thomas^a, Xiaoyan Lan^{a,b}, Raleigh M. Linville^c, Shen Li^d, Peter C. Searson^c, Guanshu Liu^a, Monica Pearl^a, Martin G. Pomper^a, Mirosław Janowski^{a,b}, Tim Magnus^e, Piotr Walczak^{a,b,*}

^a The Russell H. Morgan Department of Radiology and Radiological Science, Johns Hopkins University School of Medicine, Baltimore, MD, USA

^b Department of Diagnostic Radiology and Nuclear Medicine, University of Maryland School of Medicine, Baltimore, MD, USA

^c Institute for Nanobiotechnology, Johns Hopkins University, Baltimore, MD, USA

^d Department of Neurology, Dalian Municipal Central Hospital, Dalian, China

^e Department of Neurology, University Medical Center Hamburg-Eppendorf, Hamburg, Germany

ARTICLE INFO

Keywords:

Blood-brain barrier
Intra-arterial
Mannitol
Two-photon microscopy
Cortex

ABSTRACT

Intra-arterial (IA) infusion of mannitol induces osmotic blood-brain barrier opening (OBBBO) and that method has been used for decades to improve drug delivery to the brain. However, high variability of outcomes prevented vast clinical adoption. Studies on dynamic multi-scale imaging of OBBBO as well as extravasation of IA injected therapeutic agents are essential to develop strategies assuring precision and reproducibility of drug delivery. Intravital microscopy is increasingly used to capture the dynamics of biological processes at the molecular level in convenient mouse models. However, until now OBBBO has been achieved safely in subcortical structures, which prevented direct insight into the process of extravasation through the skull window. Here, we used our previously developed real-time MRI to adjust the procedure to achieve robust cortical OBBBO. We found that catheter-mediated delivery to the cortex from the ipsilateral carotid artery can be improved by temporarily occluding the contralateral carotid artery. The reproducibility and safety of the method were validated by MRI and histology. This experimental platform was further exploited for studying with intravital microscopy the extravasation of 0.58 kDa rhodamine and 153 kDa anti-VEGF monoclonal antibody (bevacizumab) upon IA injection. Dynamic imaging during IA infusion captured the spatiotemporal dynamic of infiltration for each molecule into the brain parenchyma upon OBBBO. Small-sized rhodamine exhibited faster and higher penetration than the antibody. Histological analysis showed some uptake of the monoclonal antibody after IA delivery, and OBBBO significantly amplified the extent of its uptake. For quantitative assessment of cortical uptake, bevacizumab was radiolabeled with zirconium-89 and infused intraarterially. As expected, OBBBO potentiated brain accumulation, providing $33.90 \pm 9.06\%$ of injected dose per gram of brain tissue (% ID/g) in the cortex and $17.09 \pm 7.22\%$ ID/g in subcortical structures. In contrast IA infusion with an intact BBB resulted in $3.56 \pm 1.06\%$ ID/g and $3.57 \pm 0.59\%$ ID/g in the same brain regions, respectively. This study established reproducible cortical OBBBO in mice, which enabled multi-photon microscopy studies on OBBBO and drug targeting. This approach helped demonstrate in a dynamic fashion extravasation of fluorescently-tagged antibodies and their effective delivery into the brain across an osmotically opened BBB.

1. Introduction

The blood-brain barrier (BBB) is a major obstacle for delivery of therapeutics to the central nervous system (CNS), as it prevents brain penetration of > 98% of pharmaceutical agents [1,2]. The BBB is considered as a primary reason why the vast majority of drug trials for CNS disorders fail, while at the time, spectacular progress has been made in

developing treatments for peripheral disorders with malignancies being the best example [3–6]. Intra-arterial (IA) infusion of mannitol has been used for decades for osmotic BBB opening (OBBBO) by disrupting the tight junctions to improve brain uptake of a variety of therapeutic agents including chemotherapeutics [7,8], nanobodies [9] gene vectors [10] and stem cells [11]. Unfortunately, high variability of BBB opening territory and outcomes prevented a vast clinical adoption of this

* Corresponding author at: University of Maryland, Baltimore, 670 W. Baltimore St., HSF III 1176, Baltimore, MD 21201, USA

E-mail address: pwalczak@som.umaryland.edu (P. Walczak).

<https://doi.org/10.1016/j.jconrel.2019.11.019>

Received 1 October 2019; Accepted 16 November 2019

Available online 18 November 2019

0168-3659/ © 2019 Published by Elsevier B.V.

approach [12]. Recently, advances in real-time MRI facilitated visualization and optimization of the local trans-catheter perfusion territory [13] and this approach enabled predictable and reproducible OBBBO [14]. Notably, OBBBO has been shown to have distinct advantage for brain delivery and therapeutic efficacy of anti-angiogenic antibodies (Bevacizumab) in animal models [15] and clinically [16].

These positive developments have revived an interest in IA drug delivery approaches; however, the low spatial resolution of MRI is not sufficient for studying mechanisms of OBBBO. To understand and capitalize on observed high bevacizumab uptake in the brain, it is highly desirable to comprehensively and mechanistically investigate OBBBO and drug extravasation at the microscopic level.

Two-photon microscopy (2 PM) is an intravital imaging technique that allows imaging of tissue up to about one millimeter in depth [17]. Using 2 PM, it is achievable to reach sufficient temporal and spatial resolution in the cerebral cortex to track an agent's penetration across the BBB at the level of microvasculature. Due to limited depth of penetration, 2 PM studies are restricted to superficial structures such as cerebral cortex accessed with an implanted cranial window [18]. However, as we recently reported, OBBBO in mice with intracarotid mannitol infused at the hemodynamically safe rate of ~0.15 ml/min is primarily routed to deep brain structures without perfusion through cerebral cortex [19]. Consequently, OBBBO does not consistently involve cerebral cortex. That phenomenon is likely due to specifics of blood supply and collateralization [20,21]. As such, OBBBO has been out of reach for 2 PM. The main motivation for this study was to develop an approach to enable neurologically-safe OBBBO in the cerebral cortex. We hypothesized that the contralateral common carotid artery (CCA) compensates for the lost blood supply from the catheterized ipsilateral CCA. Therefore, we explored with real-time MRI whether temporary occlusion of the contralateral CCA (cCCA) opened BBB in ipsilateral cortex, and subsequently validated capability of visualization of this process by intravital microscopy using rhodamine and fluorescently labeled bevacizumab. For quantitative assessment of brain uptake, and to confirm whether pharmacologically relevant concentrations are reached, bevacizumab was radiolabeled with zirconium-89 (⁸⁹Zr-bevacizumab) for precise measurements of its biodistribution.

2. Materials and methods

2.1. Animals and endovascular catheterization

All procedures were performed in accordance with guidelines for the care and use of laboratory animals and were approved by the Johns Hopkins Animal Care and Use Committee. Male SCID mice ($n = 38$, 6–8 weeks old, 20–25 g, Jackson Laboratory) were used in this study. The surgical procedures for gaining arterial access were performed as described previously [19]. Briefly, anesthesia was induced with 5% isoflurane and maintained with 1.5–2% isoflurane during surgery. The CCA bifurcation was exposed using blunt dissection. The occipital artery branching off from the external carotid artery (ECA) was coagulated. The ECA and the pterygopalatine artery (PPA) were temporarily ligated with 4-0 silk sutures to route the entire flow into cerebral arteries. A temporary tie was placed on the carotid bifurcation and the proximal CCA was permanently ligated using 4-0 sutures. Before making a small arteriotomy, a suture connecting a weight (25 g) was secured around the contralateral CCA. Then a microcatheter (PE-8-100, SAI Infusion Technologies) was flushed with 2% heparin (1000 units/ml, heparin sodium, Upjohn), inserted into the ipsilateral CCA via the arteriotomy and advanced into the internal carotid artery. The catheter was secured by two purse-string suture ties around CCA.

2.2. Interventional MRI

The mice with IA catheter secured in place were positioned in a Bruker 11.7 T MRI scanner. Baseline T2 (TR/TE = 2500/30 ms), T1

(TR/TE 350/6.7 ms)-weighted and dynamic gradient echo echo-planar imaging (GE-EPI, TR/TE 1250/9.7 ms, field of view (FOV) = 14×14 mm, matrix = 128×128 , acquisition time = 60 s and 24 repetitions) images of the brain were acquired. The microcatheter was connected to a syringe mounted on an MRI compatible programmable syringe pump (PHD 2000, Harvard Apparatus Inc.) for controlled solution administration. Gadolinium (Gd; Prohance) dissolved in saline at 1:50 was infused intra-arterially at the rate of 0.15 ml/min under dynamic GE-EPI MRI for visualization of perfusion territory. For animals where the cortex was not perfused (most cases), the weight around contralateral CCA was engaged, occluding the vessel with dynamic imaging of IA infusion to confirm cortical perfusion/supply.

Once cortical perfusion has been confirmed, 25% mannitol mixed with Gd (50:1) was infused until enhancement indicating BBB breach has been achieved (up to three bolus injections 1–2 min each; interval between infusions is 30 s). For detailed assessment of the BBB status, high resolution T1-weighted scan was collected after mannitol infusion. Three and seven days after OBBBO, the safety of the procedure was evaluated by MRI and then animals were sacrificed for further histological assessment.

2.3. Cranial window implantation

Cranial window procedures were performed as previously described [22]. Briefly, mice were shaved and deeply anesthetized with 1.5–2% isoflurane, and stabilized on a stereotactic frame. Before surgery, animals were administered with dexamethasone sodium phosphate (0.02 ml at 4 mg/ml, Fresenius Kabi) by subcutaneous injection to prevent cerebral edema. Then the skin and periosteum were removed to expose the skull. A craniotomy (~3 mm diameter) was conducted over the right parietal bone ~1.5 mm posterior to bregma and ~1.5 mm lateral from midline. Saline was applied regularly to avoid heating caused by drilling during skull-thinning procedure. At the end, the central island of skull bone was gently lifted, removed, and covered with a circular coverglass (3 mm diameter, #1 thickness, Harvard Biosciences) sealed to the skull using glue. For the subsequent imaging sessions, a custom-made head-bar with a circular opening was sealed to the skull with dental cement, covering all the exposed skull, wound margins and glass edges. Mice were allowed to recover for 7 days before imaging.

2.4. Conjugation of bevacizumab and fluorescein

Bevacizumab was washed 3 times using ultrafiltration with Millipore Amicon Ultra Centrifugal Filters 50 kDa MWCO (Millipore). After washing, the antibody was resuspended in saline at the concentration of 10 mg/ml and pH was adjusted to 9.0 with 0.1 M Na_2CO_3 . NHS-Fluorescein (Thermo Fisher Scientific) was then dissolved in DMSO at the concentration of 10 mg/ml was mixed with antibody at the 1:10 M ratio. Conjugation was carried for 1 h in 37 °C with 160 RPM agitation. The bevacizumab and fluorescein (bevacizumab-FITC) complexes were washed 3 times with saline on the 50 kDa centrifugal filters. Final protein concentration of bevacizumab-FITC and conjugation efficiency were determined by absorbance at 280 nm and 495 nm measured using a NanoDrop (Thermo Fisher Scientific).

2.5. Matrix-assisted laser desorption ionization-time-of-flight (MALDI-TOF)

To determine the average number of fluorescein molecules conjugated with bevacizumab, MALDI-TOF spectra of unmodified antibody and bevacizumab-FITC conjugate was recorded on a Voyager DE-STR spectrophotometer using 2,5-dihydroxybenzoic acid (DHB) as a matrix. First, protein samples were desalted using Zeba™ spin columns 7 kDa MWCO (Thermo Fisher Scientific) and 10 μl elutions were mixed with 10 μl of matrix (10 mg/ml). Then 1 μl of this mixture was placed on the

target plate in triplicate and dried. The mixture was dissolved in 50% methanol (MeOH) and 0.1% trifluoroacetate (TFA) aqueous solution. Number of shots and laser power was adjusted according to spectrum quality (Supplementary Fig. 1).

2.6. Intravital Epi-fluorescence and 2 PM

Before microscopy, isoflurane anesthetized mice ($n = 5$) with cranial window and with arterial access as described above were stabilized in a custom-made frame immobilizing their head. The mice were positioned under an epi-fluorescent microscope and a $10\times$ magnification objective was used for capturing images at frequency of 1–2 Hz. Saline solution of 0.001 mM rhodamine (0.58 kDa) was injected using a syringe infusion pump at the rate of 0.15 ml/min over 1 min via the ICA microcatheter to visualize trans-catheter perfusion. When the cortex was not perfused, the contralateral CCA was closed temporarily for 20 s by engaging the weights.

For 2 PM to visualize OBBBO and drug penetration, mice were placed under a multiphoton microscope (FV1000MPE, Olympus, Tokyo, Japan). A $10\times$ objective (UPlanSApo, 0.40 NA and 3.1 mm working distance) was centered over the cranial window and used to collect time series images of 800×800 pixels (1.59 $\mu\text{m}/\text{pixel}$; 2 $\mu\text{s}/\text{pixel}$; 100 frames) at an estimated depth of 150 μm below the cortical surface. Rhodamine (0.002 mM) mixed with bevacizumab-FITC (0.01 mM) was injected prior to OBBBO to collect baseline data and optimize cortical perfusion (temporary contralateral CCA closure). Then, 25% mannitol mixed with rhodamine and bevacizumab-FITC was delivered at the rate of 0.15 ml/min for 4 mins in total. A common excitation wavelength of 800 nm was used to simultaneously image both dyes during injection and dynamic imaging was continuously performed for 14 mins.

2.7. Histology and immunohistochemistry

For histological evaluation on the safety of OBBBO in the cortex, 7 days after surgery, animals ($n = 4$) were anesthetized and perfused transcardially with 5% sucrose, followed by 4% paraformaldehyde (PFA). The brains were rapidly removed and post-fixed overnight in 4% PFA at 4 °C. The brains were cryopreserved in 30% sucrose and 30- μm thick coronal sections were cryosectioned. Immunohistochemistry for anti-GFAP (1:250, Dako) and anti-Iba1 (1:250, Wako) was performed to assess the neuroinflammation. The secondary antibody was goat anti-rabbit (Alexa Fluor-488, 1:200, Molecular Probes). For detecting the biodistribution of infused bevacizumab, the mice with OBBBO ($n = 4$) and without OBBBO ($n = 3$) were sacrificed 1 h after administration. The brains were cryosectioned at 30 μm and the slices were stained with goat anti-human secondary antibody (Alexa Fluor-488, 1:200, Invitrogen). All the fluorescent images were acquired using an inverted microscope (Zeiss, Axio Observer Z1).

2.8. Radiolabeling of bevacizumab

^{89}Zr labeled bevacizumab was prepared as described recently [15,23]. Briefly, 1 mCi of $^{89}\text{ZrCl}_4\text{O}_8$ was mixed with 20 μl of oxalic acid (1 M) and 25 μl Na_2CO_3 (2 M). After 3 min 200 μl of HEPES containing 1 mg of bevacizumab-deferoxamine conjugate was added. Then, pH of the solution was adjusted to 7 with 2 M Na_2CO_3 , and the mixture was incubated at room temperature for 45 min. Then ^{89}Zr -bevacizumab was purified using Zeba™ Spin Desalting Column (7 kDa MWCO) pre-equilibrated with sterile PBS. ^{89}Zr -bevacizumab was prepared with ~99% radiochemical purity and 35 MBq/mg specific activity. For in vivo studies, ^{89}Zr -bevacizumab was diluted with sterile saline at final concentration 20 $\mu\text{Ci}/\text{ml}$.

2.9. Brain uptake of ^{89}Zr -bevacizumab

Three experimental groups were designed for evaluating ^{89}Zr -bevacizumab biodistribution ($n = 4/\text{each}$). Group 1: IA infusion with contralateral CCA closure (Intact BBB/cCCA closure); Group 2: OBBBO without contralateral CCA closure followed by IA infusion (OBBBO/cCCA patent); Group 3: OBBBO with contralateral CCA closure followed by IA infusion (OBBBO/cCCA closure). OBBBO was induced by 25% mannitol as we described above. Then 0.74 MBq (~20 μCi , total dose of 22 μg) of ^{89}Zr -bevacizumab reconstituted in 1 ml of saline was infused IA over 5 min at the rate of 0.15 ml/min. Upon completion of infusion, the mice were sacrificed, and brain was harvested and divided into right/left hemispheres and further divided into cortex and remaining part of the brain. Each sample was weighed, and the radioactivity was measured using PerkinElmer 2480 Automatic Gamma Counter (Waltham, MA, USA). To calculate the percent of injected dose per gram of brain tissue (%ID/g) and the bevacizumab dose per gram of brain tissue ($\mu\text{g}/\text{g}$), triplicate radioactive standards (0.01% of the injected dose) were counted along with tissue samples.

2.10. Data processing and statistical analysis

Data is expressed as mean \pm SD unless otherwise specified. Quantitation of immunohistochemistry was based on relative fluorescence using Image J and analyzed using a student's paired *t*-test. The ratio of ipsi – /contralateral fluorescence intensity was analyzed using a student's unpaired *t*-test. The MRI analysis of the change in area of the Gd perfusion territory and Gd-enhancement for each mouse was calculated using a custom-written script in MATLAB and analyzed using a paired *t*-test. The post-mortem.

^{89}Zr -bevacizumab quantitation was analyzed using one-way ANOVA followed by Bonferroni post-tests. A *p*-value < .05 was considered significant.

3. Results

3.1. Real-time MRI shows variability of cortical trans-catheter perfusion

Across the 26 mice we found that using infusion rate of 0.15 ml/min, which has been proven as a maximum safe speed [19], we observed variability in cortical involvement. Infusion of a contrast agent (Gd or SPIO) visualized the perfusion territory of the brain as hypointense regions on T2* MRI, which was sampled by GE-EPI scans at a temporal resolution of 2 volumes per second. Such real-time MRI allows precise spatiotemporal visualization of the parenchymal perfusion territory. IA infusion of Gd via ICA with dynamic GE-EPI imaging revealed T2* hypointensity in cerebral cortex (Fig. 1a) at a frequency of 23.07%. The lack of cortical perfusion using this delivery route (Fig. 1b) was observed much more frequently (76.93%). This phenomenon hints at variability of clinical outcomes and is an obvious obstacle complicating 2 PM studies.

3.2. Temporary closure of contralateral CCA facilitates cortical perfusion visualized under real-time MRI

Dynamic GE-EPI scans clearly visualized the biodistribution of IA injected contrast. In animals lacking trans-catheter perfusion through the cortex (drop of T2* signal) temporary closure of the contralateral CCA redistributed the cerebral blood flow opening up the cortex for the catheter infusion (Fig. 2a). The dynamic signal changes for two selected ROIs are shown in Fig. 2b. There was a steep and early drop in the signal intensity in the hippocampus (ROI2), at that time the signal intensity in the cortex (ROI1) remained unchanged and dropped only after temporary closure of the contralateral CCA.

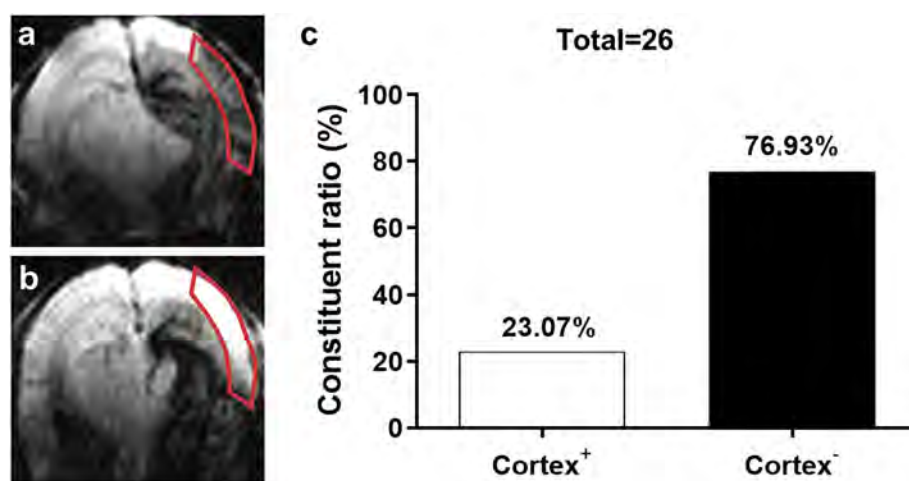


Fig. 1. The variability of cortical involvement during contrast agent infusion via ICA. (a, b) Representative T2* images during infusion of a contrast agent at a rate of 0.15 ml/min wherein the cortex was (a) or was not (b) perfused. (c) The constituent ratio of these phenomena.

3.3. Osmotic disruption of the BBB in cerebral cortex using real-time MRI guidance

Immediately after confirming trans-catheter Gd perfusion in the cortex with IA infusion of the contrast agent (Fig. 3a), IA mannitol was infused using the same parameters. Effective OBBBO was reflected by Gd enhancement on the T1-weighted scan in the region previously highlighted by the contrast infusion (Fig. 3d). To determine the correlation between the Gd perfusion (Fig. 3a) and Gd enhancement (Fig. 3b) MRI, the histograms were drawn and fitted into two Gaussian distributions (Fig. 3b,e). The values that corresponded to the minimal overlap between the two Gaussian functions were chosen to be the threshold that separated the pixels with a significant signal change. Using these thresholds, the areas with significant signal change were determined (Fig. 3c,f). For the four mice studied, the Gd perfusion MRI showed an average signal change area of $27.13 \pm 2.36\%$, while Gd enhancement showed an average signal change area of $26.50 \pm 3.40\%$, which was not significantly different ($P = .663$, Fig. 3g). A strong correlation was shown between these two methods ($R^2 = 0.946$, Fig. 3h). This indicated a successful OBBBO in cortex by

IA mannitol, as predicted by the perfusion pre-scan. Furthermore, the histopathological validation using Evans blue, which is state of the art technique for BBB assessment, displayed a pattern of extravasation that was consistent with MRI (Fig. 3i).

3.4. Safety and long-term consequences of IA mannitol-induced OBBBO in the cortex

Three and seven days after OBBBO, T2w MRI did not detect any asymmetry or hyperintensity, suggesting a lack of edema or inflammation, T2*w scans were not indicative of microhemorrhages and a lack of Gd-enhancement on T1w images revealed an intact BBB (Fig. 4a), overall suggesting that the procedure is safe and the BBB breach was transient. Histology corroborated these observations with GFAP and IBA-1 staining 7 days post OBBBO, in which there was no evidence of astrocytic or microglial activation in the OBBBO region, as determined by comparing the fluorescence intensity between the targeted region and the corresponding area in the contralateral hemisphere ($P = .344$, $P = .073$; Fig. 4b,c). Overall, both MRI and histologic appearance confirmed that the procedure for cortical OBBBO induction

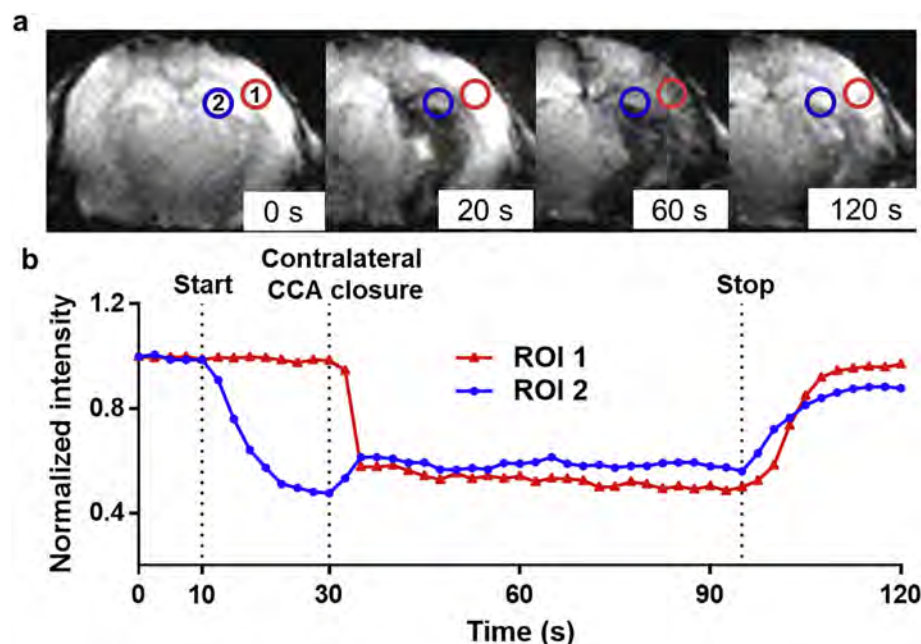


Fig. 2. Use of real-time MRI to visualize the effect of contralateral CCA closure on cortical trans-catheter perfusion. (a) Representative T2* images before (0 s), 20 s, 60 s and 120 s after infusion of Gd at the rate of 0.15 ml/min. (b) Dynamic signal changes for two ROIs marked in (a). Graph lines and ROIs are shown in corresponding colors. Start represents the beginning of IA Gd infusion. Stop represents the end of the infusion.

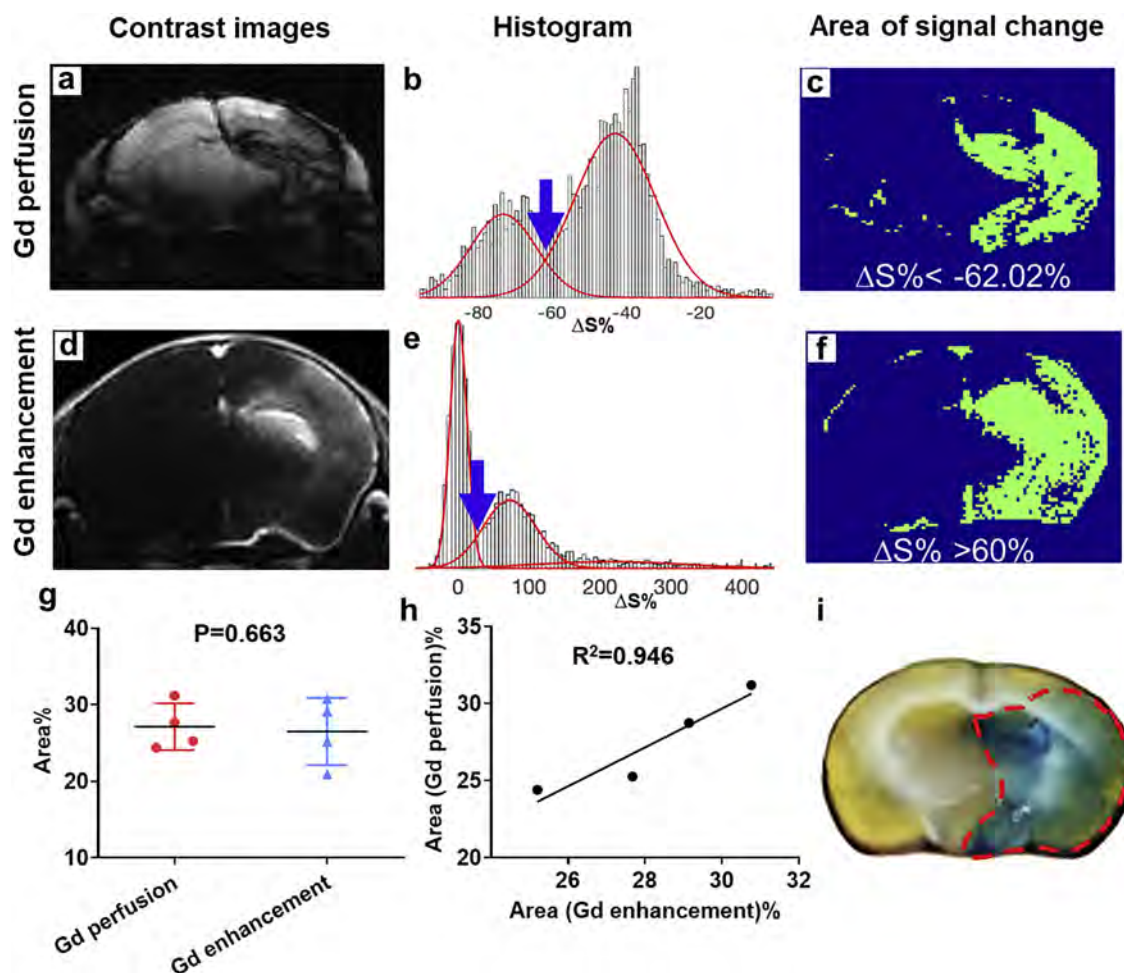


Fig. 3. Real-time MRI for predictable OBBBO with histological validation. (a, d) Representative T2* images of Gd perfusion. (b) Histogram analysis of pixel intensities in (a), showing two Gaussian distributions (red lines). Blue arrow points to where a cut-off of -62.02% was applied to separate the two distributions. (c) Segmented map shows the area where the relative signal change was smaller than -62.02% . (d) Gd enhancement map, (e) histogram analysis, and (f) segmented map ($\Delta S\% > 60\%$) right after mannitol infusion ended. (g) Scatter graph and (h) correlation analysis of the OBBBO territory predicted by Gd perfusion and assessed using Gd enhancement ($n = 4$). (i) The histological analyses show the region with extravasation of Evans blue. (For interpretation of the references to colour in this figure legend, the reader is referred to the web version of this article.)

did not cause brain damage. Notably, excessive exposure to IA mannitol i.e. continuous 4 min-infusion led to brain damage, the injury was shown as T2 hyperintensity on day 3 (Supplementary Fig. 2).

3.5. Vascular trans-catheter perfusion in mouse cortex through a cranial window

With the goal of developing a protocol enabling comprehensive assessment of cortical BBB, including intravital microscopy, we implanted cranial windows and head posts ($n = 5$) (Fig. 5a). After allowing the animals to heal for one week, the mice were catheterized intra-arterially and placed under epi-fluorescent microscopy. Rhodamine was infused via the catheter to verify perfusion and display the cortical vascular architecture. In an agreement with the observation under MRI, cortical perfusion was observed rarely, as visualized during IA infusion bolus of rhodamine (Fig. 5b). In those animals, the dynamic signal changes showed steep increase for the duration of bolus infusion consistently for cortical vessels (Fig. 5c). In the majority of animals, however, sparse or none cerebral arteries and microvessels were perfused and temporary contralateral CCA closure was required to rapidly increase and broaden perfusion territory in the cortex (Fig. 5d, Supplementary Video 1). The dynamic assessment of that scenario is quantitatively represented in Fig. 5e.

3.6. Intravital multiphoton microscopy for visualization of cortical OBBBO and drug extravasation

The cerebral vasculature at $\sim 100 \mu\text{m}$ depth into the cortex was visualized with 2 PM upon IA injection of rhodamine. Once cortical perfusion was achieved, infusion (2 min IA bolus) of a mixture of mannitol, rhodamine and bevacizumab-FITC was initiated; however, infiltration was not observed. Subsequently, another infusion (1 min bolus) was performed, the BBB was breached, and a final infusion (1 min bolus) was performed, for a total of 4 min of infusion time, which resulted in a more robust penetration into the cortical parenchyma (Fig. 6a, Supplementary Video 2). The 0.58 kDa rhodamine extravasated the cortex earlier compared to 153 kDa bevacizumab-FITC. The fluorescence intensity changes in 7 selected ROIs located in the parenchyma was measured to exhibit dynamics of BBB permeability for rhodamine and bevacizumab-FITC. As anticipated, there was earlier onset and higher intensity of extravasation for rhodamine upon BBBO compared to bevacizumab-FITC. The half-time of rhodamine and bevacizumab-FITC reaching their maximum was 526.2 s and 618.6 s, respectively (Fig. 6b).

3.7. Histological confirmation of bevacizumab extravasation

Cryosectioned brain tissue samples collected one hour after IA

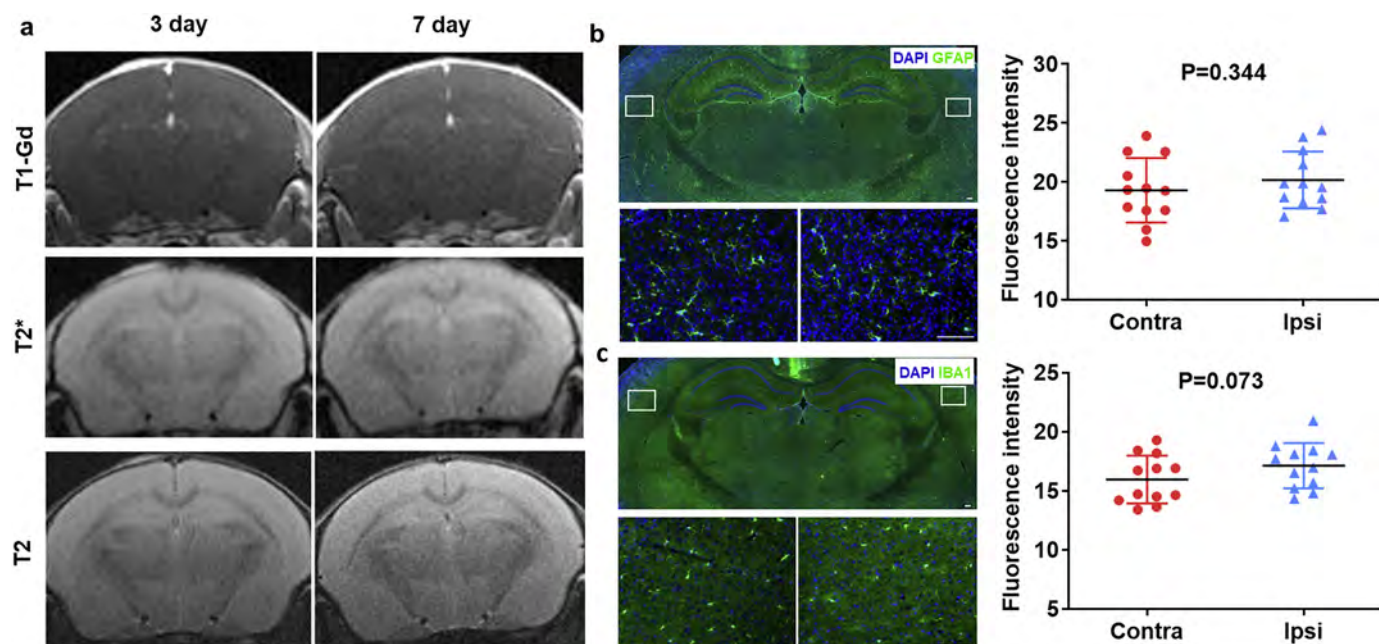


Fig. 4. MRI and histological assessment post-OBBBO. (a) 3 and 7 days after OBBBO, T2-w and T2* w images did not indicate brain damage. No Gd enhancement in T1 images was observed in the brain, revealing that the BBB was resealed. Fluorescent staining of the OBBBO region with GFAP (b) and IBA1 (c) showed comparable intensity between the ipsilateral and the contralateral hemisphere (3 ROIs/hemisphere as represented in lower magnification), indicating no inflammation after OBBBO. Scale bar = 100 μ m.

delivery of bevacizumab with intact BBB (BBBI) showed modestly increased uptake of bevacizumab delivery to the target (ipsilateral side), however, it was localized to the blood vessels (Fig. 7a). For the IA delivery with OBBBO, accumulation of bevacizumab was observed in both

blood vessels and parenchyma (Fig. 7b). Additionally, OBBBO appeared to potentiate the vascular concentration of bevacizumab. As measured by the fluorescence intensity, there was significantly higher uptake of bevacizumab in ipsilateral vs. contralateral hemisphere in both groups

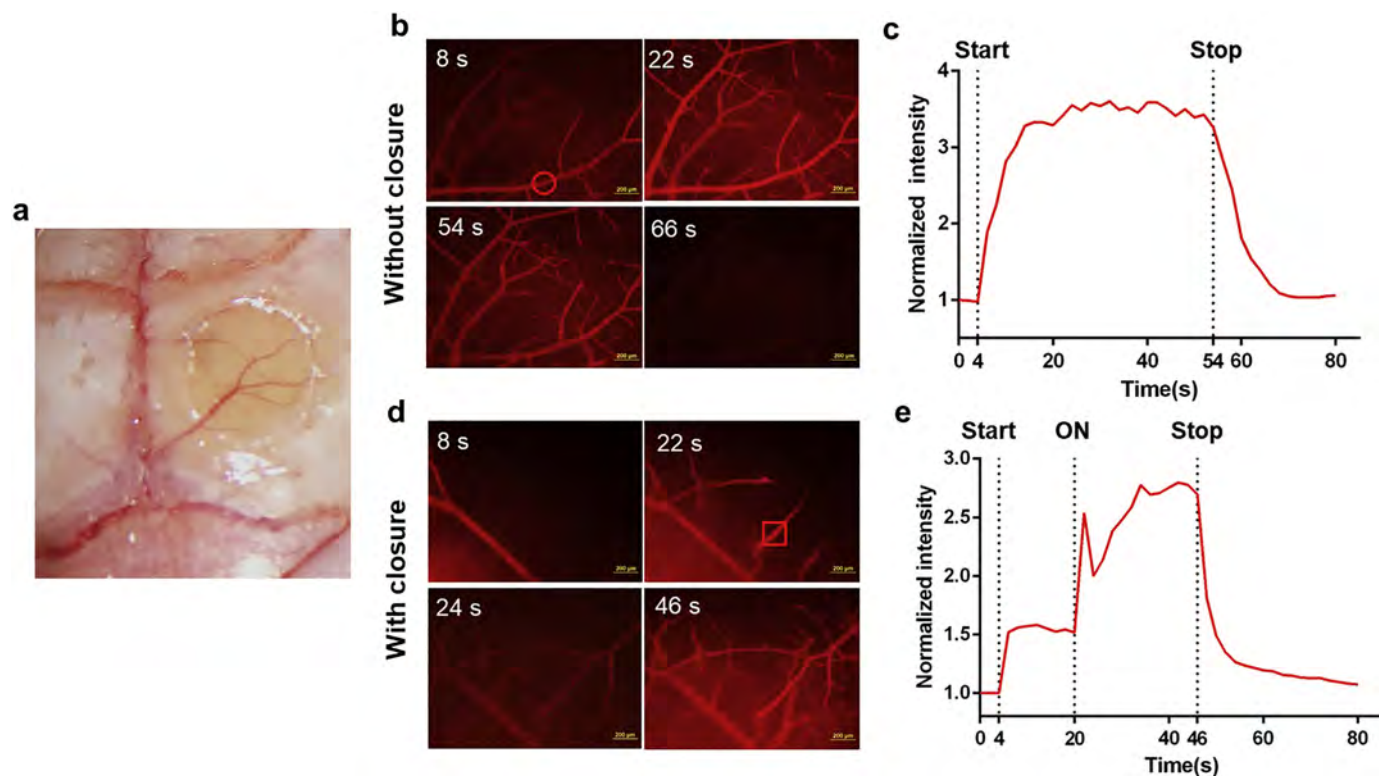


Fig. 5. Visualization of cortical perfusion in epifluorescence microscopy. (a) The cranial window for microscopic imaging. (b) Representative fluorescent images show the perfusion territory of rhodamine without contralateral CCA closure. (c) Dynamic signal changes of the ROI (circle) marked in (b). (d) Representative fluorescent images show the change of perfusion territory in the cortex pre- and post-contralateral CCA closure. (e) Dynamic signal changes of the ROI (square) marked in (d). Start represents the beginning of rhodamine infusion. ON represents the weight is engaged. Stop represents the end of the infusion.

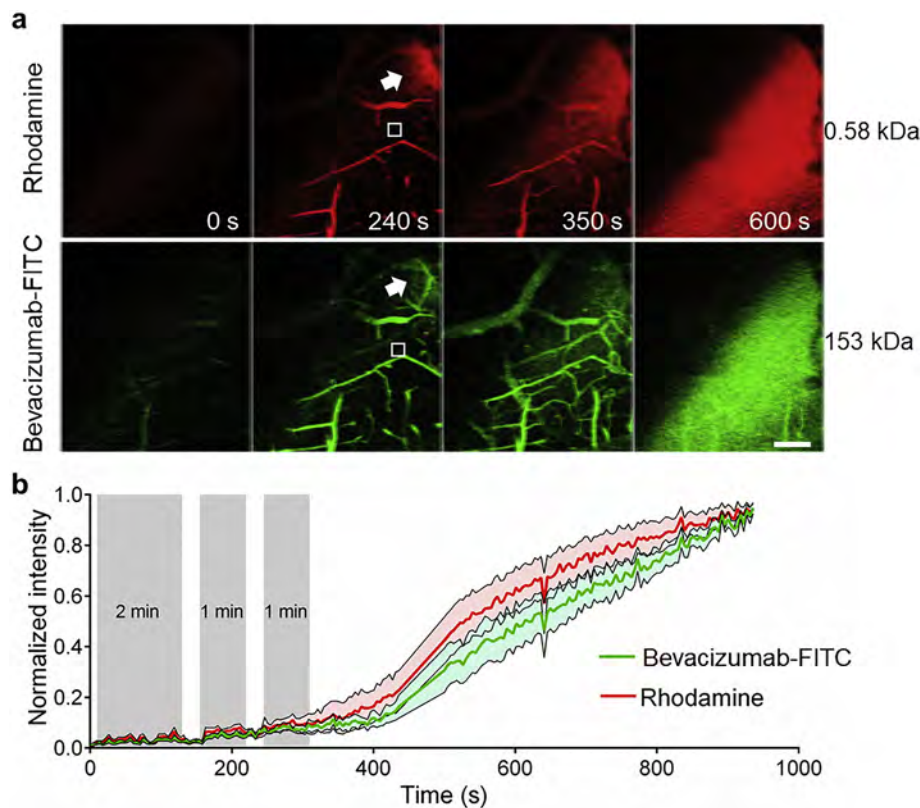


Fig. 6. Intravital 2 PM visualization of cortical OBBBO and drug extravasation. (a) Representative 2 PM images showed the vessels permeability to rhodamine and bevacizumab. The arrow points to where BBB disruption started. (b) Quantitative measurement of fluorescent signal intensities in the selected extravascular regions marked in (a) over 15 min long dynamic imaging. The data was presented as mean \pm SEM from 7 ROIs. The grey shading indicated the IA infusion periods. Scale bar = 50 μ m.

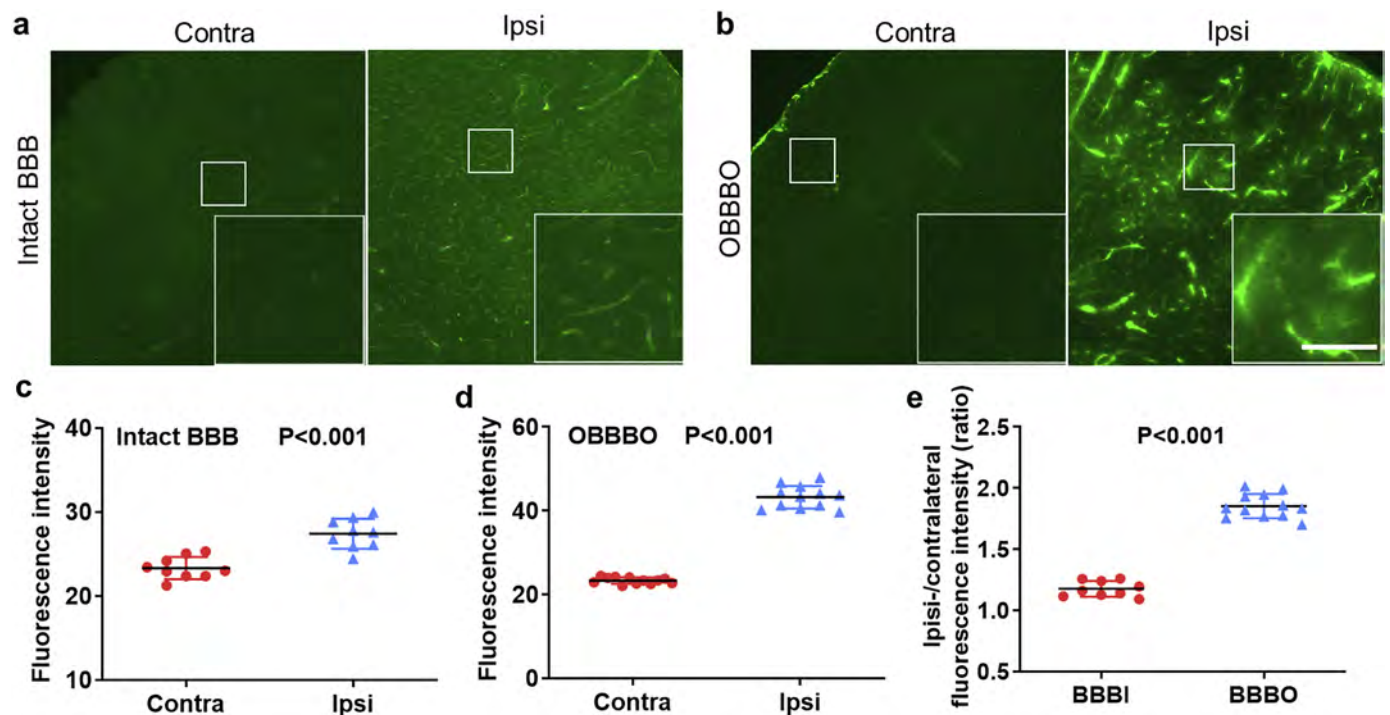


Fig. 7. Histological assessment of bevacizumab biodistribution and extravasation. (a, b) Coronal fluorescent images of mouse cerebral cortex showed the distribution of infused bevacizumab in animals with intact BBB and OBBBO. (c, d) Quantification of fluorescence intensity of bevacizumab between the ipsilateral and contralateral hemisphere. (e) The ipsi-/contralateral ratio values were higher when the BBB was opened compared to that in animals with intact BBB. Measurements are sampled from 3 ROIs/hemisphere as represented in lower magnification. Scale bar = 50 μ m.

($P < .001$, Fig. 7c, d), but the ipsi-/contralateral ratio was more pronounced (~ 2 fold higher) when the BBB was opened ($P < .001$, Fig. 7e). These observations demonstrated that IA delivery of bevacizumab into the brain across an osmotically opened BBB is more

effective compared to the intact BBB (BBBI).

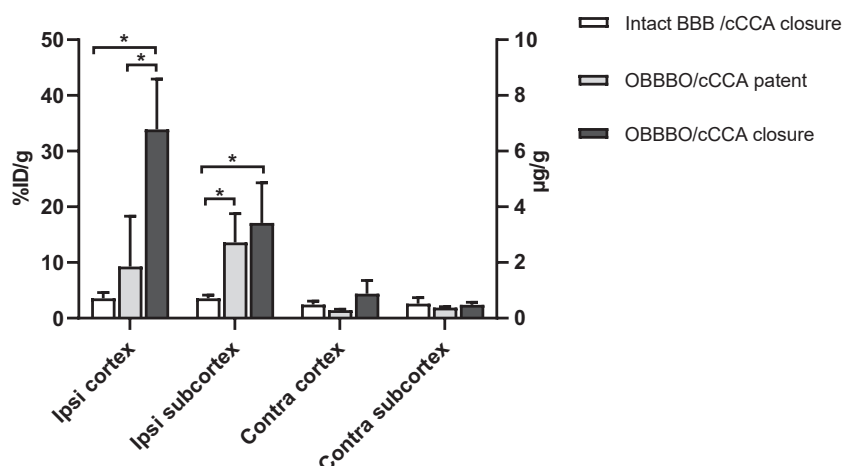


Fig. 8. Brain uptake of ^{89}Zr -bevacizumab. Ex vivo biodistribution analysis showed brain uptake of ^{89}Zr -bevacizumab with significantly higher uptake in the ipsilateral cortex in OBBBO/cCCA closure group ($n = 4$). *Statistically significant difference.

3.8. Brain uptake of ^{89}Zr -bevacizumab

To further quantitate brain uptake of injected antibody, ^{89}Zr -bevacizumab was evaluated using ex vivo biodistribution assay (Fig. 8, Supplemental Tables 1, 2). We found the uptake of ^{89}Zr -bevacizumab in the ipsilateral cortex reached $33.90 \pm 9.06\% \text{ID/g}$ ($7.46 \pm 1.99 \mu\text{g/g}$), which was significantly higher than that in the intact BBB/cCCA closure group ($3.56 \pm 1.06\% \text{ID/g}$; $0.78 \pm 0.23 \mu\text{g/g}$) and OBBBO/cCCA patent group ($9.29 \pm 9.02\% \text{ID/g}$; $2.04 \pm 1.99 \mu\text{g/g}$). No statistically significant difference was found between these two groups. In the ipsilateral subcortical structures, the uptake of ^{89}Zr -bevacizumab reached $13.59 \pm 5.19\% \text{ID/g}$ ($2.99 \pm 1.14 \mu\text{g/g}$) and $17.09 \pm 7.22\% \text{ID/g}$ ($3.76 \pm 1.59 \mu\text{g/g}$) in the group of OBBBO/cCCA patent and OBBBO/cCCA closure, respectively. While in the intact BBB/cCCA closure group, we observed much lower uptake of $3.57 \pm 0.59\% \text{ID/g}$ ($0.79 \pm 0.13 \mu\text{g/g}$). In addition, after IA infusion, the uptake in the ipsilateral hemisphere (both the cortex and subcortical structures) was markedly higher than that in the contralateral hemisphere regardless of BBB status.

4. Discussion

Intra-arterial hyperosmotic mannitol has been used for decades to induce transient permeabilization of the BBB for enhancing drug delivery to the brain. However, due to the unpredictable and non-selective opening, this approach provide variable outcomes [12,16], preventing its broad clinical adaptation. Our previous studies have proved the superiority of real-time MRI guidance, facilitating highly predictable and spatially precise endovascular targeting of the brain to induce OBBBO and deliver therapeutics [13,14,19,24]. There is growing demand for this type of technology due to the rapidly growing field of endovascular neurointerventions. Indeed, we have recently applied this approach clinically in a patient with aggressive recurrent glioblastoma multiforme [16]. Real-time MRI guidance of IA delivery was essential to maximize tumor exposure with bevacizumab following mannitol infusion, resulting in an encouraging therapeutic response [16]. Additionally, our positron emission tomography (PET) imaging study demonstrated that IA route is far more effective in delivering monoclonal antibodies into the brain compared to systemic administration and the antibodies retained in the brain for at least 24 h [15]. However, the relatively low spatial resolution PET data from that study precluded assessment as to whether the accumulation was solely on the endothelial level or the antibodies penetrated into the brain parenchyma. Here, we focused on optimizing IA drug delivery in mice to facilitate multi-scale dynamic imaging studies of OBBBO and determine the

amount of infused drug uptake in targeted region.

OBBBO in mice has been previously reported and several studies showed successful BBB breach in the entire hemisphere including the cortex [10,25,26]; however, those published studies utilized a high IA infusion rate exceeding the safe physiological perfusion rate for the carotid artery, and it has been reported by us and others that excessive infusion rate has a direct damaging effect on the BBB and the brain [19,24,27,28]. We previously optimized the procedure for safe, transient opening of the BBB without neurological consequences but the territory of BBB opening rarely included the cortex. This phenomenon is likely due to redundancy in vascularization of the cortex supplied by more than one major cerebral artery eventually leading to mixing and dilution of IA mannitol [29,30]. In order to prevent this situation, here, we temporarily occluded the contralateral CCA for the duration of mannitol injection and that intervention was sufficient for the ipsilateral cortex to be perfused from the catheter and therefore disrupt the cortical BBB as shown by real-time MRI. This experimental platform was then exploited for studying the mechanism of drug extravasation using intravital microscopy. Dynamic imaging during IA infusion allowed us to visualize and track the leakage of fluorescent dyes upon OBBBO, showing that rhodamine extravasated earlier and led to higher parenchymal accumulation than monoclonal antibody. This observation is consistent with a study of focused ultrasound (FUS)-induced BBBO reported by Nhan. et al., which demonstrated fast leakage for small sized molecules [31]. Indeed, FUS is emerging as a novel non-invasive technology for BBB opening to enhance delivery of therapeutics into the brain [32–35]. This approach, especially when performed under MRI-guidance, has excellent spatial control; however, the strategy needs to overcome the potential adverse of sterile inflammation before being widely implemented in clinical trials [36]. Furthermore, FUS-induced BBBO in the brain parenchyma is usually combined with systemic administration of therapeutics, making it difficult to reach sufficient drug concentration at the targeted site and often resulting in toxic side effects. In contrast, IA approach combining selective OBBBO immediately followed by localized delivery of a specific drug during the same procedure as a one-stop-shop affords adequate therapeutic concentration at the desired destination while minimizing systemic exposure.

Microscopic analysis in this study (both intravital and post mortem) provided information about the timing of BBB breach as well as parenchymal penetration of injected antibodies, further explaining our previous PET findings [15] and other literature reports [7,37,38]. After IA delivery antibodies with an intact BBB were found to localize within blood vessels, while parenchymal presence was negligible. This is consistent with published literature showing extravasation of

antibodies without BBBO is marginal [15,39–41]. Notably, OBBBO paired with intravenous delivery of antibodies also results in poor brain accumulation [15].

IA mannitol with coordinated closure of the contralateral CCA facilitated cortical OBBBO; however, for effective BBB disruption longer exposure to mannitol (around 3 min) was required compared to subcortical structures. This phenomenon may result from the mixing and dilution of mannitol or differences in structure and function of cortical capillaries. Our dynamic intravital microscopy supported the mixing theory, where we observed the intermittent pulsatile flow pattern during IA infusion of the contrast agent (Supplementary Video 2). The structure and function of the microvessels may also contribute to differences in vulnerability to mannitol. Tissue-engineered models of the human BBB, which recapitulate shear stress, geometry, and physiological permeability have recently emerged as a platform to study BBBO [42]. Within 3D BBB microvessels, mannitol-induced BBBO was observed to be heterogeneous, occurring due to disruption of discrete cell-cell junctions between adjacent iPSC-derived brain microvascular endothelial cells [43].

The multi-scale imaging studies reported here are essential for developing precise, reproducible, and effective strategies for drug targeting. Even in the case of direct intracerebral injection of small molecules, based on convection-enhanced delivery (CED), drug retention in the brain is uncertain. A recent PET study surprisingly reported that CED of low molecular weight molecules resulted in their rapid clearance [44]. The mechanism of that rapid clearance is not well understood but the BBB functionality includes active efflux transporting molecules out of the CNS [45]. Meanwhile, this finding might also explain the limited efficacy of therapies when BBB permeable small molecules were used to treat CNS disorders, as they seem to be easily transported into peripheral circulation, resulting in inadequate therapeutic concentrations at the target. Hence, our developed platform for intravital imaging in the cortex will be of great value to accurately understand the drug behavior in the brain parenchyma with or without BBBO, profoundly contributing to the development of drug delivery strategies.

Monoclonal antibodies constitute a source of therapeutic agents used increasingly in oncology and for many other disorders. However, the high molecular weight (around 150 kDa) leads to their poor diffusion across the BBB, resulting in limited therapeutic efficacy for the diseases affecting CNS. Drug concentrations in the CNS are notoriously low with an example of a clinical study showing that the concentration of a monoclonal antibody (trastuzumab) in the cerebrospinal fluid (CSF) was very low (0.21 mg/l versus 70.32 mg/l in the serum) [46]. In another report monoclonal antibody (rituximab) in the CSF was detected at around 1% of the blood concentration after the dose of 800 mg administered intravenously [47]. In a preclinical study using mice bearing an orthotopic diffuse intrinsic pontine glioma, Jansen et al. [48] reported no visible accumulation of ⁸⁹Zr-bevacizumab on PET imaging either in the brain nor in tumors. Ex vivo quantitative assessment showed the uptake was below 1%ID/g. Such poor uptake requires extremely high dose of systemic drug for achieving any therapeutic effect. As shown in a study using U87 brain tumor model, the tumor growth was inhibited only after the dose of bevacizumab reached 10 mg/kg [49]. Here, we demonstrated that IA delivery could increase the uptake up to 3.6%ID/g. OBBBO further improve the uptake to 33.90%ID/g in the ipsilateral cortex and 17.09%ID/g for ipsilateral subcortical structures. Although high uptake of bevacizumab in the brain reached pharmacologically relevant concentration, this study utilized intact animals and future experiments with brain tumor models are needed to identify the therapeutic dose and analyze the treatment effects. Notably, in contrast to parenchymal delivery requiring neurosurgical procedure, endovascular treatment can be easily performed multiple times if required.

Overall, this study established reproducible cortical OBBBO in mice, which enables multi-photon microscopy studies on OBBBO and drug

targeting. This approach enabled the real-time monitoring of the extravasation of IA injected antibodies and proved utility of this approach for effective delivery of antibodies into the brain across osmotically opened BBB. Such a platform will be critical for designing and guiding treatment strategies for a variety of neurological disorders.

Supplementary data to this article can be found online at <https://doi.org/10.1016/j.jconrel.2019.11.019>.

Author contributions

CC, AJ, WGL, MJ, SL, MP, TM and PW conception and design. CC, AJ, XL and PW acquisition of data. CC, AJ, GL, AMT, RML, PCS, MJ, SL, MP and PW analysis and interpretation of data. CC draft of the manuscript. All authors revision and final approval.

Funding

This study was supported by 2017-MSCRFD-3942, 2019-MSCRFD-5031, NIH R01NS091110, R01NS102675 R21NS091599.

Declaration of Competing Interest

PW, MJ and MP are founders and hold equity in IntraArt, LLC and TiCom, LLC. This arrangement has been reviewed and approved by the Johns Hopkins University in accordance with its conflicts of interest policies.

Acknowledgements

RML acknowledges a National Science Foundation Graduate Research Fellowship under Grant No. DGE1746891.

References

- [1] G.W. Goldstein, A.L. Betz, The Blood-Brain-Barrier, *Sci. Am.* 255 (1986) 74–8.
- [2] W.M. Pardridge, The blood-brain barrier: bottleneck in brain drug development, *NeuroRx* 2 (2005) 3–14.
- [3] R.K. Oberoi, K.E. Parrish, T.T. Sio, R.K. Mittapalli, W.F. Elmquist, J.N. Sarkaria, Strategies to improve delivery of anticancer drugs across the blood-brain barrier to treat glioblastoma, *Neuro-Oncology* 18 (2016) 27–36.
- [4] V.K. Gribkoff, L.K. Kaczmarek, The need for new approaches in CNS drug discovery: why drugs have failed, and what can be done to improve outcomes, *Neuropharmacology* 120 (2017) 11–19.
- [5] W.A. Banks, From blood-brain barrier to blood-brain interface: new opportunities for CNS drug delivery, *Nat. Rev. Drug Discov.* 15 (2016) 275–292.
- [6] K. Aldape, K.M. Brindle, L. Chesler, R. Chopra, A. Gajjar, M.R. Gilbert, N. Gottardo, D.H. Gutmann, D. Hargrave, E.C. Holland, D.T.W. Jones, J.A. Joyce, P. Kearns, M.W. Kieran, I.K. Mellingerhoff, M. Merchant, S.M. Pfister, S.M. Pollard, V. Ramaswamy, J.N. Rich, G.W. Robinson, D.H. Rowitch, J.H. Sampson, M.D. Taylor, P. Workman, R.J. Gilbertson, Challenges to curing primary brain tumors, *Nat. Rev. Clin. Oncol.* 16 (8) (2019) 509–520.
- [7] S.I. Rapoport, Advances in osmotic opening of the blood-brain barrier to enhance CNS chemotherapy, *Expert Opin. Investig. Drugs* 10 (2001) 1809–1818.
- [8] D.F. Kraemer, D. Fortin, E.A. Neuwelt, Chemotherapeutic dose intensification for treatment of malignant brain tumors: recent developments and future directions, *Curr. Neurol. Neurosci. Rep.* 2 (2002) 216–224.
- [9] W.G. Lesniak, C. Chu, A. Jablonska, B. Behnam Azad, O. Zwaenepoel, M. Zawadzki, A. Lisok, M.G. Pomper, P. Walczak, J. Gettemans, M. Janowski, PET imaging of distinct brain uptake of a nanobody and similarly-sized PAMAM dendrimers after intra-arterial administration, *Eur. J. Nucl. Med. Mol. Imaging* 46 (9) (2019) 1940–1951.
- [10] C.P. Foley, D.G. Rubin, A. Santillan, D. Sondhi, J.P. Dyke, R.G. Crystal, Y.P. Gobin, D.J. Ballon, Intra-arterial delivery of AAV vectors to the mouse brain after mannitol mediated blood brain barrier disruption, *J. Control. Release* 196 (2014) 71–78.
- [11] S. Cerri, R. Greco, G. Levandis, C. Ghezzi, A.S. Mangione, M.T. Fuzzati-Armentero, A. Bonizzi, M.A. Avanzini, R. Maccario, F. Blandini, Intracarotid infusion of mesenchymal stem cells in an animal model of Parkinson's disease, focusing on cell distribution and neuroprotective and behavioral effects, *Stem Cells Transl. Med.* 4 (2015) 1073–1085.
- [12] S. Joshi, A. Ergin, M. Wang, R. Reif, J. Zhang, J.N. Bruce, I.J. Bigio, Inconsistent blood brain barrier disruption by intraarterial mannitol in rabbits: implications for chemotherapy, *J. Neuro-Oncol.* 104 (2011) 11–19.
- [13] P. Walczak, J. Wojtkiewicz, A. Nowakowski, A. Habich, P. Holak, J. Xu, Z. Adamiak, M. Chehade, M.S. Pearl, P. Gailloud, B. Lukomska, W. Maksymowicz, J.W. Bulte, M. Janowski, Real-time MRI for precise and predictable intra-arterial stem cell

- delivery to the central nervous system, *J. Cereb. Blood Flow Metab.* 37 (7) (2016) 2346–2358.
- [14] M. Janowski, P. Walczak, M.S. Pearl, Predicting and optimizing the territory of blood–brain barrier opening by superselective intra-arterial cerebral infusion under dynamic susceptibility contrast MRI guidance, *J. Cereb. Blood Flow Metab.* 36 (2016) 569–575.
- [15] W.G. Lesniak, C. Chu, A. Jablonska, Y. Du, M.G. Pomper, P. Walczak, M. Janowski, A distinct advantage to intra-arterial delivery of ^{89}Zr -bevacizumab in PET imaging of mice with and without osmotic opening of the blood–brain barrier, *J. Nucl. Med.* 60 (5) (2018) 617–622.
- [16] M. Zawadzki, J. Walecki, B. Kostkiewicz, K. Kostyra, M.S. Pearl, M. Solaiyappan, P. Walczak, M. Janowski, Real-time MRI guidance for intra-arterial drug delivery in a patient with a brain tumor: technical note, *BMJ Case Rep.* 12 (2019).
- [17] K. Svoboda, R. Yasuda, Principles of two-photon excitation microscopy and its applications to neuroscience, *Neuron* 50 (2006) 823–839.
- [18] Y. Liang, K. Li, K. Riecken, A. Maslyukov, D. Gomez-Nicola, Y. Kovalchuk, B. Fehse, O. Garaschuk, Long-term in vivo single-cell tracking reveals the switch of migration patterns in adult-born juxtaglomerular cells of the mouse olfactory bulb, *Cell Res.* 26 (2016) 805–821.
- [19] C. Chu, G. Liu, M. Janowski, J.W.M. Bulte, S. Li, M. Pearl, P. Walczak, Real-time MRI guidance for reproducible hyperosmolar opening of the blood–brain barrier in mice, *Front. Neurol.* 9 (2018) 921.
- [20] G. Makowicz, R. Poniatowska, M. Lusawa, Variants of cerebral arteries - anterior circulation, *Pol. J. Radiol.* 78 (2013) 42–47.
- [21] D.S. Liebeskind, Collateral circulation, *Stroke* 34 (2003) 2279–2284.
- [22] A. Holtmaat, T. Bonhoeffer, D.K. Chow, J. Chuckowree, V. De Paola, S.B. Hofer, M. Hubener, T. Keck, G. Knott, W.C. Lee, R. Mostany, T.D. Mrsic-Flogel, E. Nedivi, C. Portera-Cailliau, K. Svoboda, J.T. Trachtenberg, L. Wilbrecht, Long-term, high-resolution imaging in the mouse neocortex through a chronic cranial window, *Nat. Protoc.* 4 (2009) 1128–1144.
- [23] M.J. Vosjan, L.R. Perk, G.W. Visser, M. Budde, P. Jurek, G.E. Kiefer, G.A. van Dongen, Conjugation and radiolabeling of monoclonal antibodies with zirconium-89 for PET imaging using the bifunctional chelate p-isothiocyanatobenzyl-desferrioxamine, *Nat. Protoc.* 5 (2010) 739–743.
- [24] R. Guzman, M. Janowski, P. Walczak, Intra-arterial delivery of cell therapies for stroke, *Stroke* 49 (2018) 1075–1082.
- [25] M. Kaya, S. Gulturk, I. Elmas, R. Kalayci, N. Arican, Z.C. Kocylidiz, M. Kucuk, H. Yorulmaz, A. Sivas, The effects of magnesium sulfate on blood–brain barrier disruption caused by intracarotid injection of hyperosmolar mannitol in rats, *Life Sci.* 76 (2004) 201–212.
- [26] E.K. Weidman, C.P. Foley, O. Kallas, J.P. Dyke, A. Gupta, A.E. Giambrone, J. Ivanidze, H. Baradaran, D.J. Ballon, P.C. Sanelli, Evaluating permeability surface-area product as a measure of blood–brain barrier permeability in a murine model, *AJNR Am. J. Neuroradiol.* 37 (2016) 1267–1274.
- [27] M. Janowski, A. Lyczek, C. Engels, J. Xu, B. Lukomska, J.W. Bulte, P. Walczak, Cell size and velocity of injection are major determinants of the safety of intracarotid stem cell transplantation, *J. Cereb. Blood Flow Metab.* 33 (2013) 921–927.
- [28] L.L. Cui, E. Kerkela, A. Bakreen, F. Nitzsche, A. Andrzejewska, A. Nowakowski, M. Janowski, P. Walczak, J. Boltze, B. Lukomska, J. Jolkkonen, The cerebral embolism evoked by intra-arterial delivery of allogeneic bone marrow mesenchymal stem cells in rats is related to cell dose and infusion velocity, *Stem Cell Res Ther* 6 (2015) 11.
- [29] L.A. Gillilan, Potential collateral circulation to the human cerebral cortex, *Neurology* 24 (1974) 941–948.
- [30] E. Cuccione, G. Padovano, A. Versace, C. Ferrarese, S. Beretta, Cerebral collateral circulation in experimental ischemic stroke, *Exp. Transl. Stroke. Med.* 8 (2016) 2.
- [31] T. Nhan, A. Burgess, E.E. Cho, B. Stefanovic, L. Lilge, K. Hynynen, Drug delivery to the brain by focused ultrasound induced blood–brain barrier disruption: quantitative evaluation of enhanced permeability of cerebral vasculature using two-photon microscopy, *J. Control. Release* 172 (2013) 274–280.
- [32] A. Burgess, S. Dubey, S. Yeung, O. Hough, N. Eterman, I. Aubert, K. Hynynen, Alzheimer disease in a mouse model: MR imaging-guided focused ultrasound targeted to the hippocampus opens the blood–brain barrier and improves pathologic abnormalities and behavior, *Radiology* 273 (2014) 736–745.
- [33] K.T. Chen, K.C. Wei, H.L. Liu, Theranostic strategy of focused ultrasound induced blood–brain barrier opening for CNS disease treatment, *Front. Pharmacol.* 10 (2019) 86.
- [34] A.B. Etame, R.J. Diaz, C.A. Smith, T.G. Mainprize, K. Hynynen, J.T. Rutka, Focused ultrasound disruption of the blood–brain barrier: a new frontier for therapeutic delivery in molecular neurooncology, *Neurosurg. Focus.* 32 (2012) E3.
- [35] S. Wang, I.S. Shin, H. Hancock, B.S. Jang, H.S. Kim, S.M. Lee, V. Zderic, V. Frenkel, I. Pastan, C.H. Paik, M.R. Dreher, Pulsed high intensity focused ultrasound increases penetration and therapeutic efficacy of monoclonal antibodies in murine xenograft tumors, *J. Control. Release* 162 (2012) 218–224.
- [36] Z.I. Kovacs, S. Kim, N. Jikaria, F. Qureshi, B. Milo, B.K. Lewis, M. Bresler, S.R. Burks, J.A. Frank, Disrupting the blood–brain barrier by focused ultrasound induces sterile inflammation, *Proc. Natl. Acad. Sci. U. S. A.* 114 (2017) E75–E84.
- [37] E.A. Neuwelt, J. Minna, E. Frenkel, P.A. Barnett, C.I. McCormick, Osmotic blood–brain barrier opening to IgM monoclonal antibody in the rat, *Am. J. Phys.* 250 (1986) R875–R883.
- [38] B. Wang, T. Siahaan, R. Soltero, *Drug Delivery: Principles And Applications*, Wiley Ser Drug Disc, 2005, pp. 1–448.
- [39] R. Razpotnik, N. Novak, V. Curin Serbec, U. Rajcevic, Targeting malignant brain tumors with antibodies, *Front. Immunol.* 8 (2017) 1181.
- [40] R.T. Frank, K.S. Aboody, J. Najbauer, Strategies for enhancing antibody delivery to the brain, *Biochim. Biophys. Acta* 1816 (2011) 191–198.
- [41] H.L. Liu, P.H. Hsu, C.Y. Lin, C.W. Huang, W.Y. Chai, P.C. Chu, C.Y. Huang, P.Y. Chen, L.Y. Yang, J.S. Kuo, K.C. Wei, Focused ultrasound enhances central nervous system delivery of bevacizumab for malignant glioma treatment, *Radiology* 281 (2016) 99–108.
- [42] J.G. DeStefano, J.J. Jamieson, R.M. Linville, P.C. Searson, Benchmarking in vitro tissue-engineered blood–brain barrier models, *Fluids Barriers CNS* 15 (2018) 32.
- [43] R.M. Linville, J.G. DeStefano, M.B. Sklar, Z. Xu, A.M. Farrell, M.I. Bogorad, C. Chu, P. Walczak, L. Cheng, V. Mahairaki, K.A. Whartenby, P.A. Calabresi, P.C. Searson, Human iPSC-derived blood–brain barrier microvessels: validation of barrier function and endothelial cell behavior, *Biomaterials* 190–191 (2019) 24–37.
- [44] U. Tosi, H. Kommidi, V. Bellat, C.S. Marnell, H. Guo, O. Adeyuan, M.E. Schweitzer, N. Chen, T. Su, G. Zhang, U.B. Maachani, D.J. Pisapia, B. Law, M.M. Souweidane, R. Ting, Real-time, in vivo correlation of molecular structure with drug distribution in the brain striatum following convection enhanced delivery, *ACS Chem. Neurosci.* 10 (2019) 2287–2298.
- [45] W.G. Mayhan, D.D. Heistad, Permeability of blood–brain barrier to various sized molecules, *Am. J. Phys.* 248 (1985) H712–H718.
- [46] B.C. Pestalozzi, S. Brignoli, Trastuzumab in CSF, *J. Clin. Oncol.* 18 (2000) 2349–2351.
- [47] T.W. Ruhstaller, U. Amsler, T. Cerny, Rituximab: active treatment of central nervous system involvement by non-Hodgkin's lymphoma? *Ann. Oncol.* 11 (2000) 374–375.
- [48] M.H. Jansen, T. Lagerweij, A.C. Sewing, D.J. Vugts, D.G. van Vuurden, C.F. Molthoff, V. Caretti, S.J. Veringa, N. Petersen, A.M. Carcaboso, D.P. Noske, W.P. Vandertop, P. Wesseling, G.A. van Dongen, G.J. Kaspers, E. Hulleman, Bevacizumab targeting diffuse intrinsic pontine glioma: results of ^{89}Zr -bevacizumab PET imaging in brain tumor models, *Mol. Cancer Ther.* 15 (2016) 2166–2174.
- [49] K.R. Pechman, D.L. Donohoe, D.P. Bedekar, S.N. Kurpad, R.G. Hoffmann, K.M. Schmainda, Characterization of bevacizumab dose response relationship in U87 brain tumors using magnetic resonance imaging measures of enhancing tumor volume and relative cerebral blood volume, *J. Neuro-Oncol.* 105 (2011) 233–239.

2. Introduction

2.1. The blood-brain barrier (BBB)

The blood-brain barrier (BBB) is a unique functional structure in the central nervous system (CNS). It is mainly composed of a monolayer of highly specialized brain endothelial cells closely sealed by tight junctions and surrounded by the pericytes, astrocytic end-feet¹ (**Fig. 1a**). The BBB serves as a regulator for substances influx and efflux to maintain a homeostatic brain function. As a highly selective permeability barrier, the BBB is known to prevent the entry of harmful substances from the peripheral circulation into the CNS, making it as an important defense for CNS protection. However, the BBB is also a major obstacle for effective delivery of therapeutics into CNS. In the presence of an intact BBB, molecules, and compounds sized above 180 Da do not typically enter the CNS². Therefore, chemotherapeutics and therapeutic biologics such as trophic factors do not cross the BBB as their molecular weights usually are between 200 and 1200 Da³. The poor penetration prevents more than 98% of the existing pharmaceutical agents from entering the brain tissue after intravascular delivery (**Fig. 1b**), resulting in limited treatment efficacy of CNS diseases⁴⁻⁵.

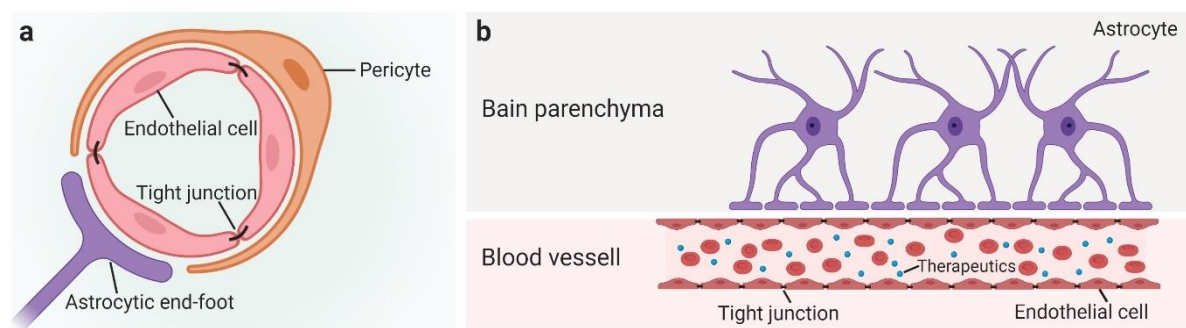


Figure 1. The blood-brain barrier (BBB). **a**, The structure of the BBB and its major components. **b**, The intact BBB prevents the passage of therapeutics from the circulating blood into the brain parenchyma.

2.2. Hyperosmotic mannitol-induced BBB opening (BBBO)

To overcome the limited accessibility of therapeutics to the CNS, various methods and drugs have been developed to induce transient permeabilization of the BBB and intra-arterial (IA) mannitol-mediated osmotic opening most frequently has been used in both preclinical and clinical studies⁶⁻⁸. Brightman *et al.*⁹ pioneered this approach demonstrating in the 1970s IA injection of the hyperosmotic mannitol-induced opening of endothelial tight junctions for the passage of agents into the brain (**Fig. 2**). In the

following decades, IA mannitol has been the primary method used to open BBB, followed by the infusion of therapeutic agents including chemotherapeutics, vectors, and stem cells in preclinical models and clinical studies^{7-8, 10-11}. However, the current strategy of osmotic BBB opening (BBBO) is highly variable and inconsistent¹² due to multiple factors including mannitol dose, injection speed but also vascular anatomy and cerebral hemodynamics of individual patients or experimental animals¹³. As a result, the published protocols show high variability (**Table 1**). For instance, in different rodent studies, the infusion rate of mannitol into the carotid artery using rats ranged from 2.6 ml/min¹⁴ to as high as 7.2 ml/min¹⁵. Notwithstanding the wide variance of these parameters, this spectrum greatly exceeds the physiological perfusion rate in the internal carotid artery risking damage. Additionally, several studies awkwardly reported intravenous (instead of intraarterial) injection of mannitol to break the BBB to facilitate the brain accumulation of therapeutics including stem cells¹⁶⁻¹⁸. Recently, in a rabbit model, interventional MRI-guidance was also used to predict and optimize the territory of BBBO through direct fine-tuning of the infusion speed, dose and the position of the IA catheter¹³. The study also gives a hint that real-time MRI is an attractive and promising approach to address the high variability of BBBO in small animals.

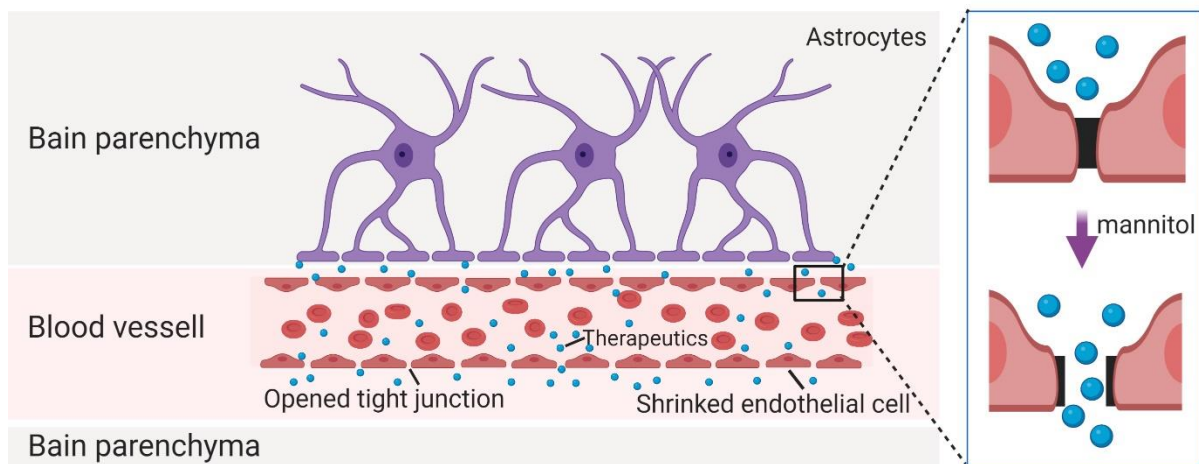


Figure 2. Hyperosmotic mannitol-induced BBB opening affords the access of therapeutics to the brain parenchyma.

Table 1 Hyperosmotic mannitol-induced BBBO in small animals

Animal species (weight or age)	Injection route	Injection rate	Injection duration or dose	Reference
Rat (200-240 g)	Intra-arterial	7.2 ml/min	30 s	19-22
Rat (350-450 g)	Intra-arterial	7.2 ml/min	5 ml/kg	23
Rat (170-340 g)	Intra-arterial	15 ml/kg/min	30 s	14, 24
Rat (~325 g)	Intra-arterial	5.4 ml/min	25 s	25-26
Rat (300-350 g)	Intra-arterial	4.98 ml/min	30 s	27
Rat (250-300 g)	Intravenous	N.D.	10 min	16
Mouse (22-24 g)	Intra-arterial	1 ml/min	0.75 ml	10
Mouse (8-12 week)	Intravenous	N.D	< 2 min	18
Mouse (N.D)	Intravenous	N.D	5 ml/kg	28

N.D. not determined

2.3. Intra-arterial delivery of therapeutics to the central nervous system (CNS)

There are various routes to deliver therapeutics to the CNS including oral or intranasal administration, intravenous, intraarterial and intracerebral injection²⁹⁻³². The advantages and limitations of each approach are described in **Table 2**. Among them, IA delivery seems superior to other methods for CNS as it circumvents many drawbacks. Although IA route has some risks such as microembolization or triggering an immune response³³, overall this minimally invasive technique is mature, well-established and safe³⁴⁻³⁵. Most importantly, it facilitates high drug concentrations in the brain while minimizing systemic toxicity³⁶⁻³⁷. It is worth noting that IA approach combined with the image guidance could visualize and predict the delivery of therapeutics to the brain. For example, studies have demonstrated the capability of real-time MRI to visualize intra-arterially administrated stem cells within cerebral vasculature at a high temporal resolution³⁸⁻³⁹. Such real-time imaging modality can also predict the biodistribution of injected therapeutics using pre-infusion of a contrast agent *via* IA catheter thereby determining whether they are delivered to the expected brain region or misrouted³⁹⁻⁴⁰. While MRI is excellent for high spatial resolution anatomical imaging and perfusion studies, its sensitivity is rather low and insufficient for monitoring drug pharmacokinetics. Positron Emission Tomography (PET) imaging bridges that gap, and that modality was instrumental for demonstrating biodistribution of therapeutics after IA route.

Table 2. Common delivery routes of therapeutics to the CNS.

Delivery route	Advantage	Limitation
Oral	self-administration convenient non-invasive safe	hepatic first pass effect limited brain exposure risk of systemic toxicity low bioavailability difficult to overcome the BBB
Intranasal	self-administration relatively large absorption area non-invasive bypasses the BBB safe	short retention time low permeability for hydrophilic drug lack of potent drugs
Intravenous	common convenient safe	peripheral organs first pass effect risk of immune response limited brain exposure risk of systemic toxicity difficult to overcome the BBB
Intracerebral	spatially precise deposition high local drug concentration low systemic toxicity	invasive risk of focal hemorrhage, headache, somnolence, subdural hematoma, requires highly trained surgeons dose restriction less acceptable to patients
Intra-arterial	high local drug concentration immediate onset of action minimally invasive targeted delivery low systemic toxicity safe techniques in the clinic	risk of microembolism risk of immune response requires trained neurointerventionalist

Advances in biotechnology enable efficient and cost-effective design of macromolecules. Such scaffolds can be designed with high affinity and specificity for safe engagement of certain molecular targets. Recently, there is growing interest in nanobodies as therapeutic agents and dendrimers as drug nanocarriers. Nanobodies are derived from naturally occurring heavy chain antibodies in camelids. They are one-tenth (~15 kDa) of the size of monoclonal antibodies. The small size of nanobodies

has several advantages such as easy in-vitro production, reduced immunogenicity, high affinity to molecular targets, and improved permeability across biological barriers⁴¹⁻⁴². Polyamidoamine (PAMAM) dendrimers are quickly emerging as a versatile nanoplatform for selective drug delivery due to their unique physicochemical properties, including small size, large number of reactive terminal groups that can be readily modified with different functionalities, bulky interior void volume, and biocompatibility⁴³. A generation-4 PAMAM dendrimer has a similar size to a nanobody and has the further advantage of capacity for conjugation with various functionalities, including ligands for molecular targets, imaging radio-, chemo-, and immunotherapeutic agents⁴⁴. Thus, the nanobody and PAMAM were used as part of this dissertation to explore their penetration and clearance from the brain using PET.

2.4. Intravital imaging on studying mechanisms of BBBO and drug penetration

MRI is able to guide delivery and visualize drug distribution in the brain; however, the low spatial resolution and sensitivity are not sufficient for studying pharmacokinetics *in vivo*. To date, comprehensive and mechanistic investigations on drug extravasation across osmotically opened BBBO at the microscopic level are lacking. Two-photon microscopy (2PM) is an emerging intravital imaging technique that allows for imaging tissues up to about one millimeter in depth⁴⁵. Using 2PM, it is achievable to reach sufficient temporal and spatial resolution in the cerebral cortex to track agents' penetration across the BBB at the level of microvasculature. Due to limited depth of penetration, 2PM studies are restricted to superficial structures such as cerebral cortex accessed with an implanted cranial window⁴⁶.

2.5. Goals of the project

The overall goal of this project was to use intra-arterial route with manipulation of the BBB permeability for effective delivery of therapeutics to the brain and explore the mechanisms facilitating drug accumulation in the brain. The specific goals were as follows:

- i) to develop a predictable, reproducible and safe hyperosmotic mannitol-based BBBO technique in mice.
- ii) to exploit the established experimental platform with IA delivery of two major classes of therapeutics to the brain and determine their pharmacokinetics.
- iii) to optimize the hyperosmotic mannitol-based BBBO in the cortex of mouse.
- iv) to investigate the osmotic BBBO as well as subsequent drug accumulation in the brain at the microscopic level using intravital microscopy.

3. Materials and Methods

3.1. Hyperosmotic mannitol-based BBBO

3.1.1. *Animals and endovascular catheterization*

All procedures were performed in accordance with guidelines for the care and use of laboratory animals and were approved by the Johns Hopkins Animal Care and Use Committee. Male SCID mice (n = 8, 6-8 weeks old, 20-25 g, Jackson Laboratory) were used. Anesthesia was induced with 5% isoflurane and maintained with 1.5-2% isoflurane during surgery. The common carotid artery (CCA) bifurcation was exposed using blunt dissection. The occipital artery branching off from the external carotid artery (ECA) was coagulated. The ECA and the pterygopalatine artery (PPA) were temporarily ligated with 4-0 silk sutures to route the entire flow into cerebral arteries. A temporary tie was placed on the carotid bifurcation and the proximal CCA was permanently ligated using 4-0 sutures. Then a microcatheter (PE-8-100, SAI Infusion Technologies) was flushed with 2% heparin (1000 units/ml, heparin sodium, Upjohn), via a small arteriotomy and advanced into the internal carotid artery (ICA). The catheter was secured by two purse-string suture ties around CCA. For goal iii-iv, before making a small arteriotomy, a suture connecting a weight (25 g) was secured around the contralateral CCA.

3.1.2. *Interventional MRI*

The mice with a secured intra-arterial catheter were positioned in a Bruker 11.7T MRI scanner. Baseline T2 (TR/TE = 2,500/30ms) and T1 (TR/TE 350/6.7ms)-weighted and dynamic Gradient echo-echo planar imaging (GE-EPI, TR/TE 1250/9.7ms, field of view (FOV) = 14, matrix = 128, acquisition time = 60 s and 24 repetitions) images of the brain were acquired. A superparamagnetic iron oxide (SPIO) nanoparticle formulation (Feraheme, dissolved in saline at 1:30; 0.3mg Fe/ml) or gadolinium (Gadoteridol, dissolved in saline at 1:50; 5.46 mg/mL) was infused intra-arterially at rates between 0.05 and 0.20 ml/min under dynamic GE-EPI MRI to predict perfusion territory and optimize that territory to the desired size and location. An infusion pump (PHD 2000, Harvard Apparatus Inc.) was used to control the contrast administration. The routine was to start injections from the lowest speed, and then increase it at increments of 0.05 ml/min until an effective perfusion area was achieved. Then, 25% mannitol was delivered via an IA route over 1 min at a speed determined by previous contrast agent injection. T1-weighted images were obtained post-gadolinium to visualize BBB integrity.

To achieve BBBO in cortex, for animals where the cortex was not perfused (most cases), the weight around contralateral CCA was engaged, occluding the vessel with dynamic imaging of IA infusion to confirm cortical perfusion/supply. Once cortical perfusion has been confirmed, 25% mannitol was infused until BBB breach has been achieved (up to three bolus injections 1-2 min each; interval between infusions is 30 s). T1-weighted images were obtained post-gadolinium to visualize BBB integrity.

3.1.3. Histological validation of BBBO

For histological evaluation of BBBO, 0.1 ml of 2% w/v Evans blue (EB) or rhodamine red (1 mmol/l) were subsequently administrated intra-arterially at the same rate as mannitol. The brains were harvested right after injection and without perfusion to avoid the clearance of both imaging agents. For EB verification, frozen coronal brain slabs (1-mm) were sliced on a cryostat. For the detection of rhodamine, the brain was cryosectioned at 30 μ m and fluorescent images of rhodamine biodistribution were acquired.

3.1.4. MRI and immunohistochemistry in evaluating the safety of BBBO

Three and seven days after BBBO, the safety of the procedure was evaluated by MRI. For further histological assessment, animals were transcardially perfused with 5% sucrose and then with 4% paraformaldehyde (PFA). The brains were cryopreserved in 30% sucrose and cryosectioned at 30- μ m. Primary antibodies and dilutions were used as follows: anti-GFAP (1:250, Dako); anti-IBA1 (1:250, Wako); and anti-NeuN (1:100, Cell Signaling Technology). The secondary antibody was goat anti-rabbit (Alexa Fluor-488, 1:200, Molecular Probes). All the fluorescent images were acquired using an inverted microscope (Zeiss, Axio Observer Z1).

3.2. Brain uptake of nanobody and dendrimer

3.2.1. Gelsolin nanobody

Gelsolin nanobody 11 (NB11), cloned in the pHEN6c vector, was purified from WK6 cells. Briefly, competent WK6 cells were transformed with the plasmid and grown at 37 °C in TB medium with 100 μ g/ml ampicillin until the OD600 reached 0.60–0.80. Then temperature was set to 20 °C and nanobody expression was induced by the addition of 0.5 mM IPTG. After overnight induction, bacterial cultures were pelleted by centrifugation at 11,000 \times g for 20 min at 4 °C. Cells were resuspended in a small volume of phosphate-buffered saline (PBS), and 0.2 mg/ml lysozyme was added. Lysis proceeded during 30 min rotation at room temperature. This suspension was then

sonicated (Vibracell, Sonics and Materials, Newtown, CT, USA) and centrifuged again ($\sim 29,000\times g$) for 30 min at 4 °C to obtain the bacterial protein lysate. The His6-tagged nanobody was purified by Immobilized metal ion affinity chromatography (IMAC) on a Ni^{2+} column and eluted with 500 mM imidazole. Finally, nanobody 11 was purified to homogeneity by gel filtration chromatography on a Superdex 200 HR 10/30 column (GE Healthcare, Diegem, Belgium), equilibrated in 20 mM Tris.HCl pH 7.5, 150 mM NaCl, 1 mM DTT.

3.2.2. Synthesis of NB and deferoxamine

For conjugation of deferoxamine (DFO) with NB, storage buffer was replaced with saline using ultrafiltration with Millipore Amicon Ultra Centrifugal Filters 3000 Da molecular weight cut-off (MWCO, Millipore Sigma, cat #: UFC80030) and pH was adjusted to 9 with a small amount of 2 M Na_2CO_3 solution. Then five-fold molar equivalent of SCN-Bn-DFO dissolved in DMSO was added and conjugation was carried out for 30 min at 37 °C in a thermomixer at 550 r.p.m. Resulting NB-DFO conjugate was purified as described above, reconstituted in saline at 10 mg/ml and 0.1 ml aliquots were kept at -20 °C until further use.

3.2.3. Synthesis of PAMAM dendrimers and DFO

$\text{G4}(\text{NH}_2)_{64}$ dendrimer (0.030 g, 2.11×10^{-6} mol) was dissolved in 3 ml deionized water resulting in pH = 9.2 and 5 mol equivalent of SCN-Bn-DFO (0.008 g, 1.05×10^{-5} mol) reconstituted in 0.2 ml of DMSO was added. The reaction proceeded for 30 min at 37 °C in a thermomixer at 550 r.p.m., and a small amount of reaction mixture was subjected to MALDI-TOF mass spectrometry to confirm conjugation of DFO with dendrimer. Next, 0.2 ml (2.99×10^{-3} mol) of glycidol was added and reaction was carried for additional overnight to cap remaining primary amines with butane-1,2-diol (Bdiol). Resulting $\text{G4}(\text{DFO})_3(\text{Bdiol})_{110}$ dendrimer was purified using deionized water and ultrafiltration with Millipore Amicon Ultra Centrifugal Filters 10,000 Da MWCO, lyophilized, yielding 0.035 g of the conjugate, which was stored at -20 °C until further use.

3.2.4. Matrix-assisted laser desorption ionization-time-of-flight (MALDI-TOF)

To determine average number of DFO molecules conjugated with nanobody and dendrimer and assess its capping efficiency with butane-1,2-dio, MALDI-TOF spectra were recorded on a Voyager DE-STR spectrophotometer, using 2,5-dihydroxybenzoic acid (DHB) as a matrix, which was dissolved in 50% MeOH and 0.1% TFA aqueous

solution at concentration of 20 mg/ml. NB and NB(DFO)₂ samples were desalted using Zeba™ spin columns 7 K MWCO (cat. # 89882, Thermo Fisher Scientific). Samples of G4(NH₂)₆₄, G4(NH₂)₆₁(DFO)₃, and G4(DFO)₃(Bdiol)₁₁₀ dendrimers were prepared in deionized water. 10 µl of samples were mixed with 10 µl of matrix, and 1 µl of resulting mixture was placed on the target plate (in triplicate) and evaporated. Number of shots and laser power was adjusted according to spectrum quality.

3.2.5. Radiolabeling of NB and dendrimer

Radiolabeling of NB(DFO)₂ and G4(DFO)₃(Bdiol)₁₁₀ with Zirconium-89 (⁸⁹Zr) was performed using reported procedure⁴⁷. ⁸⁹ZrNB(DFO)₂ was fabricated with ~99% radiochemical purity and 129.5 ± 10 MBq/mg specific activity. ⁸⁹ZrG4(DFO)₃(Bdiol)₁₁₀ was prepared with ~99% radiochemical purity and 120 ± 8 MBq/mg specific activity. For further studies, ⁸⁹ZrNB(DFO)₂ and ⁸⁹ZrG4(DFO)₃(Bdiol)₁₁₀ were diluted with sterile saline.

3.2.6. PET-CT imaging of IA and IV delivery of radiolabelled NB and dendrimer

6–8-week-old male C3HeB/FeJ mice (Jackson, n = 4 per group, total n = 28) were used in PET-CT studies. Under general anesthesia, a catheter was placed in the ICA, as we have reported above, and mice were transferred to the PET-CT scanner. BBB opening was performed with 25% mannitol infused for 1 min at a speed of 0.15 ml/min. ~8.5 MBq (~230 µCi) of ⁸⁹ZrNB(DFO)₂ or ⁸⁹ZrG4 (DFO)₃ (Bdiol)₁₁₀ reconstituted in 1 ml of saline was infused IA or IV over 5 min at 0.15 ml/min flow rate. There were four experimental groups: 1) IA infusion with BBB intact (IA/BBBI), 2) BBBO followed by IA infusion (BBBO/IA), 3) BBBO followed by intravenous infusion (BBBO/IV) and 4) intravenous infusion followed by BBBO (IV/BBBO) for ⁸⁹ZrNB(DFO)₂. Three groups-1) IA infusion with BBB intact (IA/BBBI), 2) BBBO followed by IA infusion (BBBO/IA), and 3) intravenous infusion followed by BBBO (IV/BBBO)—were evaluated for ⁸⁹ZrG4(DFO)₃(Bdiol)₁₁₀. Accumulation of ⁸⁹ZrNB(DFO)₂ or ⁸⁹ZrG4(DFO)₃(Bdiol)₁₁₀ in the brain was initially evaluated with dynamic 30-min-long PET scans divided into 30 s frames, followed by whole body PET/CT imaging acquired around 1 h and 24 h post-infusion (pi), in two bed positions and 7 min per bed on an ARGUS small animal PET/CT scanner (Sedecal, Madrid, Spain). A CT scan (512 projections) was performed before whole-body PET imaging at 1 h (mice remained in the scanner after dynamic scan was completed) and 24 h pi, to enable co-registration. PET data were reconstructed using the two-dimensional ordered subsets-expectation maximization

algorithm (2D-OSEM) and corrected for dead time and radioactive decay. Presented whole-body images were generated using Amira® (FEI, Hillsboro, OR, USA) and dynamic scans (brain and heart radioactivity accumulation) and radioactivity distribution in different brain regions were analyzed with PMOD 4.3 (PMOD Technologies LLC, Zürich, Switzerland). The peak concentration of radioactivity over 5 min around the end of IA infusion of $^{89}\text{ZrNB}(\text{DFO})_2$ and $^{89}\text{ZrG4}(\text{DFO})_3(\text{Bdiol})_{110}$ was extracted, and compared with the last 5 min of the dynamic scans to calculate the rate of early clearance of administrated radiotracers from the brain. Then the radioactivity detected in the CNS at 1 h and 24 h after infusion was used to assess their later brain clearance. The effect of BBBO on nanobody or dendrimer brain accumulation following their IV infusion was evaluated by comparing level of radioactivity 5 min before and 5 min after mannitol administration.

3.2.7. Ex-vivo biodistribution of NB and dendrimer

Upon completion of PET-CT at 24 h pi of $^{89}\text{ZrNB}(\text{DFO})_2$ or $^{89}\text{ZrG4}(\text{DFO})_3(\text{Bdiol})_{110}$, mice were sacrificed; blood, brain (divided into right and left hemispheres), and selected organs were harvested and weighed. The radioactivity in collected samples was measured on a PerkinElmer 2480 Automatic Gamma Counter (Waltham, MA, USA) 4 days after sample collection to avoid detector saturation due to high radioactivity accumulation in brain and kidneys. To calculate the percent of injected dose per gram of tissue (%ID/g), triplicate radioactive standards (0.01% of the injected dose) were counted along with tissue samples.

3.3. Intravital imaging on drug delivery in mouse cortex

3.3.1. Cranial window implantation

Cranial window procedures were performed as previously described⁴⁸. Briefly, mice were shaved and deeply anesthetized with 1.5-2% isoflurane and stabilized on a stereotactic frame. Before surgery, animals were administered with dexamethasone sodium phosphate (0.02 ml at 4 mg/ml, Fresenius Kabi) by subcutaneous injection to prevent cerebral edema. Then the skin and periosteum were removed to expose the skull. A craniotomy (~ 3 mm diameter) was conducted over the right parietal bone ~1.5 mm posterior to bregma and ~1.5 mm lateral from midline. Saline was applied regularly to avoid heating caused by drilling during skull-thinning procedure. At the end, the central island of skull bone was gently lifted, removed, and covered with a circular coverglass (3 mm diameter, #1 thickness, Harvard Biosciences) sealed to the skull using glue. For the subsequent imaging sessions, a custom-made head-bar with a

circular opening was sealed to the skull with dental cement, covering all the exposed skull, wound margins and glass edges. Mice were allowed to recover for 7 days before imaging.

3.3.2. Conjugation of bevacizumab and fluorescein

Bevacizumab was washed 3 times using ultrafiltration with Millipore Amicon Ultra Centrifugal Filters 50 kDa MWCO (Millipore). After washing, the antibody was resuspended in saline at the concentration of 10 mg/ml and pH was adjusted to 9.0 with 0.1 M Na₂CO₃. NHS-Fluorescein (Thermo Fisher Scientific) was then dissolved in DMSO at the concentration of 10 mg/ml was mixed with antibody at the 1:10 M ratio. Conjugation was carried for 1 h in 37 °C with 160 r.p.m agitation. The bevacizumab and fluorescein (bevacizumab-FITC) complexes were washed 3 times with saline on the 50 kDa centrifugal filters. Final protein concentration of bevacizumab-FITC and conjugation efficiency were determined by absorbance at 280 nm and 495 nm measured using a NanoDrop (Thermo Fisher Scientific). The MALDI-TOF was performed as described for NB and dendrimers.

3.3.3. Intravital Epi-fluorescence and Two-photon microscopy

Before microscopy, isoflurane anesthetized mice (n = 5) with cranial window and with arterial access as described above were stabilized in a custom-made frame immobilizing their head. The mice were positioned under an epi-fluorescent microscope and a 10× magnification objective was used for capturing images at frequency of 1-2 Hz. Saline solution of 0.001 mM rhodamine (0.58 kDa) was injected using a syringe infusion pump at the rate of 0.15 ml/min over 1 min via the ICA microcatheter to visualize trans-catheter perfusion. When the cortex was not perfused, the contralateral CCA was closed temporarily for 20 s by engaging the weights.

For Two-photon microscopy (2 PM) to visualize BBBO and drug penetration, mice were placed under a multiphoton microscope (FV1000MPE, Olympus, Tokyo, Japan). A 10× objective (UPlanSApo, 0.40 NA and 3.1 mm working distance) was centered over the cranial window and used to collect time series images of 800 × 800 pixels (1.59 μm/pixel; 2 μs/pixel; 100 frames) at an estimated depth of 150 μm below the cortical surface. Rhodamine (0.002 mM) mixed with bevacizumab-FITC (0.01 mM) was injected prior to BBBO to collect baseline data and optimize cortical perfusion (temporary contralateral CCA closure). Then, 25% mannitol mixed with rhodamine and bevacizumab-FITC was delivered at the rate of 0.15 ml/min for 4 mins in total. A

common excitation wavelength of 800 nm was used to simultaneously image both dyes during injection and dynamic imaging was continuously performed for 14 mins.

3.3.4. Histology and immunohistochemistry

For histological evaluation on the safety of BBBO in the cortex, 7 days after surgery, animals (n = 4) were anesthetized and perfused transcardially with 5% sucrose, followed by 4% PFA. The brains were rapidly removed and post-fixed overnight in 4% PFA at 4 °C. The brains were cryopreserved in 30% sucrose and 30- μ m thick coronal sections were cryosectioned. immunohistochemistry for anti-GFAP (1:250, Dako) and anti-IBA1 (1:250, Wako) was performed to assess the neuroinflammation. The secondary antibody was goat antirabbit (Alexa Fluor-488, 1:200, Molecular Probes). For detecting the biodistribution of infused bevacizumab, the mice with BBBO (n = 4) and without BBBO (n = 3) were sacrificed 1 h after administration. The brains were cryosectioned at 30 μ m and the slices were stained with goat anti-human secondary antibody (Alexa Fluor-488, 1:200, Invitrogen). All the fluorescent images were acquired using an inverted microscope (Zeiss, Axio Observer Z1).

3.4. Data processing and statistical analysis

Data is expressed as mean \pm SD unless otherwise specified. Quantitation of immunohistochemistry was based on relative fluorescence using Image J and analyzed using a Mann-Whitney *U*-test (in goal i) or a student's paired t-test (in goal iii-iv). The ratio of ipsi-/contralateral fluorescence intensity was analyzed using a student's unpaired t-test (in goal iii-iv). The MRI analysis of the change in area of the contrast perfusion territory and Gd-enhancement for each mouse was calculated using a custom-written script in MATLAB and analyzed using a Mann-Whitney *U*-test (in goal i) or a paired t-test (in goal iii-iv). For the statistical analysis in goal ii, PROC MIXED (SAS 9.4) was used with the lowest means square (LMS) test for comparison between groups. The statements repeated and random were used for repeated measures and to express random effects, respectively.

4. Results

4.1. MRI guidance enabled a reproducible hyperosmolar BBBO in mice

4.1.1. Real-time MRI for prediction of trans-catheter perfusion territory using MR contrast

The infusion of MR contrast (SPIO or Gd) results in a drop of T2* hypointensity on MRI, which immediately clears once the infusion is stopped. This T2* hypointensity in the brain can be sampled by GE-EPI at a temporal resolution of 2 images each second, which allows precise temporo-spatial visualization of the parenchymal perfusion territory. Initially, our transcatheter SPIO contrast delivery was set at 0.05 ml/min, and in those animals in which no drop of T2* intensity was observed, we increased the speed at increments 0.05 ml/min, until the contrast agent appeared on real-time MRI. There was no need to increase the speed over 0.15 ml/min, which resulted in satisfactory and reproducible brain perfusion, as visualized by a characteristic reduction in signal intensity for the duration of the injection bolus (**Fig. 3 a,b**). Notably, increasing the infusion speed to 0.2 ml/min resulted in delayed brain injury, as reflected by an abnormal signal on T2-weighted images and pathological changes on histology (data not shown). In addition, the injection rate for a satisfactory perfusion territory may vary among mice, necessitating the titration of the injection speed for each animal.

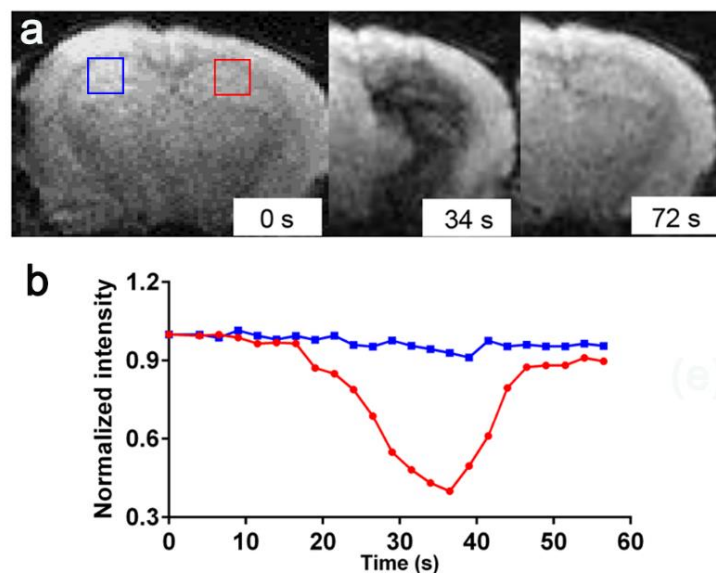


Figure 3. Use of real-time MRI to ensure an infusion speed via IA injection to predict perfusion territory in a mouse brain. a, Injecting an MRI contrast at 0.15 ml/min results in efficient cerebral perfusion, as marked by a decrease in pixel intensity (red square = ROI, quantified in b), with no big difference in pixel intensity at untreated hemisphere as a baseline (blue square = ROI, quantified in b). Signal intensity is normalized by setting the maximal value of ROIs as 1.

4.1.2. Real-time MRI for precise and local BBBO using mannitol

Immediately after the optimal infusion rate was determined for a particular mouse using SPIO, IA mannitol was infused at that rate for 1 min. To clearly present the MRI images, the signal change maps of SPIO-perfusion and Gd-contrast enhancement (Gd-CE) were calculated first (**Fig. 4 a,d**). As a consequence, such an approach resulted in an effective BBBO as reflected by Gd enhancement on the T1-weighted scan, which showed hyperintensity in the region previously highlighted by the contrast infusion (**Fig. 4 a,d**). The correlation between the SPIO-perfusion (**Fig. 4 a**) and Gd-CE (**Fig. 4 d**) MRI was determined. The histograms were drawn and fitted into two Gaussian distributions (**Fig. 4 b,e**). The values that corresponded to the minimal overlap between the two Gaussian functions were chosen to be the threshold that separated the pixels with a significant signal change. Using these determined thresholds, the areas with a significant signal change were determined (**Fig. 4 c,f**). For the four mice studied, the SPIO perfusion MRI showed an average signal change area of $26.00 \pm 5.60\%$, while Gd-CE showed an average signal change area of $26.52 \pm 5.33\%$, which was not significantly different ($P = 0.829$, **Fig. 4g**). A good correlation was shown between these two methods ($r = 0.937$, $R^2 = 0.879$, **Fig. 4h**). This indicated a successful BBBO by IA mannitol, as predicted by the perfusion pre-scan. Furthermore, the histopathological validation using EB, which is a gold standard for BBB assessment and rhodamine, which was used as a surrogate marker of therapeutic agents, demonstrated a pattern of extravasation that was consistent with MRI (**Fig. 4i-k**).

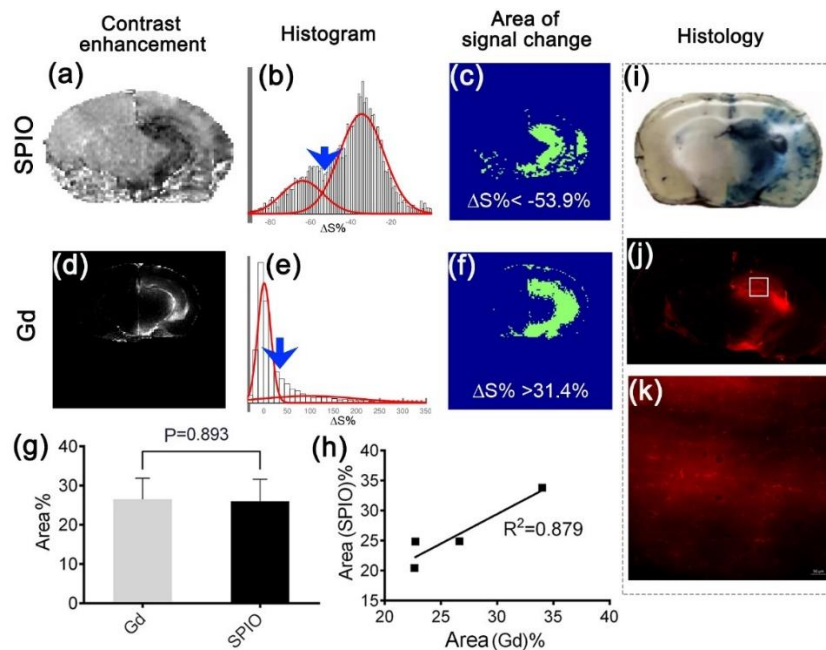


Figure 4. Prediction of mannitol induced BBBO territory. **a**, Signal change map after contrast perfusion. **b**, Histogram analysis of pixel intensities in **a**, showing two Gaussian distributions (red lines). The blue arrow indicates the point where a cut-off of -53.9% was used to separate the two distributions. **c**, Segmented map presents the area where the relative signal change was smaller than -53.9%. **d**, Signal change map, **e**, histogram analysis, and segmented map in **f** ($\Delta S\% > 31.4$) at 5 min after i.p. injection of Gd. **g**, Bar graph, and **h**, Correlation analysis of the BBBO territory predicted by the contrast perfusion and that assessed using Gd ($n = 4$). The histological analyses show the region with extravasation of EB (**k**) and rhodamine (**l**, **m**).

4.1.3. Safety and long-term consequences of IA mannitol-induced BBBO

To assess the safety of our BBBO protocol, mice were assessed for neurological and MRI sequelae. Three days after BBBO, MRI showed neither T2 abnormalities nor T1 Gd-enhancement (**Fig. 5a**), indicating that the procedure was safe and the BBB breach was transient, and did not cause permanent brain damage. Histology confirmed these observations with GFAP and IBA-1 staining 7 days post BBBO, in which there was no elevated astrocytic or microglia activation in the BBBO region, as measured by fluorescence intensity. There was no statistically significant difference in fluorescence intensity between the targeted region and the contralateral hemisphere ($P = 0.571$, $P = 0.093$; **Fig. 5b,c**). Similarly, there was no evidence of neuronal damage based on NeuN staining ($P = 0.331$, **Fig. 5d**).

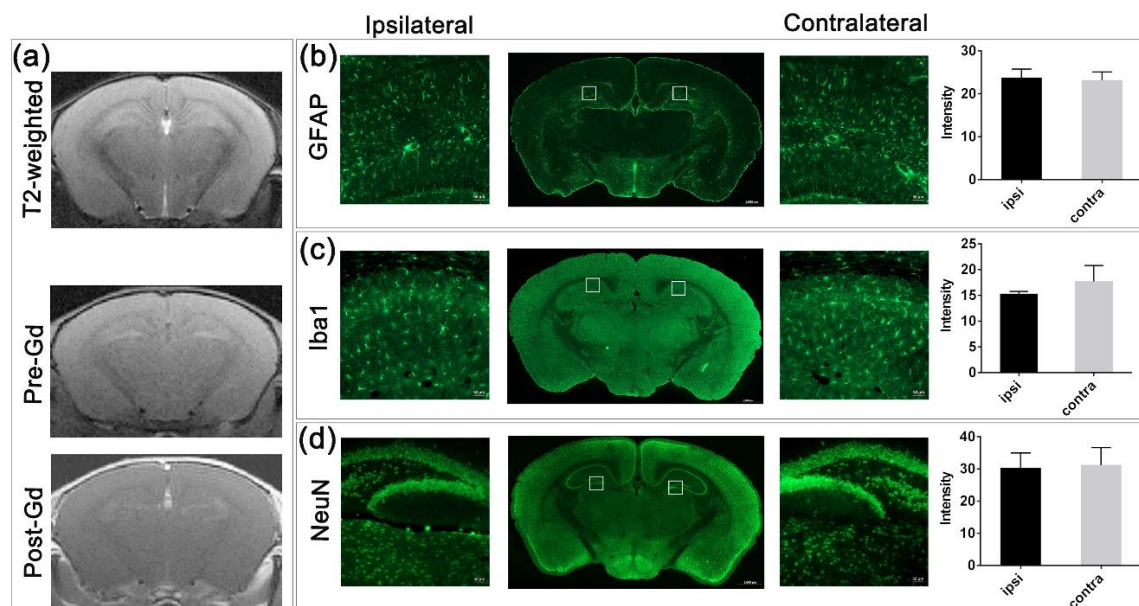


Figure 5. MRI and histological assessment post-BBBO. **a**, T2-weighted, pre-Gd, and post-Gd images 3 days after BBBO showed no sign of brain damage. No Gd-CE could be observed in the brain, suggesting that the BBB was resealed. Fluorescent staining of the BBBO region with GFAP (**b**), Iba1 (**c**), and NeuN (**d**) revealed comparable intensity between the ipsilateral and the contralateral hemisphere (2 ROIs/hemisphere as represented in lower magnification, $n = 4$) indicating no inflammation and no neuronal loss after BBBO.

4.2. Intra-arterial delivery resulted in a distinct brain uptake of a nanobody and similarly-sized PAMAM dendrimers with and without BBBO

4.2.1. Synthesis of ^{89}Zr -radiolabeled nanobody and PAMAM dendrimer

Synthesis of $^{89}\text{ZrNB}(\text{DFO})_2$

Preparation of $^{89}\text{ZrNB}(\text{DFO})_2$ involved conjugation of on average two DFO molecules as measured by MALDI-TOF spectrometry (data not shown) and subsequent radiolabeling with ^{89}Zr as presented in **Fig. 6**.

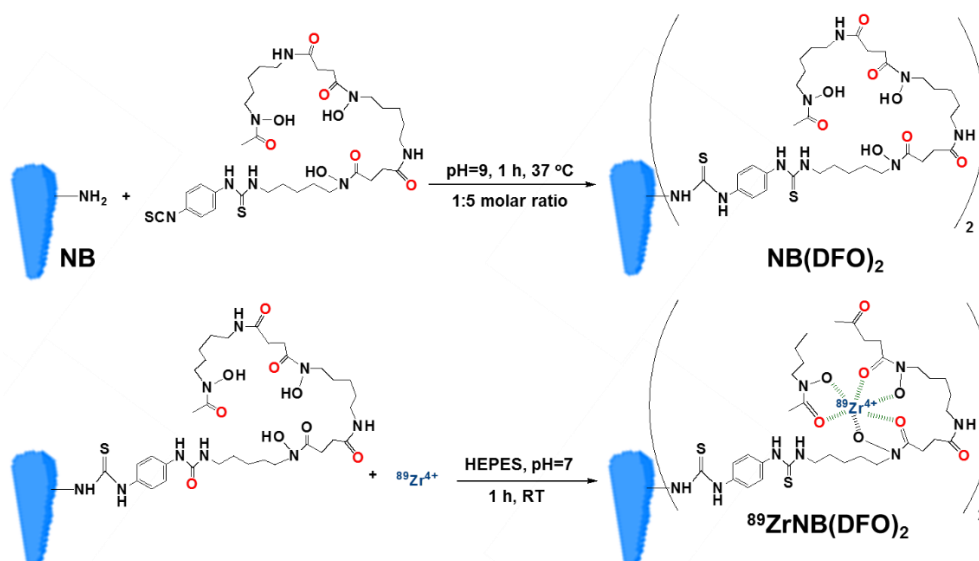


Figure 6. Conjugation of nanobody with DFO and radiolabeling with ^{89}Zr

Synthesis of $^{89}\text{ZrG4}(\text{DFO})_3(\text{Bdiol})_{110}$

As presented in the **Fig.7**, $\text{G4}(\text{NH}_2)_{64}$ was conjugated with on average three molecules of DFO and remaining primary amines were substituted with 110 butane-1,2-diol moieties, assessed by increase of the molecular weight observed in MALDI-TOF spectrometry (data not shown). Resulting $\text{G4}(\text{DFO})_3(\text{Bdiol})_{110}$ dendrimer was subsequently radiolabeled with ^{89}Zr and used for further studies.

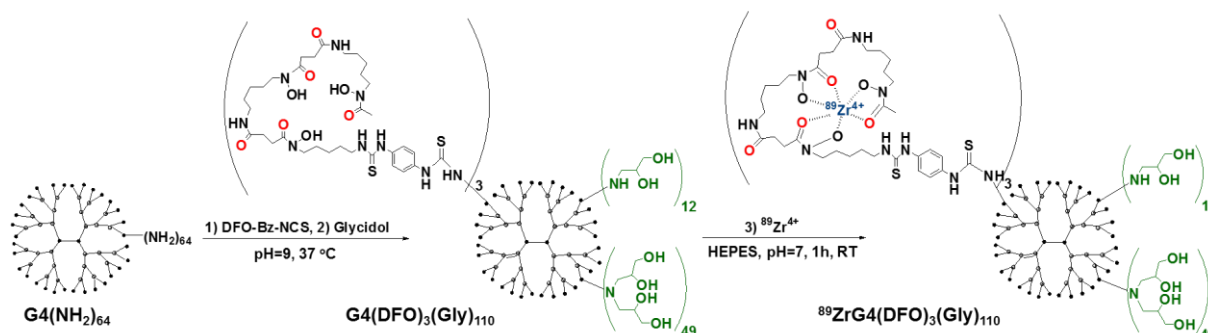


Figure 7. Conjugation of $\text{G4}(\text{NH}_2)_{64}$ dendrimer with DFO, followed by capping of primary amines with butane-1,2-diol moieties and radiolabeling with ^{89}Zr .

4.2.2. Brain uptake of ^{89}Zr -radiolabeled nanobody and PAMAM dendrimer and their biodistributions

Brain uptake of $^{89}\text{ZrNB(DFO)}_2$ and its biodistribution

Nearly linear uptake of radioactivity in the ipsilateral hemisphere was observed during IA infusions of $^{89}\text{ZrNB(DFO)}_2$ regardless status of BBB with no accumulation in the contralateral hemisphere (**Fig. 8**). The IA/BBBI infusion resulted in $^{89}\text{ZrNB(DFO)}_2$ accumulation in the ipsilateral hemisphere with a peak concentration of 25.79 ± 15.79 %ID/cc (percentage of injected dose per cubic centimeter of tissue, %ID/cc) and BBBO further enhanced its uptake to 60.66 ± 35.41 %ID/cc ($P < 0.05$). Only background radioactivity in the CNS was observed after IV infusion (1.93 ± 0.31 %ID/cc), which actually decreased after BBBO (1.59 ± 0.26 %ID/cc, $P < 0.05$). There was very slow early clearance of radioactivity from the ipsilateral hemisphere observed over a period of 30 minutes, which was non-significant for IA/BBBI (22.46 ± 15.05 , $P = \text{NS}$), but it was statistically different for BBBO/IA infusion (53.66 ± 30.73 , $P < 0.05$). The background radioactivity after IV/BBBO was not changed at the end of infusion (1.29 ± 0.25 , $P = \text{NS}$).

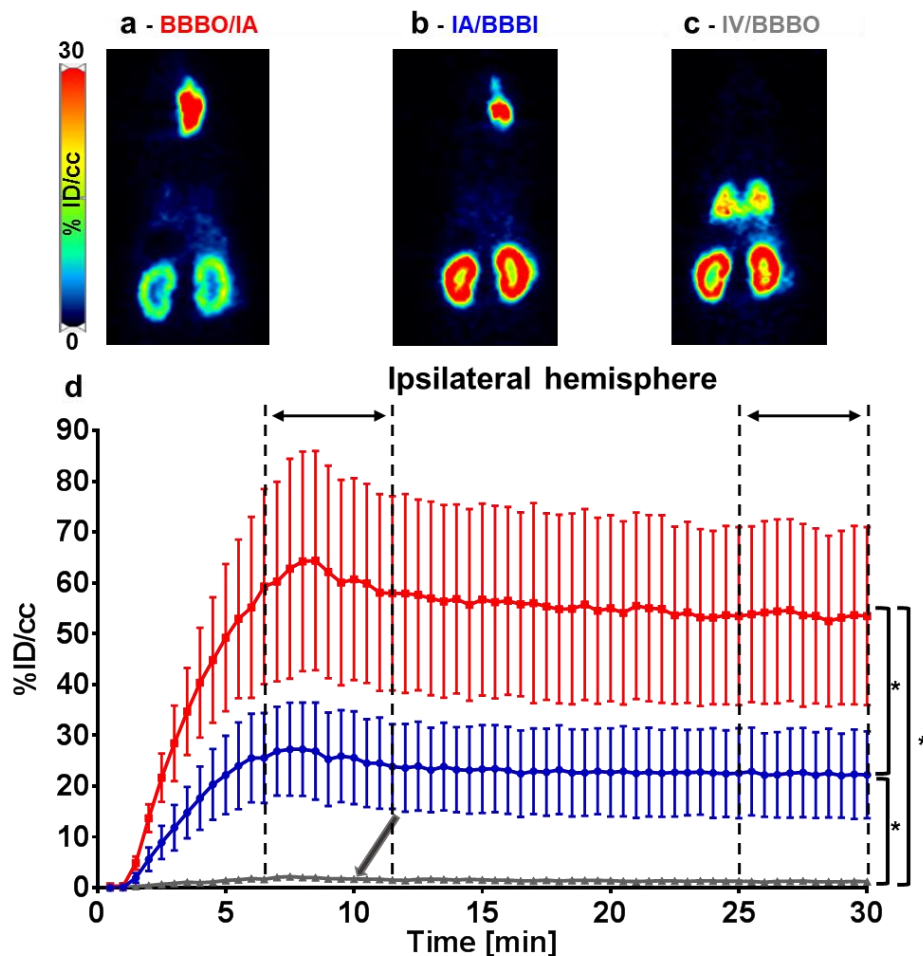


Figure 8. PET imaging and dynamics of $^{89}\text{ZrNB}(\text{DFO})_2$ uptake in ipsilateral hemisphere. Representative axial, sagittal and coronal PET images recorded 1 h after injection, illustrating brain uptake of $^{89}\text{ZrNB}(\text{DFO})_2$ upon: **a**, BBBO followed by immediate IA infusion of 8.5 MBq of $^{89}\text{ZrNB}(\text{DFO})_2$ reconstituted in 1 mL of saline at 0.15 mL/min, **b**, IA infusion with BBBI and **c**, IV infusion followed by BBBO at the 5 min after infusion was completed, showing the highest accumulation of radioactivity in ipsilateral hemisphere upon BBBO/IA, **d**, curves demonstrating dynamics of $^{89}\text{ZrNB}(\text{DFO})_2$ uptake in the ipsilateral hemisphere upon BBBO/IA (red line), IA/BBBI (blue line), and IV/BBBO (gray line, arrow shows time of BBBO) indicating highest uptake of $^{89}\text{ZrNB}(\text{DFO})_2$ in animals treated with BBBO and IA infusion, each time point is presented as mean and SEM, n=4. %ID/cc = percentage of injected dose per cubic centimeter of tissue.

The whole body PET-CT imaging performed 1 h after infusion revealed similar pattern of radioactivity uptake in the brain as at the end of dynamic PET scan, which then decreased nearly by 50% at 24 h after infusion ($P < 0.05$, **Fig.9**). In all evaluated cohorts high uptake of radioactivity was also observed in kidney indicating fast renal clearance (**Fig.8,9**). High accumulation of $^{89}\text{ZrNB}(\text{DFO})_2$ in the ipsilateral hemisphere upon BBBO/IA infusion resulted in its statistically relevant lower concentration in kidneys at 1 h after infusion (26.72 ± 4.19) in comparison to IA/BBBI (43.36 ± 3.83) and IV/BBBO (39.61 ± 7.51 %ID/cc). The clearance of $^{89}\text{ZrNB}(\text{DFO})_2$ from brain over 24 h resulted in increase of radioactivity in kidneys to 35.38 ± 5.11 %ID/cc in BBBO/IA group, while no difference was observed for remaining experimental groups (41.84 ± 5.47 and 40.34 ± 7.91 %ID/cc for IA/BBBI and BBBO/IV, respectively). For IV/BBBO infusion 12.48 ± 2.32 %ID/cc of $^{89}\text{ZrNB}(\text{DFO})_2$ could also be detected in the lungs 1 h after infusion. In agreement with PET-CT imaging post mortem biodistribution analysis (**Fig.9b**) revealed significantly higher accumulation of $^{89}\text{ZrNB}(\text{DFO})_2$ in the ipsilateral hemisphere in BBBO/IA (17.8 ± 5.99 %ID/g) compared to IA/BBBI (6.15 ± 3.53 %ID/g) and IV/BBBO (0.09 ± 0.03 %ID/g) infusions with negligible radioactivity uptake in the contralateral hemispheres in all mice 24 h after infusion. Among peripheral organs the highest accumulation of $^{89}\text{ZrNB}(\text{DFO})_2$ was detected in kidneys followed by spleen, liver and lungs.

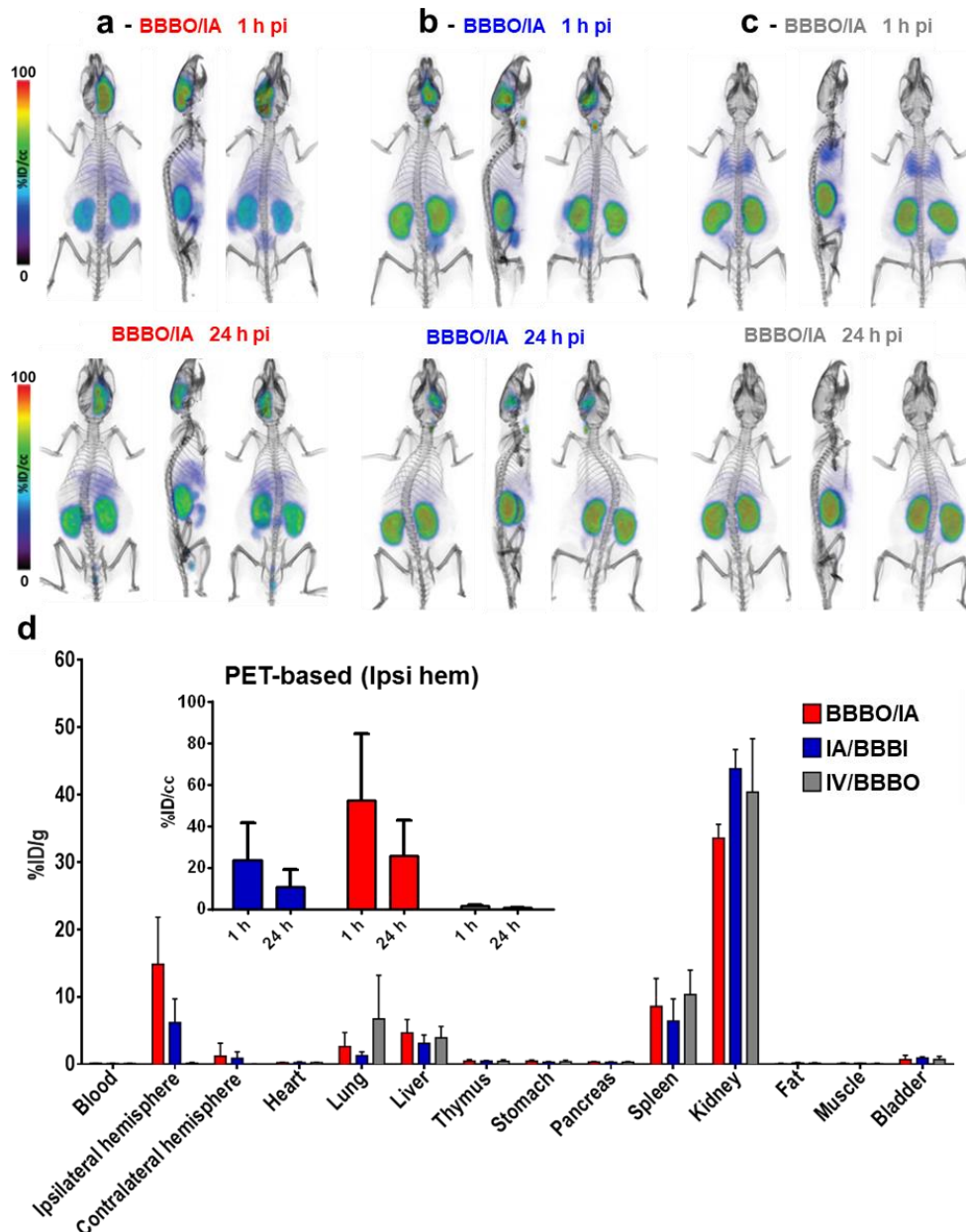


Figure 9. PET-CT imaging and ex vivo biodistribution of $^{89}\text{ZrNB}(\text{DFO})_2$ at 24 h after infusion. Whole body volume rendered PET-CT images recorded 1 h and 24 h post infusion of ~ 8.5 MBq (~ 230 μCi) of $^{89}\text{ZrNB}(\text{DFO})_2$, demonstrating its biodistribution upon: **a**, BBBO followed by immediate IA infusion, **b**, IA infusion with BBBI and **c**, IV infusion followed by BBBO 5 min after infusion was completed. **d**, Ex vivo biodistribution of $^{89}\text{ZrNB}(\text{DFO})_2$ at 24 h after infusion in the same groups (insert - PET-based quantification of $^{89}\text{ZrNB}(\text{DFO})_2$ uptake in ipsilateral hemisphere), showing in agreement with PET imaging higher uptake of $^{89}\text{ZrNB}(\text{DFO})_2$ in ipsilateral hemisphere compared to contralateral hemisphere in BBBO/IA group and its higher brain accumulation in comparison with IA/BBBI and IV/BBBO cohorts. %ID/g = percent of injected dose per gram of brain tissue.

Brain uptake of $^{89}\text{ZrG4}(\text{DFO})_3(\text{Bdiol})_{110}$ and its biodistribution

There was no difference in the peak concentration of $^{89}\text{ZrG4}(\text{DFO})_3(\text{Bdiol})_{110}$ in the ipsilateral hemisphere for IA/BBBI ($3.29 \pm 1.31\% \text{ID/cc}$) and BBBO/IA ($3.20 \pm 1.47\% \text{ID/cc}$) infusions ($P = \text{NS}$) as indicated by the time activity curves and PET images obtained by summing frames collected between 5 and 10 min of dynamic scans (**Fig.10**). IV/BBBO infusion resulted with background radioactivity uptake of $1.22 \pm 0.29\% \text{ID/cc}$ in the CNS, with decrease of radioactivity after BBBO to 1.1 ± 0.25 ($P < 0.05$). The fast and statistically significant clearance of $^{89}\text{ZrG4}(\text{DFO})_3(\text{Bdiol})_{110}$ from the brain was observed regardless BBB status and it reached at the end of dynamic PET scan: 1.68 ± 0.8 , 1.05 ± 0.22 , $0.83 \pm 0.18\% \text{ID/cc}$ for BBBO/IA, IA/BBBI and BBBO/IV, respectively. However, the clearance after BBBO/IA was somewhat slower compared to IA/BBBI ($P < 0.05$). IA/BBBI actually dropped to the same low level as IV/BBBO ($P = \text{NS}$) at the end of dynamic scans. However, the whole-body PET-CT imaging performed 1 h after infusion showed only background radioactivity in the brain regardless route of $^{89}\text{ZrG4}(\text{DFO})_3(\text{Bdiol})_{110}$ delivery with no statistically significant differences among groups (**Fig.11**). Significant amount of radioactivity could be detected in kidneys and bladder, followed by liver at 1 h after infusion, indicating fast renal clearance with minor hepatic involvement. At 24 h after infusion no radioactivity in the brain of all evaluated mice was observed. In agreement with PET-CT imaging postmortem biodistribution demonstrated negligible accumulation of $^{89}\text{ZrG4}(\text{DFO})_3(\text{Bdiol})_{110}$ in both hemispheres ($P = \text{NS}$) for and exclusive presence of radioactivity in kidneys and liver for all assessed delivery routes (**Fig.11**).

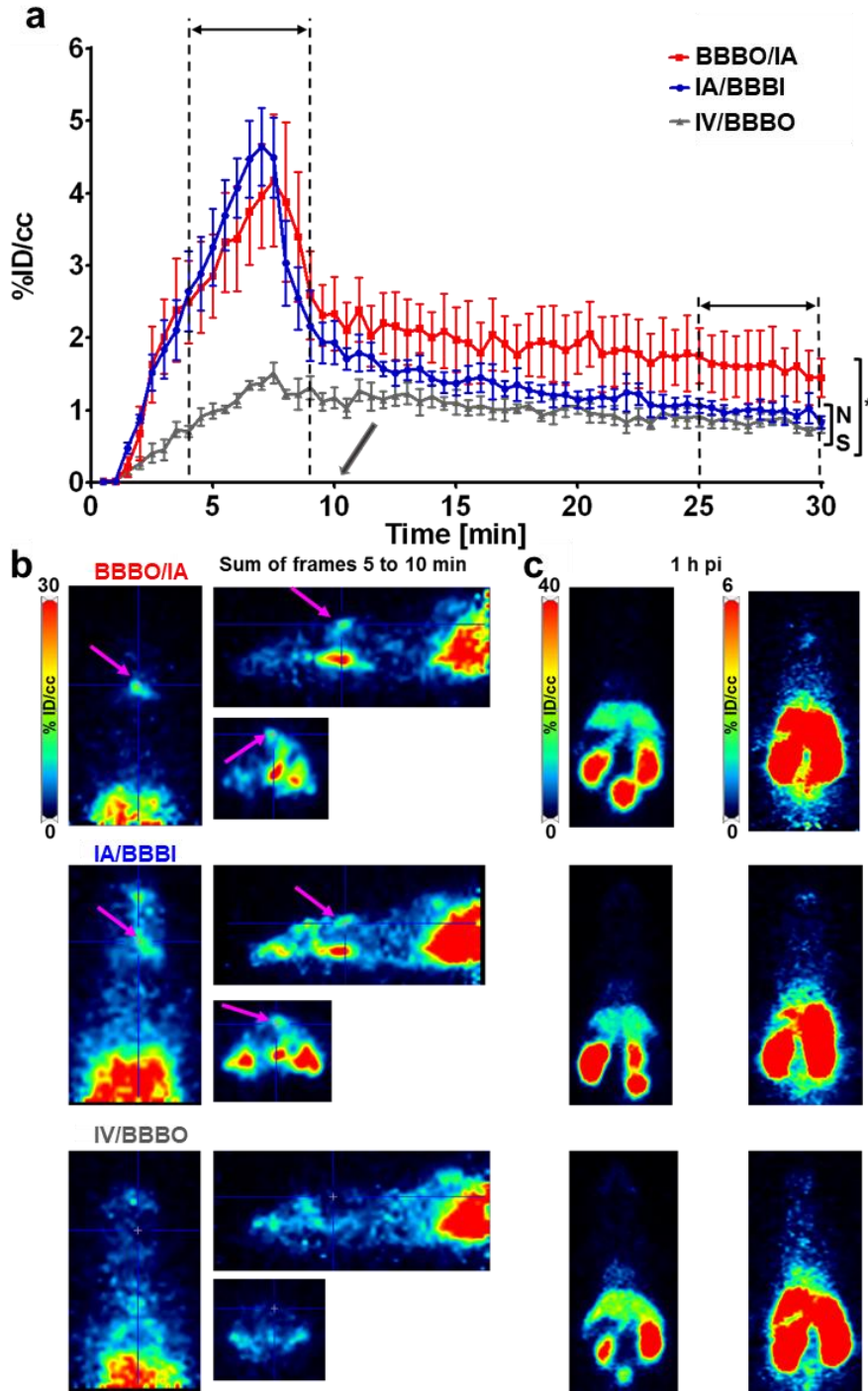


Figure 10. Time activity curves of $^{89}\text{ZrG4(DFO)}_3(\text{Bdiol})_{110}$ uptake in ipsilateral hemisphere and corresponding PET imaging. **a**, Curves demonstrating dynamics of $^{89}\text{ZrG4(DFO)}_3(\text{Bdiol})_{110}$ accumulation in the ipsilateral hemisphere upon BBBO/IA (red line), IA/BBBI (blue line), and IV/BBBO (gray line, arrows show when BBB was opened) indicating significantly lower uptake compared to $^{89}\text{ZrG4(DFO)}_3(\text{Bdiol})_{110}$ and no benefits of BBBO application, each time point is presented as mean and SEM, n=4; **b**, Representative orthogonal PET images obtained by summing frames between 5 and 10 min acquired during 30 min long dynamic scans; **c**, Representative axial PET images with scales adjusted to demonstrate whole body distribution of radioactivity (left panel) and absence of $^{89}\text{ZrG4(DFO)}_3(\text{Bdiol})_{110}$ in the brain (right panel) 1 h after infusion. Results demonstrate negligible retention of $^{89}\text{ZrG4(DFO)}_3(\text{Bdiol})_{110}$ in the brain regardless BBB status and route of administration.

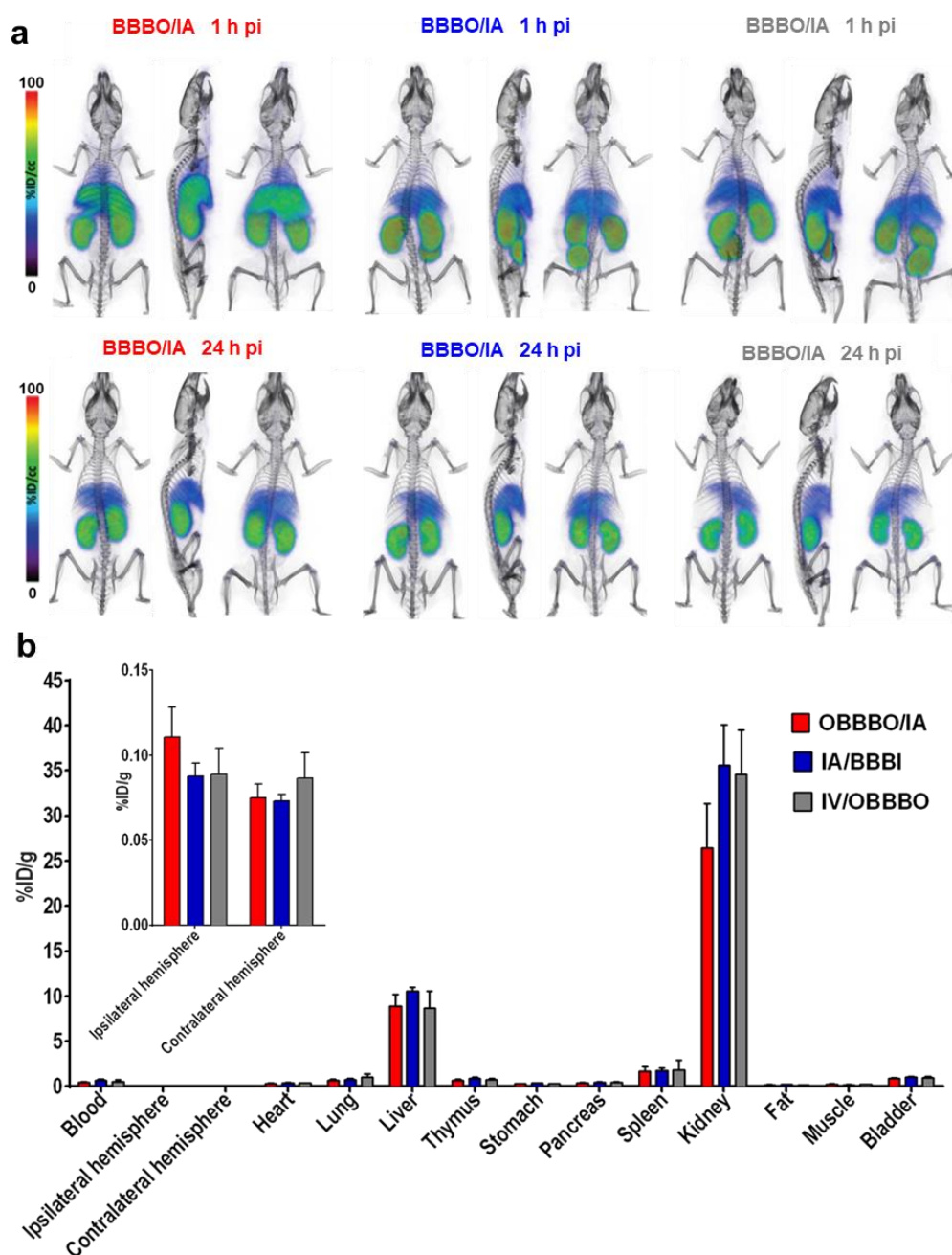


Figure 11. PET-CT imaging and ex vivo biodistribution of $^{89}\text{ZrG4}(\text{DFO})_3(\text{Bdiol})_{110}$. **a**, representative whole body volume rendered PET-CT images recorded 1 h and 24 h post infusion of $^{89}\text{ZrG4}(\text{DFO})_3(\text{Bdiol})_{110}$ for BBBO/Al, Al/BBBI and IV/BBBO infusions; **b**, ex vivo biodistribution of $^{89}\text{ZrG4}(\text{DFO})_3(\text{Bdiol})_{110}$ at 24 h after infusion in the same mice (insert-scale was adjusted to show brain accumulation of $^{89}\text{ZrG4}(\text{DFO})_3(\text{Bdiol})_{110}$, indication lack of $^{89}\text{ZrG4}(\text{DFO})_3(\text{Bdiol})_{110}$ retention on the brain regardless method of administration and its renal clearance with minor hepatic uptake).

4.3. Intravital microscopy visualized the BBBO and drug targeting in mouse cortex

4.3.1. Hyperosmolar BBBO in cerebral cortex under MRI guidance

4.3.1.1. Temporary closure of contralateral CCA facilitates cortical perfusion

Across the 26 mice we found that using infusion rate of 0.15 ml/min, we observed variability in cortical involvement. As a result, IA infusion of a contrast agent via ICA with dynamic GE-EPI imaging revealed T2* hypointensity in cerebral cortex at a frequency of 23.07%. The lack of cortical perfusion using this delivery route was observed much more frequently (76.93%). We found temporary closure of the contralateral CCA redistributed the cerebral blood flow opening up the cortex for the catheter infusion in animals lacking trans-catheter perfusion through the cortex (drop of T2* signal) (**Fig. 12a**). The dynamic signal changes for two selected ROIs are shown in **Fig. 12b**. There was a steep and early drop in the signal intensity in the hippocampus (ROI2), at that time the signal intensity in the cortex (ROI1) remained unchanged and dropped only after temporary closure of the contralateral CCA.

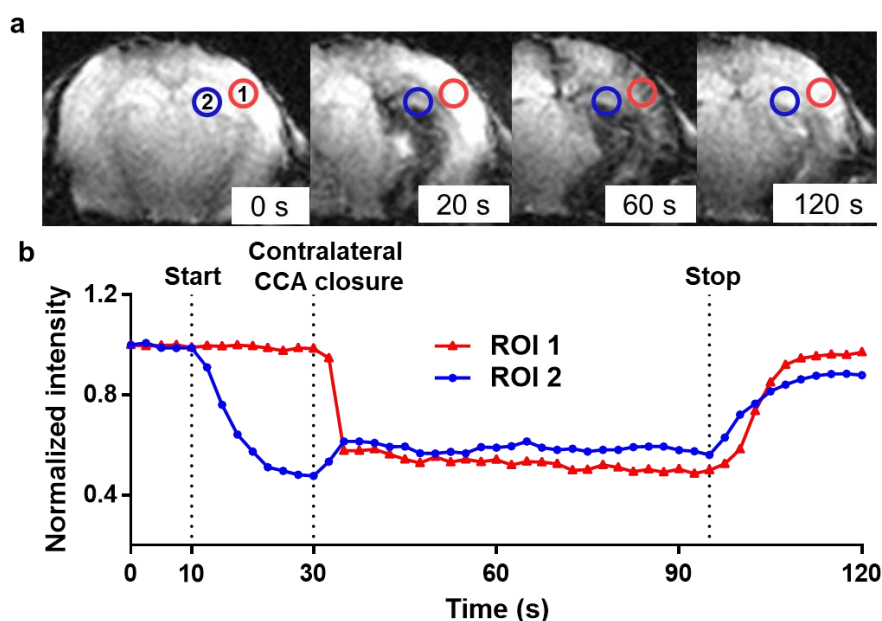


Figure 12. Use of real-time MRI to visualize the effect of contralateral CCA closure on cortical trans-catheter perfusion. **a**, Representative T2* images before (0s), 20 s, 60 s and 120 s after infusion of Gd at the rate of 0.15 ml/min. **b**, Dynamic signal changes for two ROIs marked in (a). Graph lines and ROIs are shown in corresponding colors. Start represents the beginning of IA Gd infusion. Stop represents the end of the infusion.

4.3.1.2. Osmotic disruption of the BBB in cerebral cortex using real-time MRI guidance

Immediately after confirming trans-catheter Gd perfusion in the cortex with IA infusion of the contrast agent (**Fig. 13a**), IA mannitol was infused using the same parameters. Effective BBBO was reflected by Gd enhancement on the T1-weighted scan in the region previously highlighted by the contrast infusion (**Fig. 13d**). The correlation between the Gd perfusion (**Fig. 13a**) and Gd enhancement (**Fig. 13b**) MRI was determined using the same method we described above. Briefly, the histograms were drawn and fitted into two Gaussian distributions (**Fig. 13b,e**). The values were calculated and chosen to be the threshold that separated the pixels with a significant signal change. Using these thresholds, the areas with significant signal change were determined (**Fig. 13c,f**). For the four mice studied, the Gd perfusion MRI showed an average signal change area of $27.13 \pm 2.36\%$, while Gd enhancement showed an average signal change area of $26.50 \pm 3.40\%$, which was not significantly different ($P = 0.663$, **Fig. 13g**). A strong correlation was shown between these two methods ($R^2 = 0.946$, **Fig. 13h**). This indicated a successful BBBO in cortex by IA mannitol, as predicted by the perfusion pre-scan. Furthermore, the histopathological validation using EB, which is state of the art technique for BBB assessment, displayed a pattern of extravasation that was consistent with MRI (**Fig. 13i**).

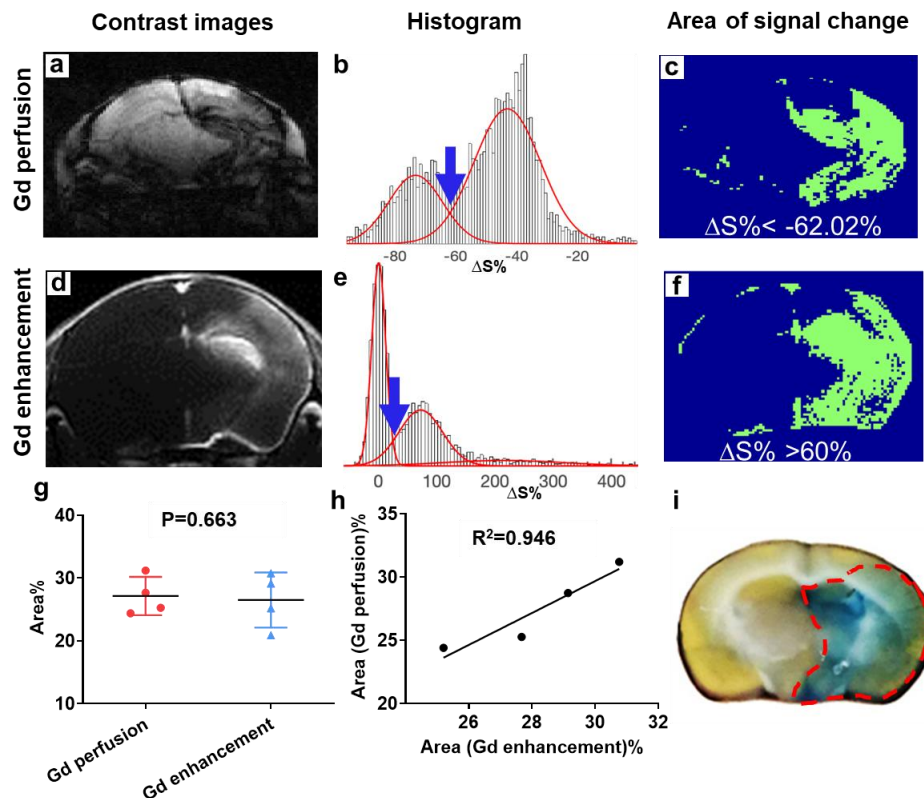


Figure 13. Real-time MRI for predictable BBBO with histological validation. **a, d**, Representative T2* images of Gd perfusion. **b**, Histogram analysis of pixel intensities in **(a)**, showing two Gaussian distributions (red lines). Blue arrow points to where a cut-off of -62.02% was applied to separate the two distributions. **c**, Segmented map shows the area where the relative signal change was smaller than -62.02%. **d**, Gd enhancement map, **e**, histogram analysis, and **f**, segmented map ($\Delta S\% > 60\%$) right after mannitol infusion ended. **g**, Scatter graph and **h**, correlation analysis of the BBBO territory predicted by Gd perfusion and assessed using Gd enhancement ($n = 4$). **i**, The histological analyses show the region with extravasation of EB.

4.3.1.3. Safety and long-term consequences of IA mannitol-induced BBBO in the cortex

Three and seven days after BBBO, T2w MRI did not detect any asymmetry or hyperintensity, suggesting a lack of edema or inflammation, T2*w scans were not indicative of microhemorrhages and a lack of Gd-enhancement on T1w images revealed an intact BBB (**Fig.14a**), overall suggesting that the procedure is safe and the BBB breach was transient. Histology corroborated these observations with GFAP and IBA-1 staining 7 days post BBBO, in which there was no evidence of astrocytic or microglial activation in the BBBO region, as determined by comparing the fluorescence intensity between the targeted region and the corresponding area in the contralateral hemisphere ($P = 0.344$, $P = 0.073$; **Fig. 14b,c**). Overall, both MRI and histologic appearance confirmed that the procedure did not cause brain damage.

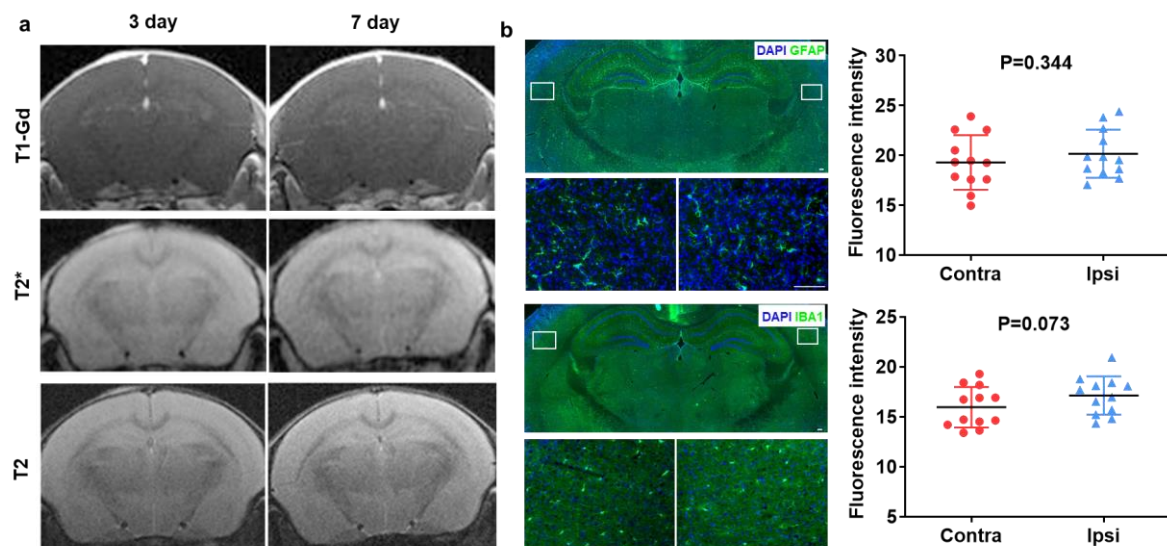


Figure 14. MRI and histological assessment post-BBBO. **a**, 3 and 7 days after BBBO, T2-w and T2* w images did not indicate brain damage. No Gd enhancement in T1 images was observed in the brain, revealing that the BBB was resealed. Fluorescent staining of the BBBO region with GFAP (**b**) and IBA1 (**c**) showed comparable intensity between the ipsilateral and the contralateral hemisphere (3 ROIs/hemisphere as represented in lower magnification), indicating no inflammation after BBBO. Scale bar = 100 μ m.

4.3.2. Vascular trans-catheter perfusion in mouse cortex through a cranial window

With the goal of developing a protocol enabling comprehensive assessment of cortical BBB, including intravital microscopy, we implanted cranial windows and head posts ($n = 5$) (**Fig. 15a**). After allowing the animals to heal for one week, the mice were catheterized intra-arterially and placed under epi-fluorescent microscopy. Rhodamine was infused via the catheter to verify perfusion and display the cortical vascular architecture. In an agreement with the observation under MRI, cortical perfusion was observed rarely, as visualized during IA infusion bolus of rhodamine (**Fig. 15b**). In those animals, the dynamic signal changes showed steep increase for the duration of bolus infusion consistently for cortical vessels (**Fig. 15c**). In the majority of animals, however, sparse or none cerebral arteries and microvessels were perfused and temporary contralateral CCA closure was required to rapidly increase and broaden perfusion territory in the cortex. The dynamic assessment of that scenario is quantitatively represented in **Fig. 15e**.

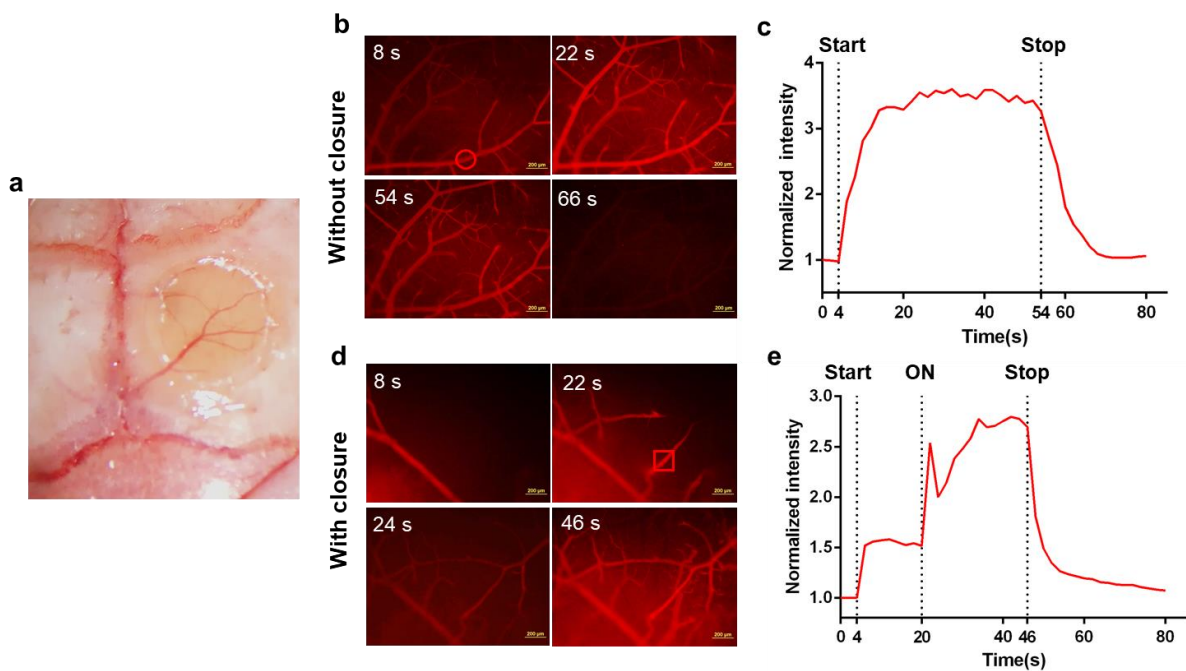


Figure 15. Visualization of cortical perfusion in epifluorescence microscopy. **a**, The cranial window for microscopic imaging. **b**, Representative fluorescent images show the perfusion territory of rhodamine without contralateral CCA closure. **c**, Dynamic signal changes of the ROI (circle) marked in (b). **d**, Representative fluorescent images show the change of perfusion territory in the cortex pre-and post-contralateral CCA closure. **e**, Dynamic signal changes of the ROI (square) marked in (d). Start represents the beginning of rhodamine infusion. ON represents the weight is engaged. Stop represents the end of the infusion.

4.3.3. Intravital multiphoton microscopy for visualization of cortical BBBO and drug extravasation

The cerebral vasculature at ~100 μm depth into the cortex was visualized with 2PM upon IA injection of rhodamine. Once cortical perfusion was achieved, infusion (2 min IA bolus) of a mixture of mannitol, rhodamine and bevacizumab-FITC was initiated; however, infiltration was not observed. Subsequently, another infusion (1 min bolus) was performed, the BBB was breached, and a final infusion (1 min bolus) was performed, for a total of 4 minutes of infusion time, which resulted in a more robust penetration into the cortical parenchyma (**Fig. 16a**). The 0.58 kDa rhodamine extravasated the cortex earlier compared to 153 kDa bevacizumab-FITC. The fluorescence intensity changes located in the parenchyma was measured to exhibit dynamics of BBB permeability for rhodamine and bevacizumab-FITC. As anticipated, there was earlier onset and higher intensity of extravasation for rhodamine upon BBBO compared to bevacizumab-FITC. The half-time of rhodamine and bevacizumab-FITC reaching their maximum was 526.2 s and 618.6 s, respectively (**Fig. 16b**).

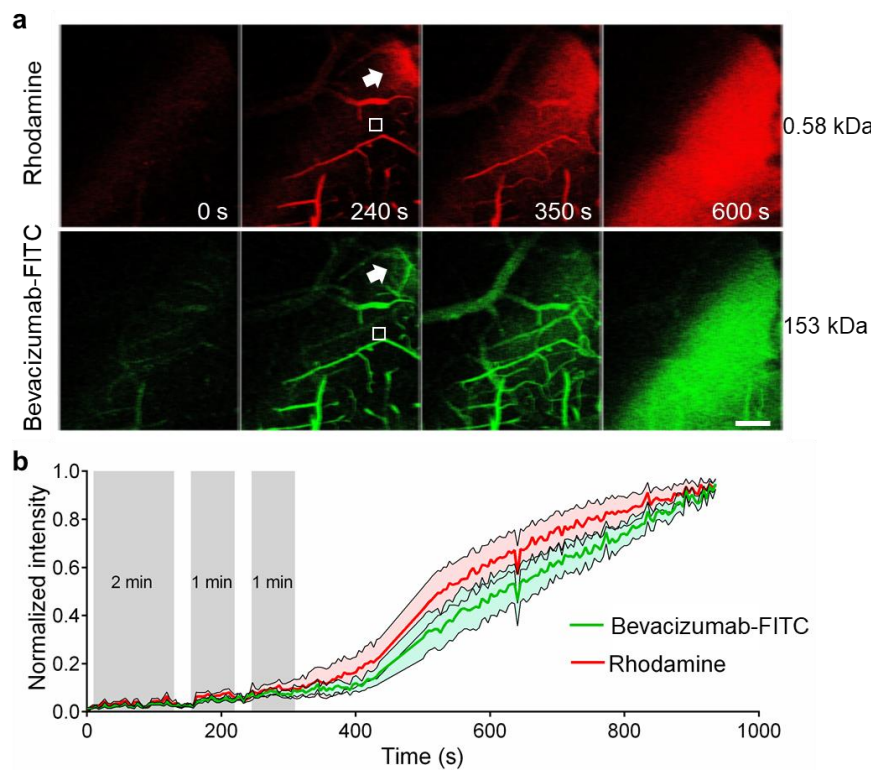


Figure 16. Intravital 2PM visualization of cortical BBBO and drug extravasation. **a**, Representative 2PM images showed the vessels permeability to rhodamine and bevacizumab. The arrow points to where BBB disruption started. **b**, Quantitative measurement of fluorescent signal intensities in the selected extravascular regions marked in (a) over 15 min long dynamic imaging. The data was presented as mean \pm SEM from 7 ROIs. The grey shading indicated the IA infusion periods. Scale bar = 50 μm .

4.3.4. Histological confirmation of bevacizumab extravasation

Cryosectioned brain tissue samples collected one hour after IA delivery of bevacizumab with intact BBB (BBBI) showed modestly increased uptake of bevacizumab delivery to the target (ipsilateral side), however, it was localized to the blood vessels (**Fig. 17a**). For the IA delivery with BBBO, accumulation of bevacizumab was observed in both blood vessels and parenchyma (**Fig. 17b**). Additionally, BBBO appeared to potentiate the vascular concentration of bevacizumab. As measured by the fluorescence intensity, there was significantly higher uptake of bevacizumab in ipsilateral vs. contralateral hemisphere in both groups ($P < 0.001$, **Fig. 17c, d**), but the ipsi-/contralateral ratio was more pronounced (~2 fold higher) when the BBB was opened ($P < 0.001$, **Fig. 17e**). These observations demonstrated that IA delivery of bevacizumab into the brain across an osmotically opened BBB is more effective compared to the intact BBB (BBBI).

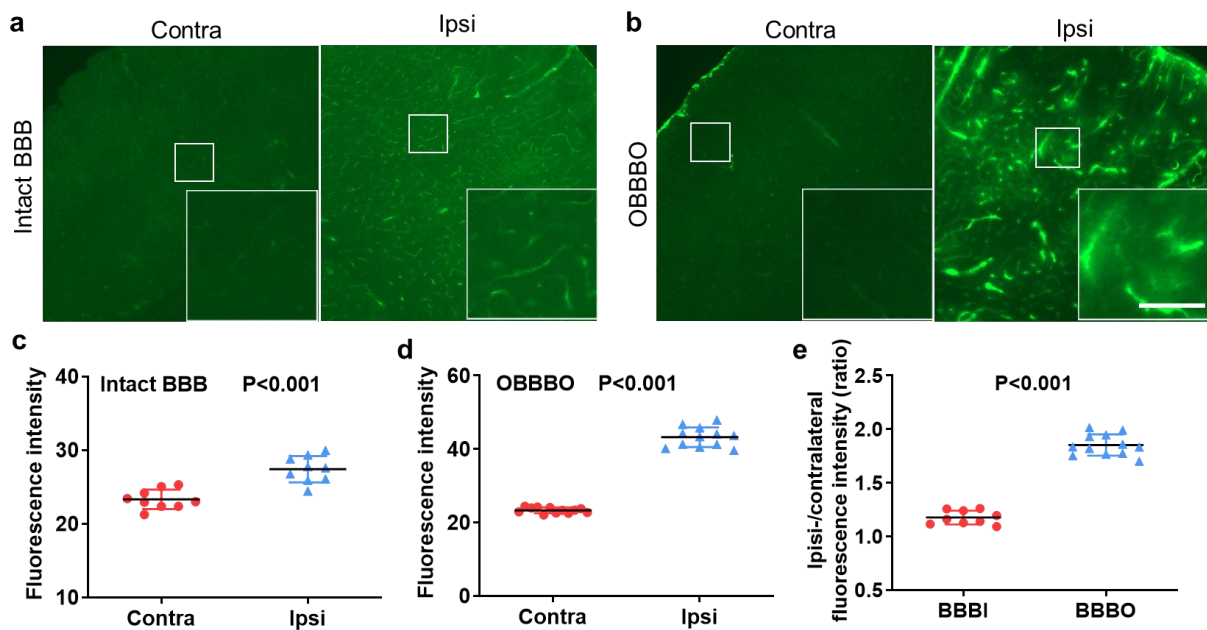


Figure 17. Histological assessment of bevacizumab biodistribution and extravasation. a, b, Coronal fluorescent images of mouse cerebral cortex showed the distribution of infused bevacizumab in animals with intact BBB and BBBO. c, d, Quantification of fluorescence intensity of bevacizumab between the ipsilateral and contralateral hemisphere. e, The ipsi-/contralateral ratio values were higher when the BBB was opened compared to that in animals with intact BBB. Measurements are sampled from 3 ROIs/hemisphere as represented in lower magnification. Scale bar = 50 μ m.

5. Discussion

5.1. Real-time MRI enables a safe and reproducible local BBBO

The overall goal of BBBO is to maximize CNS targeting of the therapeutic agent while minimizing systemic toxicity. Various methods and drugs have been developed to induce transient permeabilization of the BBB, with IA mannitol-mediated osmotic disruption being the most frequently used procedure in both preclinical and clinical studies⁶⁻⁸. Although osmotic BBBO has been an established method for decades, the parameters for inducing BBBO are highly variable and inconsistent. Indeed, we have shown that IA infusion into the rat internal carotid artery at rates exceeding 0.9 ml/min is damaging and results in scattered white matter hyperintensities⁴⁹. Here, we also found severe damage when the speed reached 0.2 ml/min indicating fine balance effective BBBO and damage. We also believe that PPA obstruction is necessary to route the entire contrast agent and mannitol volume to the cerebral arteries⁵⁰. Thus, we exploited dynamic susceptibility contrast MRI for perfusion prediction prior to BBBO. We escalated the rate from a low speed, increasing in 0.05 ml/min increments until the desired perfusion territory was reached. The extravasation of rhodamine and Evans blue corroborated the efficacy of BBBO, therefore suggesting that IA mannitol-mediated local BBBO is predictable and can be targeted to a specific region. The IA route for BBBO also allows immediate IA delivery of a specific drug during the same procedure, thus providing a “one-stop-shop” and improving the probability to achieve an adequate therapeutic concentration.

5.2. IA delivery results a distinct brain uptake regardless of BBB status for nanobodies but not for PAMAM dendrimers

After we developed the BBBO model in mice, a monoclonal antibody (bevacizumab radiolabeled with ⁸⁹Zr) was tested using the platform⁵¹. We observed a linear increase in the concentration of bevacizumab via IA route compared with IV route. Furthermore, the osmotic BBBO strongly enhanced uptake of antibodies. While antibodies are quickly emerging as therapeutics, their disadvantages such as large size, production logistics and immunogenicity motivate search for alternatives. Thus we have studied the brain uptake of nanobody (Gelsolin nanobody 11) and a drug nanocarrier (PAMAM dendrimers). As a result, we found that the IA route was more effective in delivering nanobodies to the brain than systemic administration, regardless of the BBB status. Preceding BBBO potentiated brain accumulation of the nanobodies by ~2.5-fold. Brain uptake of ⁸⁹ZrNB(DFO)₂ reached 60.66±35.41 %ID/cc, which is

higher compared to brain accumulation of 23.58 ± 4.58 %ID/cc for ^{89}Zr radiolabeled-bevacizumab ($^{89}\text{ZrBVDFO}$)⁵¹. While half of the $^{89}\text{ZrNB}(\text{DFO})_2$ was cleared from the brain over 24 h, clearance of $^{89}\text{ZrBVDFO}$ was slower. In both studies, bevacizumab and the nanobody did not have specific targets in mouse brains. In contrast to antibody and nanobody, brain retention of generation-4 hydroxy terminated PAMAM dendrimer was marginal. The peak concentration of $^{89}\text{ZrG4}(\text{DFO})_3(\text{Bdiol})_{110}$ in the brain was only 3 %ID/cc after IA delivery regardless of BBB status, decreasing to background levels within 1 h. Intravenous infusion of $^{89}\text{ZrNB}(\text{DFO})_2$ and $^{89}\text{ZrG4}(\text{DFO})_3(\text{Bdiol})_{110}$ resulted in only background tracer retention regardless of BBB status. The results are in agreement with previous reports showing negligible penetration of PAMAM dendrimers through intact BBB upon IV administration, regardless of their size and terminal functionalities, including hydroxy, carboxyl and polyethylene glycol groups⁵²⁻⁵⁴. A very low brain uptake of ~ 0.07 %ID/g in neonatal rabbits with cerebral palsy and 0.003 %ID/g healthy control pups for the same dendrimer at 24 h after injection was also reported⁵⁵. In agreement with our results, demonstrated marginal BBB permeability and brain retention of generation-4 hydroxy terminated PAMAM dendrimers even with a compromised BBB or activated microglia present in cerebral palsy model. Interestingly, PET imaging of generation-4 hydroxy terminated dendrimer-radiolabeled with copper-64 in newborn rabbits with cerebral palsy indicated brain accumulation of radioactivity around 2.5 %ID/cc 24 h after injection⁵⁶. However, copper-64 undergoes trans-chelation *in vivo*, in particular in the absence of a strong Cu(II) chelator forming thermodynamically stable complexes⁵⁷.

Our $^{89}\text{ZrNB}(\text{DFO})_2$ and $^{89}\text{ZrG4}(\text{DFO})_3(\text{Bdiol})_{110}$ were not targeted to specific molecular species within the BBB or the brain. Also, no disease model was induced, enabling testing as a baseline therapeutic delivery platform for CNS drug delivery. In this context, the nanobodies seem attractive for IA infusion, while a lot of caution should be taken regarding utility of PAMAM dendrimers as drug delivery vehicles for brain diseases, especially when they are administered systemically. Therefore, in case of PAMAM dendrimers the challenge for appropriate surface modification to achieve appreciable brain uptake and retention remains open. While here we tested generation-4 hydroxy terminated PAMAM dendrimers constructed by capping the primary amines with butane-1,2-diol, the same dendrimers with different surface modifications can potentially exhibit higher brain retention and our study may serve as a benchmark for quantitative performance of dendrimer-based diagnostics and therapeutics in the CNS

diseases. In contrast, IA route is very effective in delivery of nanobodies and their relatively fast clearance comparing to antibody could potentially be mitigated by applying nanobodies aimed for specific brain target. While, IV administration is highly ineffective for delivery of nanobodies to the brain, it was recently reported that intranasal route might be an alternative⁵⁸. However, no quantitative assessment of intranasal brain delivery of nanobodies has been reported yet. There is a progress in design of nanobodies against brain disorders⁵⁹, and our IA infusion might be a right approach to use them effectively in the clinic. Especially, after the anti-tumoral activity of neutralizing antibodies was shown in a mouse model of melanoma, the potentially neutralizing nanobodies could also be created against brain targets⁶⁰.

5.3. Intravital imaging confirmed the drug penetration post BBBO

Although PET can provide quantitative data for drug uptake in the brain, the relatively low spatial resolution precluded assessment as to whether the accumulation was solely on the endothelial level or the therapeutics penetrated into the brain parenchyma. The last goal in this project is to optimize IA drug delivery in mice to facilitate multi-scale dynamic imaging studies of BBBO. BBBO in mice has been previously reported and several studies showed successful BBB breach in the entire hemisphere including the cortex^{10, 14, 61}; however, those published studies utilized a high IA infusion rate exceeding the safe physiological perfusion rate for the carotid artery, and it has been reported by us and others that excessive infusion rate has a direct damaging effect on the BBB and the brain^{40, 49, 62-63}. Our previously optimized procedure for safe, transient opening of the BBB without neurological consequences but the territory of BBB opening rarely included the cortex. This phenomenon is likely due to redundancy in vascularization of the cortex supplied by more than one major cerebral artery eventually leading to mixing and dilution of IA mannitol⁶⁴⁻⁶⁵. In order to prevent this situation, here, we temporarily occluded the contralateral CCA for the duration of mannitol injection and that intervention was sufficient for the ipsilateral cortex to be perfused from the catheter and therefore disrupt the cortical BBB as shown by real-time MRI. This experimental platform was then exploited for studying the mechanism of drug extravasation using intravital microscopy. Dynamic imaging during IA infusion allowed us to visualize and track the leakage of fluorescent dyes upon BBBO, showing that rhodamine extravasated earlier and led to higher parenchymal accumulation than monoclonal antibody. This observation is consistent with a study of focused ultrasound (FUS)-induced BBBO reported by Nhan. et al, which demonstrated

fast leakage for small sized molecules⁶⁶. Indeed, FUS is emerging as a novel non-invasive technology for BBB opening to enhance delivery of therapeutics into the brain⁶⁷⁻⁷⁰. This approach, especially when performed under MRI-guidance, has excellent spatial control; however, the strategy needs to overcome the potential adverse of sterile inflammatory before being widely implemented in clinical trials⁷¹. Furthermore, FUS-induced BBBO in the brain parenchyma is usually combined with systemic administration of therapeutics, making it difficult to reach sufficient drug concentration at the targeted site and often resulting in toxic side effects. In contrast, IA approach combining selective BBBO immediately followed by localized delivery of a specific drug during the same procedure as a one-stop-shop affords adequate therapeutic concentration at the desired destination while minimizing systemic exposure.

Microscopic analysis in this study (both intravital and post mortem) provided information about the timing of BBB breach as well as parenchymal penetration of injected antibodies, further explaining our previous PET findings⁵¹ and other literature reports⁷²⁻⁷⁴. After IA delivery antibodies with an intact BBB were found to localize within blood vessels, while parenchymal presence was negligible. This is consistent with published literature showing extravasation of antibodies without BBBO is marginal^{51, 75-77}. Notably, BBBO paired with intravenous delivery of antibodies also results in poor brain accumulation⁵¹.

IA mannitol with coordinated closure of the contralateral CCA facilitated cortical BBBO; however, for effective BBB disruption longer exposure to mannitol (around 3 minutes) was required compared to subcortical structures. This phenomenon may result from the mixing and dilution of mannitol or differences in structure and function of cortical capillaries. Our dynamic intravital microscopy supported the mixing theory, where we observed the intermittent pulsatile flow pattern during IA infusion of the contrast agent. The structure and function of the microvessels may also contribute to differences in vulnerability to mannitol. Tissue-engineered models of the human BBB, which recapitulate shear stress, geometry, and physiological permeability have recently emerged as a platform to study BBBO⁷⁸. Within 3D BBB microvessels, mannitol-induced BBBO was observed to be heterogenous, occurring due to disruption of discrete cell-cell junctions between adjacent iPSC-derived brain microvascular endothelial cells⁷⁹. The multi-scale imaging studies are essential for developing precise, reproducible, and effective strategies for drug targeting. Even in the case of

direct intracerebral injection of small molecules, based on convection-enhanced delivery (CED), drug retention in the brain is uncertain. A recent PET study surprisingly reported that CED of low molecular weight molecules resulted in their rapid clearance⁸⁰. The mechanism of that rapid clearance is not well understood but the BBB functionality includes active efflux transporting molecules out of the CNS⁸¹. Meanwhile, this finding might also explain the limited efficacy of therapies when BBB permeable small molecules were used to treat CNS disorders, as they seem to be easily transported into peripheral circulation, resulting in inadequate therapeutic concentrations at the target. Hence, the developed platform for intravital imaging in the cortex will be of great value to accurately understand the drug behavior in the brain parenchyma with or without BBBO, profoundly contributing to the development of drug delivery strategies.

Thus, the last study in the project established reproducible cortical BBBO in mice, which enables multi-photon microscopy studies on BBBO and drug targeting. This approach enabled the real-time monitoring of the extravasation of IA injected antibodies. Such a platform will be critical for designing and guiding treatment strategies for a variety of neurological disorders.

6. Summary

The proposed project was a collaboration between the Johns Hopkins University and the University of Hamburg. We first developed a predictable, reproducible and safe mannitol-based BBBO technique in mice under real-time MRI guidance. This experimental platform was then exploited for targeted IA delivery of antibodies, nanobodies and PAMAM dendrimers to the brain. PET imaging revealed a significant advantage in brain accumulation for antibodies and nanobodies after IA delivery in contrast to no uptake when these agents were delivered using IV route. The effect was further potentiated by prior BBBO for IA route but again no accumulation has been observed after IV administration. Retention of both agents in the brain 24 h post IA infusion was very good. Pharmacokinetics of dendrimers was on the other hand less favorable. Even after IA injection dendrimers not only poorly accumulated in the brain during infusion but also completely cleared within 1 h of administration regardless of the BBB status. Dynamic imaging on a microscopy level during IA infusion visualized the moment of antibody leakage upon BBBO and the antibody indeed penetrated the brain parenchyma rather than being captured at the level of capillary vessels.

Das Projekt war eine Zusammenarbeit zwischen der Johns Hopkins University und der Universität Hamburg. Zunächst entwickelten wir eine vorhersehbare, reproduzierbare und sichere Technik zur Eröffnung der Blut-Hirn-Schranke mittels Mannitol in Mäusen unter Echtzeit-MRT Steuerung. Diese experimentelle Plattform wurde dann für die gezielte intraarterielle Gabe von Antikörpern, Nanobodies und PAMAM-Dendrimern in das Gehirn genutzt. In der PET Bildgebung zeigte sich nach intraarterieller Injektion eine signifikante Akkumulation von Antikörper und Nanobodies im Gehirn, während es nach einer intravenösen Gabe zu keiner Aufnahme im Gehirn kam. Ein vorheriges Öffnen der Blut-Hirn-Schranke mittels Mannitol verstärkte zusätzlich die Aufnahme nach intraarterieller Gabe. Nach intravenöser Verabreichung war jedoch weiterhin keine Akkumulation zu beobachten. Die Retention von Antikörpern und Nanobodies im Gehirn war 24 Stunden nach der intraarteriellen Infusion sehr gut. Die Pharmakokinetik der Dendrimere war dagegen weniger günstig. Die Dimere reichert sich nach der intraarteriellen Injektion schlecht im Gehirn an und waren unabhängig vom Status der Blut-Hirn-Schranke eine Stunde nach der Verabreichung im Gehirn nicht mehr nachweisbar. Die dynamische Bildgebung auf mikroskopischer Ebene während der intraarteriellen Infusion visualisierte den Moment des Austritts von Antikörpern nach Öffnung der Blut-Hirn-Schranke. Der Antikörper blieb nicht in den Kapillargefäßen, sondern drang in das Gehirnparenchym ein.

7. Reference

1. Moura, R. P.; Almeida, A.; Sarmiento, B., The role of non-endothelial cells on the penetration of nanoparticles through the blood brain barrier. *Prog Neurobiol* **2017**, *159*, 39-49.
2. Nduom, E. K.; Yang, C.; Merrill, M. J.; Zhuang, Z.; Lonser, R. R., Characterization of the blood-brain barrier of metastatic and primary malignant neoplasms. *J Neurosurg* **2013**, *119* (2), 427-33.
3. Budde, M. D.; Janes, L.; Gold, E.; Turtzo, L. C.; Frank, J. A., The contribution of gliosis to diffusion tensor anisotropy and tractography following traumatic brain injury: validation in the rat using Fourier analysis of stained tissue sections. *Brain* **2011**, *134* (Pt 8), 2248-60.
4. Pardridge, W. M., The blood-brain barrier: bottleneck in brain drug development. *NeuroRx* **2005**, *2* (1), 3-14.
5. Goldstein, G. W.; Betz, A. L., The Blood-Brain-Barrier. *Sci Am* **1986**, *255* (3), 74-&.
6. Cloughesy, T. F.; Gobin, Y. P.; Black, K. L.; Vinuela, F.; Taft, F.; Kadkhoda, B.; Kabbinavar, F., Intra-arterial carboplatin chemotherapy for brain tumors: a dose escalation study based on cerebral blood flow. *J Neurooncol* **1997**, *35* (2), 121-31.
7. Chakraborty, S.; Filippi, C. G.; Wong, T.; Ray, A.; Fralin, S.; Tsiouris, A. J.; Praminick, B.; Demopoulos, A.; McCrea, H. J.; Bodhinayake, I.; Ortiz, R.; Langer, D. J.; Boockvar, J. A., Superselective intraarterial cerebral infusion of cetuximab after osmotic blood/brain barrier disruption for recurrent malignant glioma: phase I study. *J Neurooncol* **2016**, *128* (3), 405-15.
8. Gonzales-Portillo, G. S.; Sanberg, P. R.; Franzblau, M.; Gonzales-Portillo, C.; Diamandis, T.; Staples, M.; Sanberg, C. D.; Borlongan, C. V., Mannitol-enhanced delivery of stem cells and their growth factors across the blood-brain barrier. *Cell Transplant* **2014**, *23* (4-5), 531-9.
9. Brightman, M. W.; Hori, M.; Rapoport, S. I.; Reese, T. S.; Westergaard, E., Osmotic opening of tight junctions in cerebral endothelium. *J Comp Neurol* **1973**, *152* (4), 317-25.
10. Foley, C. P.; Rubin, D. G.; Santillan, A.; Sondhi, D.; Dyke, J. P.; Crystal, R. G.; Gobin, Y. P.; Ballon, D. J., Intra-arterial delivery of AAV vectors to the mouse brain after mannitol mediated blood brain barrier disruption. *J Control Release* **2014**, *196*, 71-78.

11. Burkhardt, J. K.; Riina, H.; Shin, B. J.; Christos, P.; Kesavabhotla, K.; Hofstetter, C. P.; Tsiouris, A. J.; Boockvar, J. A., Intra-arterial delivery of bevacizumab after blood-brain barrier disruption for the treatment of recurrent glioblastoma: progression-free survival and overall survival. *World Neurosurg* **2012**, 77 (1), 130-4.
12. Joshi, S.; Ergin, A.; Wang, M.; Reif, R.; Zhang, J.; Bruce, J. N.; Bigio, I. J., Inconsistent blood brain barrier disruption by intraarterial mannitol in rabbits: implications for chemotherapy. *J Neurooncol* **2011**, 104 (1), 11-9.
13. Janowski, M.; Walczak, P.; Pearl, M. S., Predicting and optimizing the territory of blood–brain barrier opening by superselective intra-arterial cerebral infusion under dynamic susceptibility contrast MRI guidance. *Journal of Cerebral Blood Flow & Metabolism* **2016**, 36 (3), 569-575.
14. Kaya, M.; Gulturk, S.; Elmas, I.; Kalayci, R.; Arican, N.; Kocyildiz, Z. C.; Kucuk, M.; Yorulmaz, H.; Sivas, A., The effects of magnesium sulfate on blood-brain barrier disruption caused by intracarotid injection of hyperosmolar mannitol in rats. *Life Sci* **2004**, 76 (2), 201-12.
15. Yang, W. L.; Barth, R. F.; Leveille, R.; Adams, D. M.; Ciesielski, M.; Fenstermaker, R. A.; Capala, J., Evaluation of systemically administered radiolabeled epidermal growth factor as a brain tumor targeting agent. *Journal of Neuro-Oncology* **2001**, 55 (1), 19-28.
16. Tajiri, N.; Lee, J. Y.; Acosta, S.; Sanberg, P. R.; Borlongan, C. V., Breaking the Blood-Brain Barrier With Mannitol to Aid Stem Cell Therapeutics in the Chronic Stroke Brain. *Cell Transplant* **2016**, 25 (8), 1453-60.
17. Seyfried, D. M.; Han, Y.; Yang, D.; Ding, J.; Savant-Bhonsale, S.; Shukairy, M. S.; Chopp, M., Mannitol enhances delivery of marrow stromal cells to the brain after experimental intracerebral hemorrhage. *Brain Res* **2008**, 1224, 12-9.
18. Fu, H.; Muenzer, J.; Samulski, R. J.; Breese, G.; Sifford, J.; Zeng, X.; McCarty, D. M., Self-complementary adeno-associated virus serotype 2 vector: global distribution and broad dispersion of AAV-mediated transgene expression in mouse brain. *Mol Ther* **2003**, 8 (6), 911-7.
19. Yang, W.; Barth, R. F.; Rotaru, J. H.; Moeschberger, M. L.; Joel, D. D.; Nawrocky, M. M.; Goodman, J. H., Enhanced survival of glioma bearing rats following boron neutron capture therapy with blood-brain barrier disruption and intracarotid injection of boronophenylalanine. *J Neurooncol* **1997**, 33 (1-2), 59-70.

20. Yang, W.; Barth, R. F.; Leveille, R.; Adams, D. M.; Ciesielski, M.; Fenstermaker, R. A.; Capala, J., Evaluation of systemically administered radiolabeled epidermal growth factor as a brain tumor targeting agent. *J Neurooncol* **2001**, *55* (1), 19-28.
21. Cerri, S.; Greco, R.; Levandis, G.; Ghezzi, C.; Mangione, A. S.; Fuzzati-Armentero, M. T.; Bonizzi, A.; Avanzini, M. A.; Maccario, R.; Blandini, F., Intracarotid Infusion of Mesenchymal Stem Cells in an Animal Model of Parkinson's Disease, Focusing on Cell Distribution and Neuroprotective and Behavioral Effects. *Stem Cells Transl Med* **2015**, *4* (9), 1073-85.
22. Neuwelt, E. A.; Barnett, P. A.; Hellstrom, I.; Hellstrom, K. E.; Beaumier, P.; McCormick, C. I.; Weigel, R. M., Delivery of melanoma-associated immunoglobulin monoclonal antibody and Fab fragments to normal brain utilizing osmotic blood-brain barrier disruption. *Cancer Res* **1988**, *48* (17), 4725-9.
23. Kozler, P.; Riljak, V.; Jandova, K.; Pokorny, J., CT imaging and spontaneous behavior analysis after osmotic blood-brain barrier opening in Wistar rat. *Physiol Res* **2014**, *63 Suppl 4*, S529-34.
24. Chi, O. Z.; Liu, X.; Weiss, H. R., Effects of mild hypothermia on blood-brain barrier disruption during isoflurane or pentobarbital anesthesia. *Anesthesiology* **2001**, *95* (4), 933-8.
25. Godinho, B.; Henninger, N.; Bouley, J.; Alterman, J. F.; Haraszti, R. A.; Gilbert, J. W.; Sapp, E.; Coles, A. H.; Biscans, A.; Nikan, M.; Echeverria, D.; DiFiglia, M.; Aronin, N.; Khvorova, A., Transvascular Delivery of Hydrophobically Modified siRNAs: Gene Silencing in the Rat Brain upon Disruption of the Blood-Brain Barrier. *Mol Ther* **2018**, *26* (11), 2580-2591.
26. Martin, J. A.; Maris, A. S.; Ehteshami, M.; Singer, R. J., Rat model of blood-brain barrier disruption to allow targeted neurovascular therapeutics. *J Vis Exp* **2012**, (69), e50019.
27. Bhattacharjee, A. K.; Nagashima, T.; Kondoh, T.; Tamaki, N., Quantification of early blood-brain barrier disruption by in situ brain perfusion technique. *Brain Res Brain Res Protoc* **2001**, *8* (2), 126-31.
28. Ju, F.; Ran, Y.; Zhu, L.; Cheng, X.; Gao, H.; Xi, X.; Yang, Z.; Zhang, S., Increased BBB Permeability Enhances Activation of Microglia and Exacerbates Loss of Dendritic Spines After Transient Global Cerebral Ischemia. *Front Cell Neurosci* **2018**, *12*, 236.

29. Sammali, E.; Alia, C.; Vegliante, G.; Colombo, V.; Giordano, N.; Pischiutta, F.; Boncoraglio, G. B.; Barilani, M.; Lazzari, L.; Caleo, M.; De Simoni, M. G.; Gaipa, G.; Citerio, G.; Zanier, E. R., Intravenous infusion of human bone marrow mesenchymal stromal cells promotes functional recovery and neuroplasticity after ischemic stroke in mice. *Scientific reports* **2017**, *7* (1), 6962.
30. Lei, J.; Feng, F.; Duan, Y.; Xu, F.; Liu, Z.; Lian, L.; Liang, Q.; Zhang, N.; Wang, F., Intranasal nerve growth factor attenuating the seizure onset via p75R/Caspase pathway in the experimental epilepsy. *Brain research bulletin* **2017**, *134*, 79-84.
31. Uchida, H.; Niizuma, K.; Kushida, Y.; Wakao, S.; Tominaga, T.; Borlongan, C. V.; Dezawa, M., Human Muse Cells Reconstruct Neuronal Circuitry in Subacute Lacunar Stroke Model. *Stroke* **2017**, *48* (2), 428-435.
32. Janowski, M.; Wagner, D. C.; Boltze, J., Stem Cell-Based Tissue Replacement After Stroke: Factual Necessity or Notorious Fiction? *Stroke* **2015**, *46* (8), 2354-63.
33. Toma, C.; Wagner, W. R.; Bowry, S.; Schwartz, A.; Villanueva, F., Fate of culture-expanded mesenchymal stem cells in the microvasculature: in vivo observations of cell kinetics. *Circulation research* **2009**, *104* (3), 398-402.
34. Lappalainen, R. S.; Narkilahti, S.; Huhtala, T.; Liimatainen, T.; Suuronen, T.; Narvanen, A.; Suuronen, R.; Hovatta, O.; Jolkonen, J., The SPECT imaging shows the accumulation of neural progenitor cells into internal organs after systemic administration in middle cerebral artery occlusion rats. *Neuroscience letters* **2008**, *440* (3), 246-50.
35. Savitz, S. I.; Baron, J. C.; Fisher, M.; Consortium, S. X., Stroke Treatment Academic Industry Roundtable X: Brain Cytoprotection Therapies in the Reperfusion Era. *Stroke* **2019**, *50* (4), 1026-1031.
36. Owens, G., Arterial perfusion of the isolated canine brain. *Am J Physiol* **1959**, *197*, 475-7.
37. Hatiboglu, I.; Owens, G., Results of intermittent, prolonged infusion of nitrogen mustard into the carotid artery in twelve patients with cerebral gliomas. *Surg Forum* **1961**, *12*, 396-8.
38. Walczak, P.; Zhang, J.; Gilad, A. A.; Kedziorek, D. A.; Ruiz-Cabello, J.; Young, R. G.; Pittenger, M. F.; van Zijl, P. C. M.; Huang, J.; Bulte, J. W. M., Dual-Modality Monitoring of Targeted Intraarterial Delivery of Mesenchymal Stem Cells After Transient Ischemia. *Stroke* **2008**, *39* (5), 1569-1574.

39. Walczak, P.; Wojtkiewicz, J.; Nowakowski, A.; Habich, A.; Holak, P.; Xu, J.; Adamiak, Z.; Chehade, M.; Pearl, M. S.; Gailloud, P.; Lukomska, B.; Maksymowicz, W.; Bulte, J. W.; Janowski, M., Real-time MRI for precise and predictable intra-arterial stem cell delivery to the central nervous system. *J Cereb Blood Flow Metab* **2016**.
40. Guzman, R.; Janowski, M.; Walczak, P., Intra-Arterial Delivery of Cell Therapies for Stroke. *Stroke* **2018**, *49* (5), 1075-1082.
41. Ingram, J. R.; Schmidt, F. I.; Ploegh, H. L., Exploiting Nanobodies' Singular Traits. *Annu Rev Immunol* **2018**, *36*, 695-715.
42. Bannas, P.; Lenz, A.; Kunick, V.; Well, L.; Fumey, W.; Rissiek, B.; Haag, F.; Schmid, J.; Schutze, K.; Eichhoff, A.; Trepel, M.; Adam, G.; Ittrich, H.; Koch-Nolte, F., Molecular imaging of tumors with nanobodies and antibodies: Timing and dosage are crucial factors for improved in vivo detection. *Contrast Media Mol Imaging* **2015**, *10* (5), 367-78.
43. Kannan, R. M.; Nance, E.; Kannan, S.; Tomalia, D. A., Emerging concepts in dendrimer-based nanomedicine: from design principles to clinical applications. *J Intern Med* **2014**, *276* (6), 579-617.
44. Qiu, J.; Kong, L.; Cao, X.; Li, A.; Wei, P.; Wang, L.; Mignani, S.; Caminade, A. M.; Majoral, J. P.; Shi, X., Enhanced Delivery of Therapeutic siRNA into Glioblastoma Cells Using Dendrimer-Entrapped Gold Nanoparticles Conjugated with beta-Cyclodextrin. *Nanomaterials (Basel)* **2018**, *8* (3).
45. Svoboda, K.; Yasuda, R., Principles of two-photon excitation microscopy and its applications to neuroscience. *Neuron* **2006**, *50* (6), 823-39.
46. Liang, Y.; Li, K.; Riecken, K.; Maslyukov, A.; Gomez-Nicola, D.; Kovalchuk, Y.; Fehse, B.; Garaschuk, O., Long-term in vivo single-cell tracking reveals the switch of migration patterns in adult-born juxtglomerular cells of the mouse olfactory bulb. *Cell Res* **2016**, *26* (7), 805-21.
47. Vosjan, M. J.; Perk, L. R.; Visser, G. W.; Budde, M.; Jurek, P.; Kiefer, G. E.; van Dongen, G. A., Conjugation and radiolabeling of monoclonal antibodies with zirconium-89 for PET imaging using the bifunctional chelate p-isothiocyanatobenzyl-desferrioxamine. *Nat Protoc* **2010**, *5* (4), 739-43.
48. Holtmaat, A.; Bonhoeffer, T.; Chow, D. K.; Chuckowree, J.; De Paola, V.; Hofer, S. B.; Hubener, M.; Keck, T.; Knott, G.; Lee, W. C.; Mostany, R.; Mrsic-Flogel, T. D.; Nedivi, E.; Portera-Cailliau, C.; Svoboda, K.; Trachtenberg, J. T.; Wilbrecht, L.,

- Long-term, high-resolution imaging in the mouse neocortex through a chronic cranial window. *Nat Protoc* **2009**, 4 (8), 1128-44.
49. Janowski, M.; Lyczek, A.; Engels, C.; Xu, J.; Lukomska, B.; Bulte, J. W.; Walczak, P., Cell size and velocity of injection are major determinants of the safety of intracarotid stem cell transplantation. *J Cereb Blood Flow Metab* **2013**, 33 (6), 921-7.
 50. Gorelik, M.; Orukari, I.; Wang, J.; Galpoththawela, S.; Kim, H.; Levy, M.; Gilad, A. A.; Bar-Shir, A.; Kerr, D. A.; Levchenko, A.; Bulte, J. W.; Walczak, P., Use of MR cell tracking to evaluate targeting of glial precursor cells to inflammatory tissue by exploiting the very late antigen-4 docking receptor. *Radiology* **2012**, 265 (1), 175-85.
 51. Lesniak, W. G.; Chu, C.; Jablonska, A.; Du, Y.; Pomper, M. G.; Walczak, P.; Janowski, M., PET imaging of intra-arterial (89)Zr bevacizumab in mice with and without osmotic opening of the blood-brain barrier: distinct advantage of intra-arterial delivery. *J Nucl Med* **2018**.
 52. Laznickova, A.; Biricova, V.; Laznicek, M.; Hermann, P., Mono(pyridine-N-oxide) DOTA analog and its G1/G4-PAMAM dendrimer conjugates labeled with ¹⁷⁷Lu: radiolabeling and biodistribution studies. *Applied radiation and isotopes : including data, instrumentation and methods for use in agriculture, industry and medicine* **2014**, 84, 70-7.
 53. Sadekar, S.; Ray, A.; Janat-Amsbury, M.; Peterson, C. M.; Ghandehari, H., Comparative biodistribution of PAMAM dendrimers and HPMA copolymers in ovarian-tumor-bearing mice. *Biomacromolecules* **2011**, 12 (1), 88-96.
 54. Zhang, Y.; Sun, Y.; Xu, X.; Zhang, X.; Zhu, H.; Huang, L.; Qi, Y.; Shen, Y. M., Synthesis, biodistribution, and microsingle photon emission computed tomography (SPECT) imaging study of technetium-99m labeled PEGylated dendrimer poly(amidoamine) (PAMAM)-folic acid conjugates. *Journal of medicinal chemistry* **2010**, 53 (8), 3262-72.
 55. Lesniak, W. G.; Mishra, M. K.; Jyoti, A.; Balakrishnan, B.; Zhang, F.; Nance, E.; Romero, R.; Kannan, S.; Kannan, R. M., Biodistribution of fluorescently labeled PAMAM dendrimers in neonatal rabbits: effect of neuroinflammation. *Molecular pharmaceutics* **2013**, 10 (12), 4560-71.
 56. Kannan, S.; Dai, H.; Navath, R. S.; Balakrishnan, B.; Jyoti, A.; Janisse, J.; Romero, R.; Kannan, R. M., Dendrimer-based postnatal therapy for neuroinflammation and

- cerebral palsy in a rabbit model. *Science translational medicine* **2012**, 4 (130), 130ra46.
57. Boswell, C. A.; Sun, X.; Niu, W.; Weisman, G. R.; Wong, E. H.; Rheingold, A. L.; Anderson, C. J., Comparative in vivo stability of copper-64-labeled cross-bridged and conventional tetraazamacrocyclic complexes. *Journal of medicinal chemistry* **2004**, 47 (6), 1465-74.
 58. Gomes, J. R.; Cabrito, I.; Soares, H. R.; Costelha, S.; Teixeira, A.; Wittelsberger, A.; Stortelers, C.; Vanlandschoot, P.; Saraiva, M. J., Delivery of an anti-transthyretin Nanobody to the brain through intranasal administration reveals transthyretin expression and secretion by motor neurons. *Journal of neurochemistry* **2018**, 145 (5), 393-408.
 59. Samec, N.; Jovcevska, I.; Stojan, J.; Zottel, A.; Liovic, M.; Myers, M. P.; Muyldermans, S.; Sribar, J.; Krizaj, I.; Komel, R., Glioblastoma-specific anti-TUFGM nanobody for in-vitro immunoimaging and cancer stem cell targeting. *Oncotarget* **2018**, 9 (25), 17282-17299.
 60. McMurphy, T.; Xiao, R.; Magee, D.; Slater, A.; Zabeau, L.; Tavernier, J.; Cao, L., The anti-tumor activity of a neutralizing nanobody targeting leptin receptor in a mouse model of melanoma. *PloS one* **2014**, 9 (2), e89895.
 61. Weidman, E. K.; Foley, C. P.; Kallas, O.; Dyke, J. P.; Gupta, A.; Giambrone, A. E.; Ivanidze, J.; Baradaran, H.; Ballon, D. J.; Sanelli, P. C., Evaluating Permeability Surface-Area Product as a Measure of Blood-Brain Barrier Permeability in a Murine Model. *AJNR Am J Neuroradiol* **2016**, 37 (7), 1267-74.
 62. Chu, C.; Liu, G.; Janowski, M.; Bulte, J. W. M.; Li, S.; Pearl, M.; Walczak, P., Real-Time MRI Guidance for Reproducible Hyperosmolar Opening of the Blood-Brain Barrier in Mice. *Front Neurol* **2018**, 9, 921.
 63. Cui, L. L.; Kerkela, E.; Bakreen, A.; Nitzsche, F.; Andrzejewska, A.; Nowakowski, A.; Janowski, M.; Walczak, P.; Boltze, J.; Lukomska, B.; Jolkonen, J., The cerebral embolism evoked by intra-arterial delivery of allogeneic bone marrow mesenchymal stem cells in rats is related to cell dose and infusion velocity. *Stem Cell Res Ther* **2015**, 6, 11.
 64. Gillilan, L. A., Potential collateral circulation to the human cerebral cortex. *Neurology* **1974**, 24 (10), 941-8.

65. Cuccione, E.; Padovano, G.; Versace, A.; Ferrarese, C.; Beretta, S., Cerebral collateral circulation in experimental ischemic stroke. *Exp Transl Stroke Med* **2016**, *8*, 2.
66. Nhan, T.; Burgess, A.; Cho, E. E.; Stefanovic, B.; Lilge, L.; Hynynen, K., Drug delivery to the brain by focused ultrasound induced blood-brain barrier disruption: quantitative evaluation of enhanced permeability of cerebral vasculature using two-photon microscopy. *J Control Release* **2013**, *172* (1), 274-280.
67. Burgess, A.; Dubey, S.; Yeung, S.; Hough, O.; Eterman, N.; Aubert, I.; Hynynen, K., Alzheimer disease in a mouse model: MR imaging-guided focused ultrasound targeted to the hippocampus opens the blood-brain barrier and improves pathologic abnormalities and behavior. *Radiology* **2014**, *273* (3), 736-45.
68. Chen, K. T.; Wei, K. C.; Liu, H. L., Theranostic Strategy of Focused Ultrasound Induced Blood-Brain Barrier Opening for CNS Disease Treatment. *Front Pharmacol* **2019**, *10*, 86.
69. Etame, A. B.; Diaz, R. J.; Smith, C. A.; Mainprize, T. G.; Hynynen, K.; Rutka, J. T., Focused ultrasound disruption of the blood-brain barrier: a new frontier for therapeutic delivery in molecular neurooncology. *Neurosurg Focus* **2012**, *32* (1), E3.
70. Wang, S.; Shin, I. S.; Hancock, H.; Jang, B. S.; Kim, H. S.; Lee, S. M.; Zderic, V.; Frenkel, V.; Pastan, I.; Paik, C. H.; Dreher, M. R., Pulsed high intensity focused ultrasound increases penetration and therapeutic efficacy of monoclonal antibodies in murine xenograft tumors. *J Control Release* **2012**, *162* (1), 218-24.
71. Kovacs, Z. I.; Kim, S.; Jikaria, N.; Qureshi, F.; Milo, B.; Lewis, B. K.; Bresler, M.; Burks, S. R.; Frank, J. A., Disrupting the blood-brain barrier by focused ultrasound induces sterile inflammation. *Proc Natl Acad Sci U S A* **2017**, *114* (1), E75-E84.
72. Neuwelt, E. A.; Minna, J.; Frenkel, E.; Barnett, P. A.; McCormick, C. I., Osmotic blood-brain barrier opening to IgM monoclonal antibody in the rat. *Am J Physiol* **1986**, *250* (5 Pt 2), R875-83.
73. Rapoport, S. I., Advances in osmotic opening of the blood-brain barrier to enhance CNS chemotherapy. *Expert Opin Investig Drugs* **2001**, *10* (10), 1809-18.
74. Wang, B.; Siahaan, T.; Soltero, R., Drug Delivery: Principles and Applications. *Wiley Ser Drug Disc* **2005**, 1-448.
75. Razpotnik, R.; Novak, N.; Curin Serbec, V.; Rajcevic, U., Targeting Malignant Brain Tumors with Antibodies. *Front Immunol* **2017**, *8*, 1181.

76. Frank, R. T.; Aboody, K. S.; Najbauer, J., Strategies for enhancing antibody delivery to the brain. *Biochim Biophys Acta* **2011**, 1816 (2), 191-8.
77. Liu, H. L.; Hsu, P. H.; Lin, C. Y.; Huang, C. W.; Chai, W. Y.; Chu, P. C.; Huang, C. Y.; Chen, P. Y.; Yang, L. Y.; Kuo, J. S.; Wei, K. C., Focused Ultrasound Enhances Central Nervous System Delivery of Bevacizumab for Malignant Glioma Treatment. *Radiology* **2016**, 281 (1), 99-108.
78. DeStefano, J. G.; Jamieson, J. J.; Linville, R. M.; Searson, P. C., Benchmarking in vitro tissue-engineered blood-brain barrier models. *Fluids Barriers CNS* **2018**, 15 (1), 32.
79. Linville, R. M.; DeStefano, J. G.; Sklar, M. B.; Xu, Z.; Farrell, A. M.; Bogorad, M. I.; Chu, C.; Walczak, P.; Cheng, L.; Mahairaki, V.; Whartenby, K. A.; Calabresi, P. A.; Searson, P. C., Human iPSC-derived blood-brain barrier microvessels: validation of barrier function and endothelial cell behavior. *Biomaterials* **2019**, 190-191, 24-37.
80. Tosi, U.; Kommidi, H.; Bellat, V.; Marnell, C. S.; Guo, H.; Adeuyan, O.; Schweitzer, M. E.; Chen, N.; Su, T.; Zhang, G.; Maachani, U. B.; Pisapia, D. J.; Law, B.; Souweidane, M. M.; Ting, R., Real-Time, in Vivo Correlation of Molecular Structure with Drug Distribution in the Brain Striatum Following Convection Enhanced Delivery. *ACS Chem Neurosci* **2019**, 10 (5), 2287-2298.
81. Mayhan, W. G.; Heistad, D. D., Permeability of blood-brain barrier to various sized molecules. *Am J Physiol* **1985**, 248 (5 Pt 2), H712-8.

8. Explanation of own contribution

I am listed as the sole first author in the first publication entitled “Real-time MRI guidance for reproducible hyperosmolar opening of the blood-brain barrier in mice” and the third publication entitled “Optimization of osmotic blood-brain barrier opening to enable intravital microscopy studies on drug delivery in mouse cortex”. I was spearheading the majority of work in both studies and was involved in the conception and design. Specifically, my contribution was with the acquisition of data including animal surgery, MRI, microscopic imaging and histopathology. I personally performed majority of data analysis and interpretation. I was in charge of the statistical analysis, drafting the manuscripts as well as revising them after receiving comments from other coauthors. In the second publication entitled "PET imaging of distinct brain uptake of a nanobody and similarly-sized PAMAM dendrimers after intra-arterial administration", I am listed as a co-first author. In this study, I was responsible for the animal experiments including arterial catheterization, contributed to PET imaging, postmortem analysis as well as the manuscript editing.

9. Acknowledgements

First and foremost, I would like to express the heartfelt gratitude to my supervisors Prof. Dr. Tim Magnus and Prof. Dr. Piotr Walczak. Thank you, Dr. Magnus, for giving me the opportunity to do my doctoral thesis under your guidance. This precious opportunity is a critical step for my future career. Thank you, Dr. Walczak, for your constant encouragement and support. You taught me everything from how to address scientific questions efficiently to how to develop and implement my own ideas. Also, thank you for the encouragement to attend local and international conferences, where I kept in touch with the cutting-edge knowledge and got inspiration for my own research. All his help and guidance drive me closer to be an excellent researcher. I also want to thank my master's thesis supervisor, Prof. Shen Li, who recommended me to study and work with Dr. Walczak at the Johns Hopkins University. She always gave me valuable advice and help whenever needed.

I would like to sincerely acknowledge Prof. Miroslaw Janowski for his critical comments, valuable suggestion and prompt feedbacks. He is a very smart advisor who I could easily approach whenever I encountered research questions. Special thanks go to Ms. Larissa Jank for her kind help with coordinating my enrollment and providing instructions on how to efficiently build my thesis.

I also deeply express my gratitude to all the coauthors of the articles included in this thesis. Thank Dr. Wojciech G. Lesniak for helping with radiolabeling and PET imaging. Thank Dr. Babak Behnam Azad and Dr. Jan Gettemans for providing the nanobody and PAMAM dendrimers. Thank Ms. Ala Lisok for her assistance with *ex vivo* biodistribution experiments. Special thanks to Dr. Anna M. Jablonska for her assistance with the animal experiments and radioactivity measurements. She was always ready to help on scientific and personal matters during my stay in the USA.

My special thanks go out to my colleagues and friends who are not included in the articles but without you, I couldn't finish my thesis. Thank Ms. Lea Fortuno-Miranda for ordering all the materials needed to carry on with my project. Thank Ms. Irina Shats for her help with performing the histology. I also want to extend my thanks to Dr. Yue Yuan, Dr. Wei Zhu, Dr. Jia Zhang, Dr. Lin Chen, Dr. Jing Liu for their company and kind help. It was such a joy living with you.

Last but not least, greatest thanks to my wife Yue Gao for believing in me and listening to me. Also, greatly appreciate my family for their unconditional love and support over these years.

10. Curriculum vitae

Name Chengyan Chu

Date of Birth Aug 12, 1990

Contact Information

Email: dychuchengyan@hotmail.com

Foreign Languages: English (working knowledge)

Education

2009 - 2014 Bachelor of Clinical Medicine, Dalian Medical University

2014 - 2016 Master of Clinical Medicine, Neurology, Dalian Medical University

Honors And Awards

2013 Pacemaker Student of Dalian Medical University, Dalian Medical University

2014 Inspirational outstanding college students of Liaoning Province, Dalian Medical University

2016 Outstanding Graduate student of Dalian City, Dalian Medical University

Selected Publications

1. **Chu C**, Jablonska A, Lesniak W, Thomas A, Lan X, Linville R, Li S, Searson P, Liu G, Pearl M, Pomper M, Janowski M, Magnus T, Walczak P*. Optimization of osmotic blood-brain barrier opening to enable intravital microscopy studies on drug delivery in mouse cortex. J Control Release, 2020, 317: 312-321.
2. **Chu C**, Liu GS, Janowski M, Bulte JWM, Shen L, Pearl M, Walczak P*. Real-time MRI guidance for reproducible hyperosmolar opening of the blood-brain barrier in mice. Front Neurol, 2018, 9:921.
3. Lesniak WG[#], **Chu C**[#] (co-first), PET imaging of distinct brain uptake of a nanobody and similarly-sized PAMAM dendrimers after intra-arterial administration. European Journal of Nuclear Medicine and Molecular Imaging, 2019, 46:1940-1951. Int J Radiat Oncol Biol Phys, 2020, 108(3): 745-757.
4. **Chu C**, Davis C, Lan X, Hienz R, Jablonska A, Thomas A, Velarde E, Li S, Janowski M, Kai M*, Walczak P*. Neuroinflammation after stereotactic radiosurgery-induced brain tumor disintegration is linked to persistent cognitive decline in a mouse model of metastatic disease.
5. Lesniak W, **Chu C**, Jablonska A, Du Y, Pomper MG, Walczak P, Janowski M*. PET imaging of intra-arterial 89Zr bevacizumab in mice with and without osmotic opening of the blood-brain barrier: distinct advantage of intra-arterial delivery. Journal of Nuclear Medicine, 2018, 60 (5), 617-622.

11. Eidesstattliche Versicherung

Ich versichere ausdrücklich, dass ich die Arbeit selbständig und ohne fremde Hilfe verfasst, andere als die von mir angegebenen Quellen und Hilfsmittel nicht benutzt und die aus den benutzten Werken wörtlich oder inhaltlich entnommenen Stellen einzeln nach Ausgabe (Auflage und Jahr des Erscheinens), Band und Seite des benutzten Werkes kenntlich gemacht habe.

Ferner versichere ich, dass ich die Dissertation bisher nicht einem Fachvertreter an einer anderen Hochschule zur Überprüfung vorgelegt oder mich anderweitig um Zulassung zur Promotion beworben habe.

Ich erkläre mich einverstanden, dass meine Dissertation vom Dekanat der Medizinischen Fakultät mit einer gängigen Software zur Erkennung von Plagiaten überprüft werden kann.

Unterschrift: